Novel Semiconductor Materials for Mid-Infrared Optoelectronic Application

Thesis submitted in accordance with the requirements of the

University of Liverpool for the degree of Doctor in Philosophy in the

Faculty of Science and Engineering by

Zhongming Cao

March 2021

Department of Electrical Engineering and Electronics

Contents

Abstract

Thin film gallium antimony bismuth (GaSbBi) grown on GaSb substrate via molecular beam epitaxy (MBE) have been explored in this thesis by characterising the films electrical, physical and optical properties. From these wafers Schottky diodes, and metal-semiconductor-metal photodetectors (MSM-PDs) have been investigated. Another promising material for infrared photodetectors is InAs, in this work the use of high-k based dielectrics has been investigated to improve the passivation of InAs avalanche photodiodes (APDs).

Initially, the influence of postgrowth thermal annealing on GaSbBi Schottky barrier diodes has been investigated. The I-V characteristics indicated a better ideality factor and less leakage current at the reverse bias, as the annealing temperature increased up to 500 °C for a duration of 30 min. X-ray diffraction and scanning transmission electron microscope measurements were performed to verify that the bismuth composition was unaffected during the annealing process. Energy dispersive x-ray analysis indicated that Sb clustering occurs at high annealing temperatures, resulting in a concomitant degradation in the electrical performance. The optimum electrical characteristics of the diode were obtained with an annealing temperature of 500 °C for 30 min, resulting in an ideality factor of 1.3 being achieved.

The optimised GaSbBi and GaSbN samples were then fabricated into MSM-PDs and verify the viability of using GaSbBi and GaSbN as active layers in photodetector. The cut-off wavelength extended to 1950 nm (2.9% Bi), 1990 nm (3.8% Bi), 2080 nm (4.5% Bi) and 2190 nm (1.5% N) have been observed, demonstrating the viability of using Bi and N for mid-infrared sensing. The comparison of different geometry on the photo spectral response indicating Bi incorporation increase the lattice expansion, which reduce the carrier concentration of the devices.

Optimization of InAs based APDs are reported in this thesis. The use of high-k dielectric material as a passivation layer to improve the performance of InAs APDs are discussed. Three potential passivation layers, including ZnO, Al_2O_3 and MgO have been identified, all of which enables the suppression of surface leakage in smaller sized InAs APDs with a radius of 50 μm and at lower temperatures of 175 K compared to a reference SU8 device. The influence of repeated temperature cycling on these layers has also been investigated with ZnO observed clear degradation after ten cycle, MgO shows almost a 10% higher current at a constant voltage after ten temperature cycles and Al_2O_3 passivated device, exhibiting no change in performance after temperature cycles. Suggesting Al_2O_3 as an effective and stable material for InAs APDs.

List of publications

Conference presentations

1. **Influence of annealing on the electrical characteristics of GaSbBi Schottky diodes**

   <u>**Z. Cao**</u>, T. Veal, M. Ashwin, K. Dawson and I. Sandall

   UK Semiconductors 2018, Sheffield, United Kingdom, 4th-5th July 2018

2. **High-k dielectric passivation of InAs Avalanche Photodiode**

   <u>**Z. Cao**</u> and I. Sandall

   UK Semiconductors 2019, Sheffield, United Kingdom, 10th-11th July 2019

3. **GaAsSbN for multi-junction solar cell**

   Mumtaz, M. Milanova, I. Sandall, K. Cheetham, <u>**Z. Cao**</u>, M. Bilton, G. Piana, N. Fleck, L. Philips, O. Hutter, V. Donchev and K. Durose

   47th IEEE Photovoltaic Specialists Conference, Calgary, Canada, 15th June-21th Aug 2020

   DOI: 10.1109/PVSC45281.2020.9300524

4. **GaSbBi metal-semiconductor-metal photodetectors for mid-infrared sensing**

   <u>**Z. Cao**</u>, T. Veal, M. Ashwin and I. Sandall

   IEEE Photonics Conference, Vancouver, Canada, 28th Sept-1st Oct 2020

   DOI: 10.1109/IPC47351.2020.9252225

Journal papers

1. **Influence of annealing on the electrical characteristic of GaSbBi Schottky diodes**

Z. Cao, T. Veal, M. Ashwin, K. Dawson and I. Sandall, *Journal of Applied Physics*, vol. 126, no. 5, p. 053103, 2019

DOI: https://doi.org/10.1063/1.5108870

2. **Suppression of Surface Leakage Currents in InAs Avalanche Photodiodes via sputtering of high k – dielectric layers**

    Z. Cao, I. Mitrovic and I. Sandall, *IEEE Transactions on Electron Devices*, vol. 67, no. 10, p. 4269-4273, 2020

    DOI: 10.1109/TED.2020.3012122

3. **Single-junction solar cells based on p-i-n GaAsSbN heterostructures grown by LPE**

    M. Milanova, V. Donchev, K. Cheetham, **Z. Cao,** I. Sandall, G. Piana, O. Hutter, K. Durose, A. Mumtaz, *Solar Energy*, vol 208, p 659-664, 2020

    DOI: https://doi.org/10.1016/j.solener.2020.08.029

4. **GaSbBi metal-semiconductor-metal for mid-infrared sensing**

    Z. Cao, T. Veal, M. Ashwin and I. Sandall, **preparing**

Acknowledgements

Like the saying goes, if I have seen further, it is by standing on the shoulders of giants. There are many people whom I would like to thank for helping me get to this point.

Firstly, I would like to express my greatest gratitude to my primary supervisor Dr Ian Sandall. Ian welcomed me to his research group after I graduated with my master degree. At the time I was felt a lack of direction, and he provided me with an excellent opportunity to join this research project. I must thank him for his guidance from the very beginning, the encouragement he has given, the knowledge he has shared and also the friendship he has given me over the past four years. I also wish to thank him for his help with revision and the huge support for my upcoming career after the PhD studies.

Luckily, most of my work has been performed on a collaborative basis. Therefore, I would like to take this opportunity to thank Dr Mark Ashwin from the University of Warwick and Prof. Tim Veal in the Stephenson Institute, who has helped to grow the sample used in this project and given me suggestions on my paper. Dr Karl Dawson from the imaging centre at the University of Liverpool has helped to perform TEM measurement. I would also like to thank my secondary supervisor, Dr Ivona Mitrovic for her guidance and advice, especially for sharing the constructive comments of my research work on the high-k dielectric material.

The members of the BOSE group have helped me all along the way, my appreciation also extends to my colleagues and friends, Dr Naser Sedghi, Dr Andrew Shaw, Dr David Donaghy, Dr Siti Supardan, Chughtai, Serdar, Siriny, Adeem, Michael, Sorcha, Harry and Tom. My PhD work cannot finish without the help and encouragement of you all.

My Extra thanks are reserved for Prof. Huiping Zhang and my aunty Dr Ying Yan from the South China University of Technology. I couldn't image that I'm able to study aboard and even finish my PhD work. I would like to thank them for their support and inspiration since I was in high school, my life has changed because of them.

Finally, a very special thanks are reserved for my parents. I'm really grateful for the support and love that my parents have given me. I wouldn't have made it to study aboard without the encouragement from mum, and I couldn't have stayed in the UK for five years without my dad, who dedicated his life to business and support me with all he can. There are no words that I can express my love for my family, but I do wish I can be yours pride and joy.

Lift of figures

List of tables

Chapter 1

1   Introduction

The development of infrared technologies can trace back to 1800 when Willian Herschel built a crude monochromator that used a thermometer as a detector so that he could measure the distribution of energy in sunlight and found that the existence of thermal radiation in the invisible beyond the red, which leads to the discovery of infrared light [1]. After that, limited progress was made apart from establishing that infrared radiation obeyed the simplest law of optics [2-4]. The most advanced development of infrared technology happened after World War II, and that development is primarily driven by military applications. The discovery of the versatile narrow bandgap mercury cadmium telluride (HgCdTe) ternary alloy in 1959 has opened up a new area in IR detector technology and has provided an unprecedented degree of freedom in the design of infrared photoconductive and photovoltaic detector[5, 6].

The infrared detectors are used to detect the thermal radiation that all objects emit. In general, infrared detectors can be classified into two categories: thermal detectors and photon detectors. Where thermal detectors absorb the incident radiation to alter the temperature of the material, the resultant change in the physical properties is used to generate electrical output. The photon detector, on the other hand, absorbing the incident radiation within the material by interaction with electrons, while the generated electrical signal is the result of the changed electronic energy distribution in the semiconductor material [7, 8].
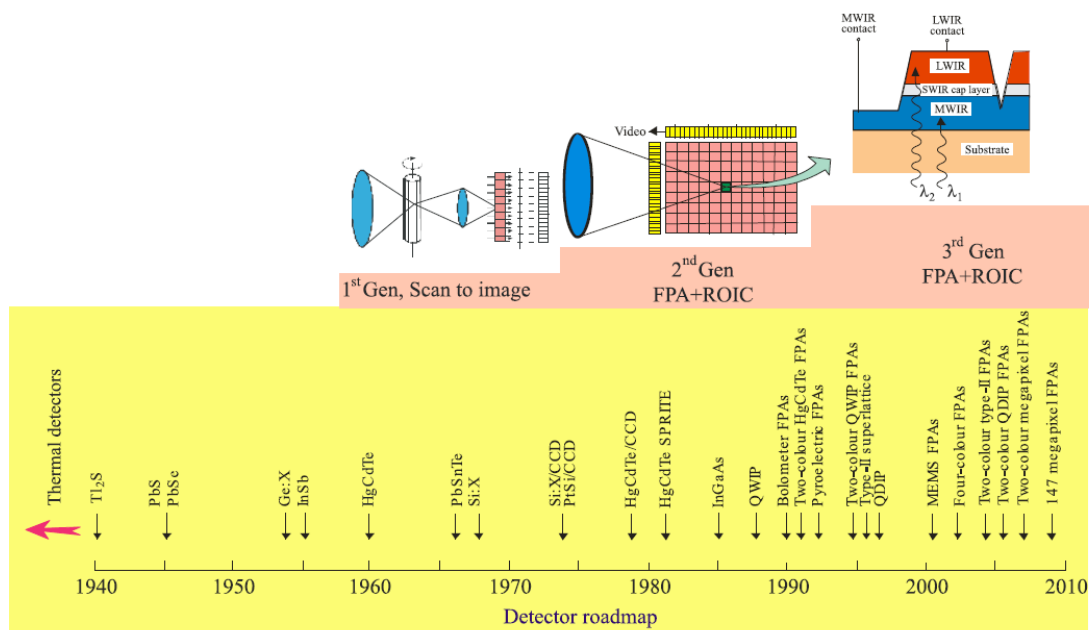
Figure 1. 1 History of the development of infrared detectors and systems [9].

Over the past two centuries, most of the progress developed on infrared technology is connected to semiconductor photon detectors. Many materials have been investigated in the infrared field. A progress report on the infrared detector technology, presented in 2011, has summarised some of the key breakings through the development of infrared detectors and systems [9]. The highlight of the main historical infrared detectors and system is shown in Figure 1. 1. Among those materials, HgCdTe is the most dominated semiconductor material for mid and long-wavelength infrared optoelectronics. The development of HgCdTe technology is primarily for the military defence. In addition, the main focus has been on focal plane array (FPA) demonstration [10-13], the knowledge based information is relative less reported [5]

With the growing development of infrared technology, the infrared optoelectronic application has expended its initial interest from military defence to civil applications. In particular, smart infrared photodetector has great potential used for the important area such as surveillance [14], space exploration [15], medical imaging [16], environmental monitoring [17], and many others. While conventional bulk and other novel nano-semiconductor materials, such as HgCdTe [5], InGaAs [18], nanowires [19], quantum dots [20] and quantum well [21] have been used to develop infrared photodetector. Due to its high responsivity speed, broad detection wavelength (1-30 μm) and large optical coefficients that enable high quantum efficiency [22], HgCdTe has always been an industrial favourite over the past decades. However, there are always numerous attempts to replace HgCdTe with alternative materials. The main motivations, behind the numerous attempts to find replace material, are the technological problems of this material.

III-V semiconductor compound, are those made from group three and five elements of the periodic table, and are important for a wide range of optical devices. Material such as GaSb and InAs have great potential to explore the short wavelength of the infrared region, due to the nature of their narrow bandgaps. While introducing a small amount of bismuth [23] or nitride [24] can significantly alter the band structure of the III-V semiconductor material, and thus extend the emission wavelength to cover a wider range of the infrared spectrum, providing a group of novel semiconductor materials for the research in the infrared region. This breakthrough allowed the high-performance infrared system of small size, lightweight and low cost and therefore suitable for civil applications.

1.1   Thesis outline

The structure of this thesis is outlined as follows. Chapter 2 provide an extensive literature review into a summary of semiconductor physics and dilute bismuth properties. The operating

principle of photodetectors is also discussed. Chapter 3 introduce the experimental and analysis techniques used throughout this thesis. The method used for the device fabrication, physical, electrical and optical characterisation of the thin film semiconductor is explained. Chapter 4 presents the influence of the post-growth thermal annealing process on GaSbBi Schottky diodes. The effects of the annealing temperature and time on the material quality and electrical characteristics of the diodes have been studied as well. Chapter 5 demonstrate the viability of using bismuth for mid-infrared sensing by the metal-semiconductor-metal photodetector. The effect of bismuth incorporation and geometry of the device on the spectral response has also been studied. Chapter 6 investigated the effectiveness of using high-k dielectric layers as potential passivation layers for InAs avalanche photodiodes. The electrical characteristics of a differently sized diode passivated with each high-k layer are investigated. Finally, the conclusions and suggestions for future works are presented in chapter 7.

1.2   Reference

[1]   W. Herschel, "XIV. Experiments on the refrangibility of the invisible rays of the sun," *Philosophical Transactions of the Royal Society of London,* no. 90, pp. 284-292, 1800.

[2]   E. S. Barr, "Historical survey of the early development of the infrared spectral region," *American Journal of physics,* vol. 28, no. 1, pp. 42-54, 1960.

[3]   R. A. Smith, F. E. Jones, and R. P. Chasmar, "The detection and measurement of infrared radiation," 1968.

[4]   P. W. Kruse, L. D. McGlauchlin, and R. B. McQuistan, "Elements of infrared technology: Generation, transmission and detection," *New York: Wiley,* 1962.

[5]   A. Rogalski, "HgCdTe infrared detector material: history, status and outlook," *Reports on Progress in Physics,* vol. 68, no. 10, p. 2267, 2005.

[6]   W. Lawson, S. Nielsen, E. Putley, and A. Young, "Preparation and properties of HgTe and mixed crystals of HgTe-CdTe," *Journal of Physics and Chemistry of Solids,* vol. 9, no. 3-4, pp. 325-329, 1959.

[7]   A. Rogalski, "Infrared detectors: an overview," *Infrared physics & technology,* vol. 43, no. 3-5, pp. 187-210, 2002.

[8]   A. Rogalski, "History of infrared detectors," *Opto-Electronics Review,* vol. 20, no. 3, pp. 279-308, 2012.

[9]   A. Rogalski, "Recent progress in infrared detector technologies," *Infrared Physics & Technology,* vol. 54, no. 3, pp. 136-154, 2011.

[10]   R. Bommena *et al.*, "High-performance SWIR HgCdTe FPA development on silicon substrates," in *Infrared Technology and Applications XL*, 2014, vol. 9070: International Society for Optics and Photonics, p. 907009.

[11]   H. Yuan *et al.*, "FPA development: from InGaAs, InSb, to HgCdTe," in *Infrared Technology and Applications XXXIV*, 2008, vol. 6940: International Society for Optics and Photonics, p. 69403C.

[12]   E. Smith *et al.*, "HgCdTe focal plane arrays for dual-color mid-and long-wavelength infrared detection," *Journal of electronic materials,* vol. 33, no. 6, pp. 509-516, 2004.

[13]   J. Beck *et al.*, "Gated IR imaging with 128× 128 HgCdTe electron avalanche photodiode FPA," *Journal of electronic materials,* vol. 37, no. 9, pp. 1334-1343, 2008.

[14]   B. Song, H. Choi, and H. S. Lee, "Surveillance tracking system using passive infrared motion sensors in wireless sensor network," in *2008 International Conference on Information Networking*, 2008: IEEE, pp. 1-5.

[15]   T. S. Lomheim, E. L. Milne, J. D. Kwok, and A. Tsuda, "Performance/sizing relationships for a short-wave/mid-wave infrared scanning point-source detection space sensor," in *1999 IEEE Aerospace Conference. Proceedings (Cat. No. 99TH8403)*, 1999, vol. 4: IEEE, pp. 113-138.

[16]   N. A. Diakides and J. D. Bronzino, *Medical infrared imaging*. CRC press, 2007.

[17]   M. S. de Cumis *et al.*, "Widely-tunable mid-infrared fiber-coupled quartz-enhanced photoacoustic sensor for environmental monitoring," *Optics express,* vol. 22, no. 23, pp. 28222-28231, 2014.

[18]   D. Bimberg, N. Kirstaedter, N. Ledentsov, Z. I. Alferov, P. Kop'Ev, and V. Ustinov, "InGaAs-GaAs quantum-dot lasers," *IEEE Journal of selected topics in quantum electronics,* vol. 3, no. 2, pp. 196-205, 1997.

[19]   E. A. Anyebe *et al.*, "Optimization of self-catalyzed InAs Nanowires on flexible graphite for photovoltaic infrared photodetectors," *Scientific reports,* vol. 7, no. 1, pp. 1-9, 2017.

[20]   I. Sandall, J. Ng, J. David, H. Liu, and C. Tan, "Evaluation of InAs quantum dots on Si as optical modulator," *Semiconductor science and technology,* vol. 28, no. 9, p. 094002, 2013.

[21]   O. Delorme *et al.*, "GaSbBi/GaSb quantum well laser diodes," *Applied Physics Letters,* vol. 110, no. 22, p. 222106, 2017.

[22]   M. Reine, "Fundamental properties of mercury cadmium telluride," *Encyclopedia of Modern Optics, Academic Press, London,* vol. 322, 2004.

[23]   H. Li and Z. M. Wang, *Bismuth-containing compounds*. Springer, 2013.

[24]   M. Henini, *Dilute nitride semiconductors*. Elsevier, 2004.

Chapter 2

2. Literature review and background

The general topic and background outline within this thesis are discussed in this chapter; a summary of semiconductor physics, bismuth properties, junctions, conduction mechanisms and the operating principle of photodetectors are discussed.

2.1 The semiconductor of physics (band structure, Bi incorporation)

2.1.1 Crystal structure

In general, semiconductor materials can be classified into one of three structural classes; crystal [1], polycrystalline [2] and amorphous semiconductors [3]. Figure 2. 1 shows the different structure of semiconductor material. In a crystal semiconductor material, each atom occupies a particular location forming a crystal lattice. A polycrystalline semiconductor consists of many different crystals. But those crystals that are oriented in different orientations do not line up at the boundaries. The boundaries between the different directions called grain boundary. At the grain boundary, the atoms do not match up well, and the grain boundary is the source of defects. These defects affect the electronic performance of a material. Amorphous semiconductors are a class of material that does not show long-range order. The atoms are more or less randomly distributed throughout the solid, which the atoms are not in a precise location specified by a crystal lattice and basis. Although the amorphous semiconductor does not show long-range order, they are likely to show short-range order behaviour, enabling the electronic properties of amorphous semiconductor to be similar to the electronic properties of crystalline semiconductor material.
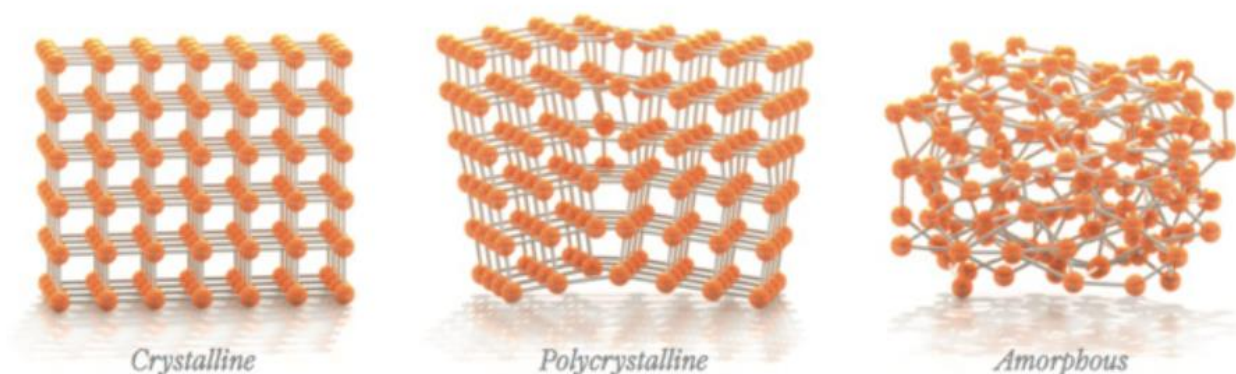
Figure 2. 1 Different degree of ordered structured: crystalline, polycrystalline and amorphous [4]

Crystalline semiconductors are the most expensive material because it is challenging to grow them with high quality (low number of defects). It requires putting every atom in its precise

location, which confirms the highest quality of crystalline semiconductor material with the fewest defects. Comparatively, polycrystalline semiconductors are less expensive to produce; however, these grain boundaries form between each crystal can impede current flow. This type of material is used when the highest quality is not needed, but the cost is essential. For example, the polycrystalline semiconductor material can be used in solar cells, where a large area of semiconductor material is utilised. Some fabrication processes include annealing, which can reduce the negative effect caused by boundary defects [5-7]. The amorphous semiconductor materials are the least expensive and have the most inferior electronic properties among semiconductor materials. The amorphous semiconductor is usually used when the cost is a critical consideration.

The crystal structure is a unique arrangement of atoms in a crystalline material, which plays an essential role in determining the physical properties, such as its band structure and optical transparency [8]. Before fabricating the material into electronic devices, it is important to study the crystal structure in the first place. The most widespread and powerful technique for studying the material properties is X-ray diffraction; other structure determination methods include using the wave character of neutrons or electrons, which are more appropriate for surface structure determination [9].

2.1.2   Band structure

Many materials with electrical conductor properties can be classified into three categories; metal, semiconductor and insulator. A practical method to visualize the difference between each material is studying the energy band structure of the material.

In a single atom, the electron occupies discrete energy levels. When forming a solid material, numerous atoms are brought together. While the atoms are bringing closer, the energy level of those atoms will split into energy bands. In terms of energy bands at zero-degree Kelvin, the electrons responsible for forming bonds between atoms are found in the last occupied band, where electrons have the highest energy level for the ground-state atoms. The lowest bands contain core electrons, which are tightly bound to the atoms, and the highest bands contain no electrons, in an infinite number of energy bands. The last ground- state band, which contains electrons, is called the valence band [10]. The energy bonds state that holds the semiconductor lattice together is filled with electrons forming the covalent bonds in the valence band. There is also an equal number of empty states that are available to hold electron is directly above the valence band called the conduction band. The energy difference between the bottom of the

conduction band and the top of the valence band is called the forbidden gap [10]. All of the valence band states are filled with electrons, and all of the conduction band states are empty, and there are no states in the forbidden gap. At room temperature, some of the electrons generate enough thermal energy to break the valence bonds between atoms and circulate in the crystal. Those electrons have gone from the valence band to the conduction band. The number of electrons in the conduction band and the holes in the valence band are equal, and this number is called intrinsic carrier concentration [11].
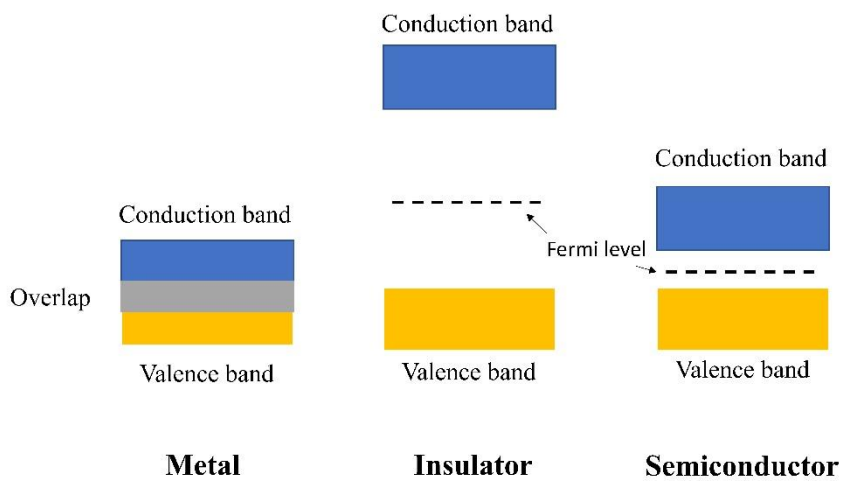
Figure 2. 2 Energy band diagrams in metal, insulator and semiconductor

The energy band diagram of metal, insulator and semiconductor have shown in Figure 2. 2. In metal, the conduction band overlaps the valence band, and because of overlap, the electron in the valence band can move through the material to become conductive. In the insulator, there also has a conduction band and valence band but a large forbidden gap in between, making the electron in the valence band unable to get into the conduction band, therefore unable to become conductive. Similarly, the semiconductor also has a valence band, conduction band and forbidden gap. However, the forbidden gap is much smaller. When the electron moves from the valence band to the conduction band, it does require a certain amount of energy, but the energy can be gained through thermal energy. Once the electron arrives at the conduction band, it becomes free to conductive, and it will conduct if the electric field is applied.

One of the important mechanisms in the semiconductor band structure is recombination and generation of carriers, as shown in Figure 2. 3 at the equilibrium, where the electrons and holes

are sitting at valence and conduction band, respectively. However, semiconductor devices are easily taken out of equilibrium by the changes in the environment. This could be affected by external effect, including thermal energy and doping density. Once sufficient energy is generated, the electron in the valence band can be excited and able to get into the conduction band. This process is the standard band to band generation. It is also the mechanism of electrons and holes pair are created. Different semiconductor material have different absorption coefficients. The absorption coefficient describes how far light of a particular wavelength can penetrate into a material before being fully absorbed. The material with higher absorption coefficient can readily absorb photons, which helps to efficiently excite electrons into the conduction band. When the energy of the photons is very close to the band gap, the absorption rate is relatively low since only the electrons at the valance band edge and interact into conduction band. However, when the photon energy increased, more electrons at lower energy level can interact with the photon to cause absorption. The band to band recombination process is the opposite of the generation process, in which the electrons in the conduction band can fall into the valence band, fill up the hold and replace the covalent bond. During this process, there are some energy has to be given up. The extra energy can go out in the form of light in direct gap semiconductor materials such as most III-V material. The other possibility is the extra energy can give up in the form of heat in the indirect gap semiconductor such as crystalline silicon.
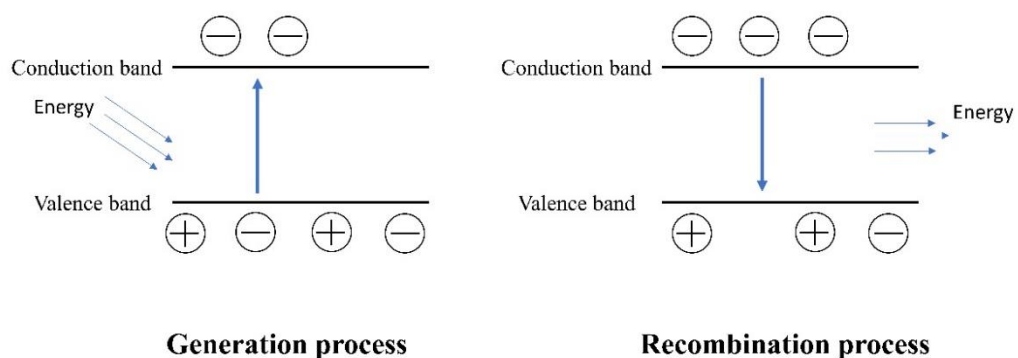
Figure 2. 3 Diagram of the standard band to band generation and recombination process

2.1.3   Direct and indirect band gap semiconductor

While considering the electron as a particle moving in a velocity in the band structure, the energy-momentum (E-k) relation is very useful to study the band structure of direct and indirect band gap semiconductor material, especially in the reactions with photons and phonons where energy and momentum have to be conserved. An example of energy band structures of direct and indirect band gap semiconductor is shown in Figure 2. 4. In the case of direct band gap structure, the conduction band minimum (CBM) energy and the valence band maximum (VBM) energy are at the same momentum value, the electron from the CBM can recombine with the hole in the VBM directly emitting a light photon of energy, where the energy is the difference between CBM and VBM. In the case of indirect band gap semiconductor on the other hand, the CBM and VBM appears at different values of momentum, which means the conservation of momentum is not satisfied. In this case, the momentum of electron will not be conserved. In order to conserved the momentum, another particle called phonon (quantized modes of lattice vibration) will be created or absorbed based on different situation such as heating or cooling the material. In the indirect band gap semiconductor, an electron from CBM can recombine with a hole in the VBM by creation or annihilation of phonons. However, the probability of both a photon and phonon occurring simultaneously is very low and as such the radiative lifetime becomes extremely long. Therefore, radiative recombination becomes extremely unlikely in indirect band gap semiconductors. The direct bandgap semiconductor material is mostly from compound semiconductors, and these type materials are usually used to fabricate into laser diodes. The indirect semiconductor material, such as Si are used to amplify the signal as in transistors and rectifier diodes.

(a)   (b)
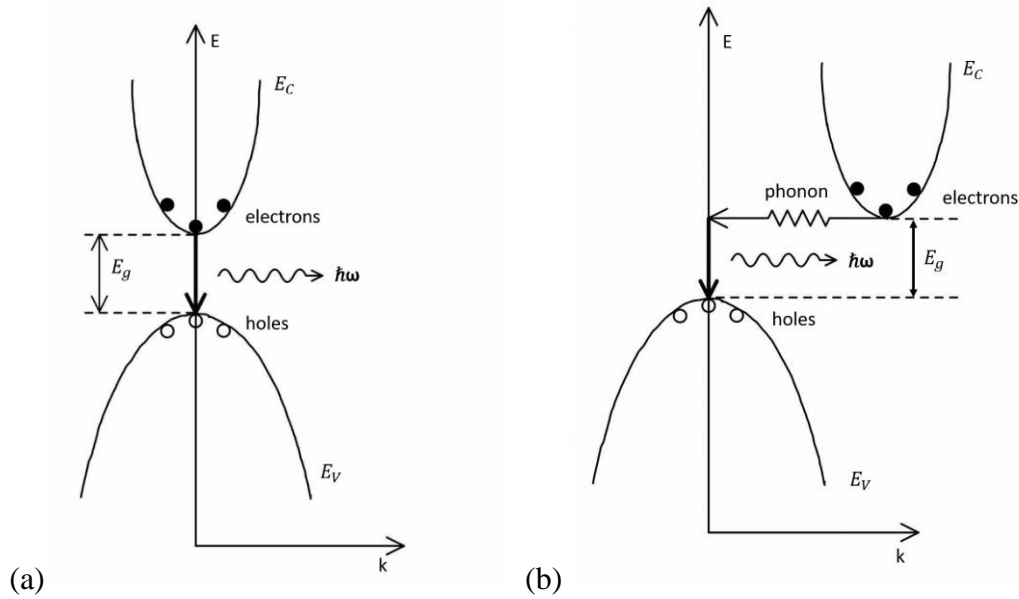
Figure 2. 4 Energy band structure of (a) direct band gap and (b) indirect band gap semiconductor

2.1.4   Doping

Unlike metal or insulator, a good or poor electrical conductor, a semiconductor is the material in between that can control the properties by introducing a small number of dopants into the semiconductor material. This process is called doping, making the semiconductor highly metallic, reasonably insulating, or anywhere in between. When a semiconductor is doped with donor or acceptor impurities, impurity energy levels are introduced that usually lie within the energy gap, as shown in Figure 2. 5. The donor level is being neutral if filled by electron, and being positive is empty. On the other hand, the acceptor level is neutral if empty and negative if filled by an electron [12]. In p-type doping, some of the material atoms are replaced by doping atoms that do not have enough electrons to share with the nearest neighbours and make covalent bonds. One of those missing bonds leads to the consequence of introducing a hole into the semiconductor lattice. Conversely, in the n-type semiconductor, the doping atoms have an extra electron without bounds with the nearest neighbours. This electron's binding energy is fragile and easily broken at room temperature, leaving an extra electron moving in the semiconductor lattice.
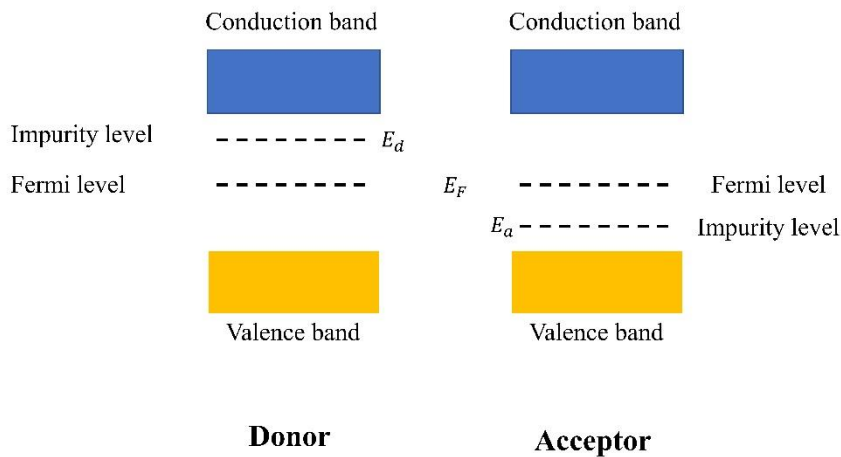
Figure 2. 5 Energy band diagram of doped semiconductor

2.2 Bismuth properties

After decades of development, significant progress has been achieved in semiconductor material for infrared devices. The materials such as HgCdTe, III-V compound semiconductor have continually demonstrated high performance in infrared technology. Because of its tuneable bandgap over the infrared spectral range, high absorption coefficient, high carrier mobility, and long carrier lifetime, HgCdTe has maintained its dominated position as the material of choice for infrared applications [13]. However, the development of HgCdTe has suffered from some major limitations, including high cost and difficulties of material growth. Consequently, other materials have been promoted to replace HgCdTe for infrared development.

III-V based compound semiconductor material, such as GaSb and InAs, has demonstrated great potential in exploring the mid-infrared area due to the strong chemical bond and small energy gap. Thus naturally, its application as an infrared detector becomes obvious. Besides, GaSb is also particularly interesting as a substrate material because it is lattice matched to various III-V compounds [14]. The cut-off wavelength of the GaSb and InAs detector is relatively short, making those applications only work in the near-infrared region. Type II superlattice based infrared detector such as InAs/GaSb and InAs/InAsSb [15, 16] can also provide good quantum efficiency. Besides, such detectors have the potential to reduce Auger dark current [17].

However, most reported InAs/GaSb superlattices-based detectors have lower performance than HgCdTe due to shorter minority carrier lifetime [15-17].

The future development of infrared optoelectronic application requires features including low cost and multi-band detection. As shown in Figure 2. 6, most of the research on compound semiconductor material focuses on wide energy gap material. The research on smaller energy gap and mid-infrared detection semiconductor material are relatively limited, leaving a gap for the other novel semiconductor to explore.
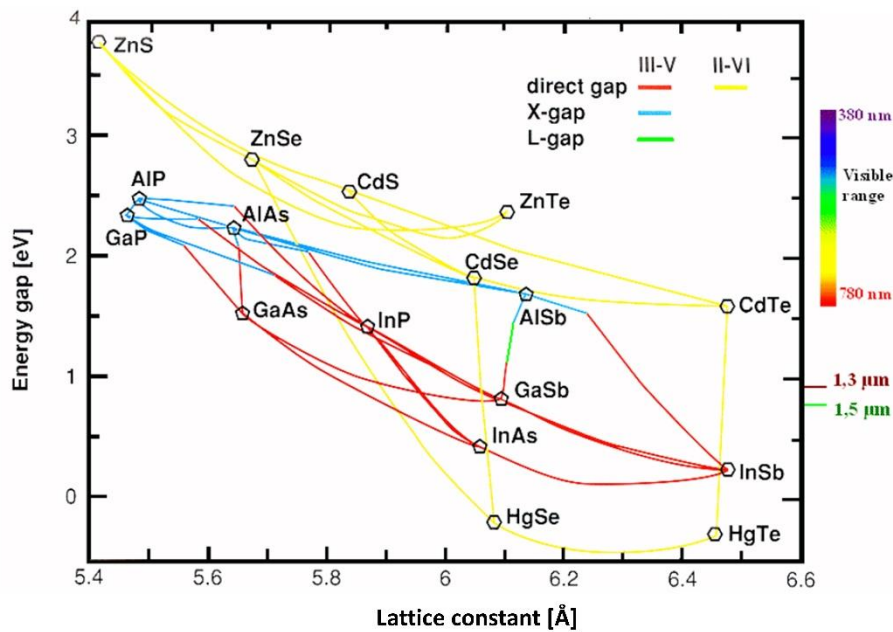
Figure 2. 6 Composition diagram of semiconductor material systems [18]

As one of the typical heavy metal, bismuth has been known as the most diamagnetic of all metals [19]. Meanwhile, the thermal conductivity of bismuth is much lower than most of the other metals. High electrical resistance and the highest Hall effect of any metal also increase the scientific attraction in bismuth-contained compounds [19].

Among bismuth-contained compounds, dilute bismuth semiconductor have generated extensive attention recently [20]. Incorporating a small number of bismuths in general III-V alloys results in a large band-gap reduction and enhanced spin-orbit coupling compared with the host material, which makes it attractive for potential optoelectronic applications in the mid-infrared range [21].

When introducing a small amount of bismuth (Bi) into common III-V compounds, for instance, GaAs, Bi impurity states will be formed close to the host semiconductor's valence band edge

[22]. When Bi is incorporated, the interaction between the valence band and Bi states are expected to lead to a large energy band-gap reduction and stable spin-orbit splitting. In contrast with dilute nitride, which is known to reduce the bandgap by lowering the conduction band edge, Bi on the band structure is primarily in the valence band [19]. As such, this offers a new method to alter the band structure of semiconductor alloys and can have more significant potential for novel optoelectronic application. Moreover, initial results show that electron transport in dilute bismuth materials is much less influenced than those in dilute N materials [23], further supporting the notion that Bi primarily affects the valence band. Table 2. 1 shows the band-gap reduction in dilute bismuths and some III-V compounds at each percent of Bi, and these data are valid only for a small number of x values.

Dilute bismuth	Band-gap reduction (me V/%)
$GaAs_{1-x}Bi_x$ $GaSb_{1-x}Bi_x$ $InAs_{1-x}Bi_x$ $InSb_{1-x}Bi_x$	83 (300 K) [24] 32 (77 K) [25] 100 (4 K) [26] 20 (77 K) [27] 23 (77 K) [27]

(a)

Common III-V ternary compounds (300K) [28]	Band-gap reduction (me V/%)
$In_xGa_{1-x}Asx$ $In_xGa_{1-x}Sbx$ GaN_xAs_{1-x} $GaAs_xSb_{1-x}$ $InAs_xSb_{1-x}$	15 10 156 [29] 19 9

(b)

Table 2. 1 Summary of band-gap reduction in (a) dilute bismuths and (b) some common III-V ternary compounds at each percent of Bi or other incorporated element (x %)[19]

Table 2. 1 (a) shows that the reduction in band-gap is much more dramatic when Bi is introduced compared to more common III-V ternary compounds listed in Table 2. 1 (b). It is interesting to note that dilute nitrides, which are also indicated in the table, have more significant bandgap reduction than any other alloys, even with Bi concentration. However, previous studies on dilute N alloys have shown this is at the cost of severe degradation in the material's electrical properties. The idea of combining the incorporation of N and Bi does present new freedom for band engineering since Bi is mainly effecting the valence band and N is on the conduction band [19].

Introducing Bi into GaAs has been intensively researched in recent years [22, 30-32]. Up to date, the research for $GaAs_{1-x}Bi_x$ compounds is proposed for less than 2µm wavelength range

and primarily for telecommunication applications because the host GaAs has a large band-gap of 1.424 eV (at 300K).

III-Sb semiconductor compounds are very attractive for optoelectronic devices working in mid-infrared. Introducing Bi in III-Sb can also have some potential benefits. First, incorporation of Bi in GaSb can efficiently reduce the band-gap, hereby extending light emission wavelength more efficiently than using InGaSb. Currently, standard quantum well lasers struggle to operate in the 2-4 µm range due to high current leakage and Auger recombination. However, by incorporating Bi, a large valence band offset can be formed, suppressing the hole leakage. Additionally, the spin-orbit splitting energy of GaSb is very close to its direct band-gap. As such, it requires a small amount of Bi in $GaSb_{1-x}Bi_x$ to suppress inter-valence band Auger recombination processes in optoelectronic devices [19].

Other compounds like InSb or InAsSb, also have similar wavelength extend by incorporation of Bi, reaching around 8-12 µm, which is an important atmospheric transmission range. Those changes will enable these novel materials to offer an alternative to HgCdTe, which is dominated in this wavelength range for photo-detection. By comparing with HgCdTe, this novel materials system can have a lower cost, a simple fabrication process and a smaller size when fabricating devices, making this material more competitive. Many other research has been processed on III-V materials such as $InSb_{1-x}Bi_x$, $InAs_{1-x}Bi_x$, however, $GaSb_{1-x}Bi_x$ is rarely explored which provide the potential for further investigation.

2.3 Junctions

To form an electronic device, we need to put materials together. The junction will be formed between the contact. The junction can be generally defined as the metal-metal junction, metal-semiconductor junction and semiconductor-semiconductor junction. Whenever the junction is formed, two materials with different Fermi levels are brought into contact, and free carriers will flow from one material into the other until an equilibrium condition is achieved, which means the Fermi levels of both materials are aligned. The equilibrium means that there is no external potential applied to the system [33].

2.3.1 Metal-metal junction

The energy band diagram example of a metal-metal junction can be found in Figure 2. 7. In this section, Au and Ti have chosen as an example to illustrate the metal-metal junction. It can be seen from Figure 2. 7 that gold has a higher work function than titanium. In this case, the

titanium has a large number of electrons close to the Fermi level. And there is also an abundance of empty state in the gold. When the metal-metal junction is formed, the electrons from titanium with the lower work function can move into gold, and an electrical field will be set up when the junction is formed.

before contact   after contact
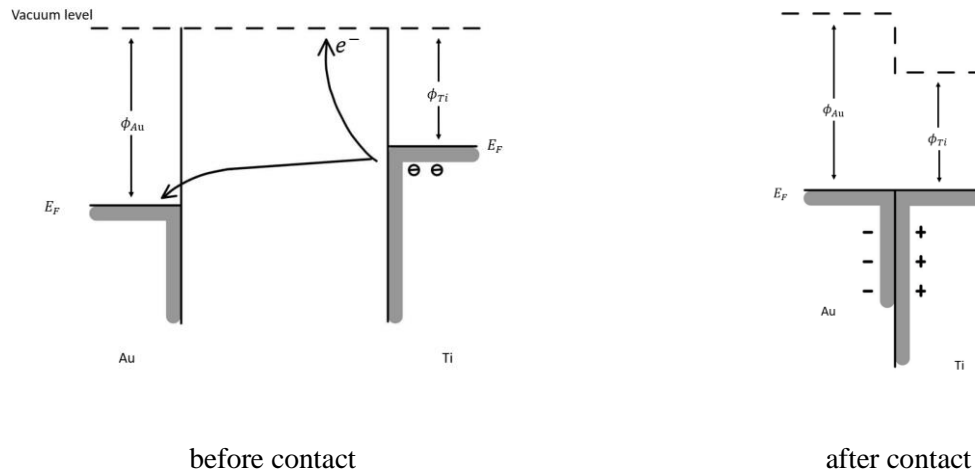
Figure 2. 7 Energy level diagram for metal-metal junctions

2.3.2 Metal-semiconductor junctions

When the metal and semiconductor are brought together, the metal-semiconductor junction will form at the interface. It is useful to understand the mechanism when we form a device on a wafer. These devices have to be connected to an external circuit, usually accomplished by forming the metal contact with these devices. In this way, to understand the metal-semiconductor junction is essential. There are two types of junction formed by metal-semiconductor contact, Schottky junction and Ohmic junction. To define different types of electrical junctions in a metal-semiconductor system, assuming that the work function of the metal ϕ_m and that of the semiconductor ϕ_s are not equal. Therefore, after they brought into intimate contact, the charge transfer between the electrode and the semiconductor will prevail until the Fermi levels of the electrode and semiconductor are aligned to the same height. Depending on the values of ϕ_m, ϕ_s and the type of semiconductor, there are different types of electrical contacts, which are discussed in the following sections.

2.3.3.1 Schottky junction

The Schottky barrier, shown in Figure 2. 8. The condition for a contact to be Schottky is $\phi_m > \phi_s$ for a metal-n-type semiconductor junction (seen by electrons from the metal side), or $\phi_m < \phi_s$ for a metal-p-type semiconductor junction (seen by holes from the metal side). In this

chapter, we will discuss n-type semiconductor as an example. In this condition, electrons will flow from the semiconductor to the metal, leaving a depletion region in the semiconductor, as shown in Figure 2. 8. Where W is the width of the depletion region, and ϕ_B is the height of the potential barrier that an electron in the metal must surmount to pass into the semiconductor. The electrons can flow easily from the semiconductor to the metal under the forward bias in this contact. In contrast, under reverse bias, the flow of electrons from the metal is limited by the electrons available over the Schottky barrier. The density of which is much smaller than that in the bulk of the semiconductor. It can be seen as one that creates a depletion region extended from the interface to the semiconductor inside. In this way, the Schottky junction under bias behaves as a rectifier [33]. The conducting mechanism of electron emission from a metal across the Schottky contact may be due either to the thermionic process or a tunnelling process. These will be discussed in the next section.

before contact   after contact
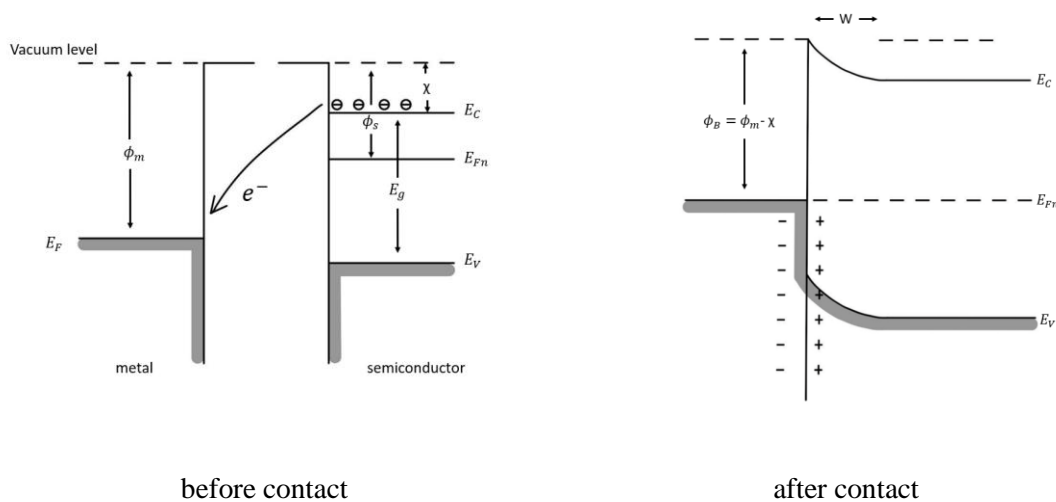
Figure 2. 8 Energy level diagrams for a Schottky contact between a metal and an n-type semiconductor

2.3.3.2 Ohmic contact

An Ohmic contact between a metal and semiconductor can be described as a negligible resistance relative to the series impedance of the semiconductor device. This implies that the free carrier density at and in the vicinity of the contact is much greater than that in the bulk of the semiconductor. An ohmic contact can also be defined as one that creates an accumulation extended from the interface to the inside of the semiconductor. In general, there are two methods to make ohmic contact. One of which is choosing metals of low work function so that $\phi_m < \phi_s$ for metal-n-type semiconductor junction or choosing metals of high work functions so that $\phi_m > \phi_s$ for metal-p-type semiconductor junction. The energy level diagrams were

presented in Figure 2. 9. This process lowers the potential barrier for efficient thermionic emission to make the free carrier density higher at the contact than that in the bulk of the semiconductor. Another method of forming an ohmic contact is doping the semiconductor surface heavily near the contact to make the potential barrier thin enough for efficient quantum-mechanical tunnelling.

It is usually challenging to find a suitable metal with $\phi_m < \phi_s$ for the ohmic contact to the n-type semiconductor, or with $\phi_m > \phi_s$ for the ohmic contact to the p-type semiconductor. Furthermore, most semiconductors for electronic devices are covalently bonded, so they have surface states. For these reasons, it is not possible to produce an ohmic contact simply based on choosing a suitable metal. The method to obtaining reliable ohmic contacts for most semiconductor devices is based on the dopant, that is, producing a very thin layer heavily doped with dopants by either diffusion, ion implantation techniques or annealing of the metal to make this layer degenerate. After this layer has been produced, any metal or alloy can be deposited on this layer's surface to form a good ohmic contact. In this thesis, most ohmic contacts are formed under this method.

before contact   after contact
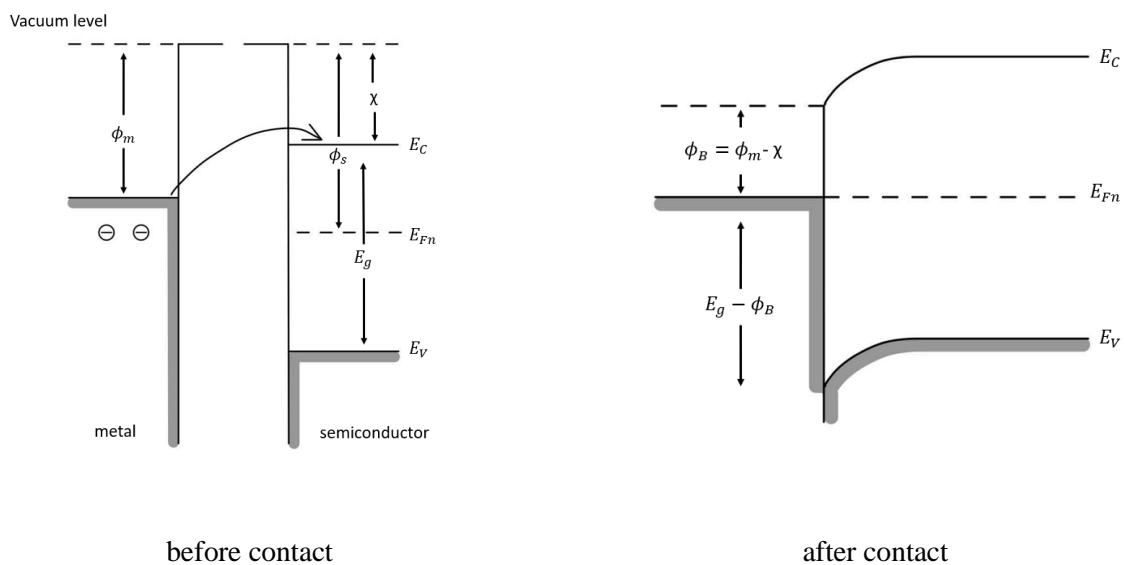
Figure 2. 9 Energy level diagrams for an Ohmic contact between a metal and an n-type semiconductor

2.3.3 Semiconductor junctions

The majority of the optoelectronic devices utilise no-homogeneous semiconductor structure to achieve the photoelectric effect. The properties of semiconductor junctions are also important when forming complex device structures such as infrared detector, type II superlattice, interband cascade laser, and quantum well laser structure.

2.3.3.1 Pn junction

A pn junction is formed between a p-type semiconductor and an n-type semiconductor as one of typical semiconductor-semiconductor contact. Usually, the pn junction formed from the same material is called homojunction. The pn junction can also from different material; such type of junction is called heterojunction. In order to form a homojunction interface, a semiconductor material is used to doping one side into p-type and the other side into n-type. In the heterojunction case, the material has to be chosen carefully so a good interface can form without any defects at the interface, which has increased some restrictions on the junction they formed. To form a pn junction, we bring the p-type and n-type semiconductor together. An example of the energy band diagram of pn junction can be found in Figure 2. 10. At equilibrium, the Fermi levels will line up, which on the side of the n-type semiconductor there are existed electrons at the conduction band, and these electrons can move to the p-type semiconductor. On the side of p-type semiconductor, the existing holes at the valence band, and these holes can move to the n-type semiconductor. This mechanism will lead to a contact potential between the pn junction.

before contact   after contact
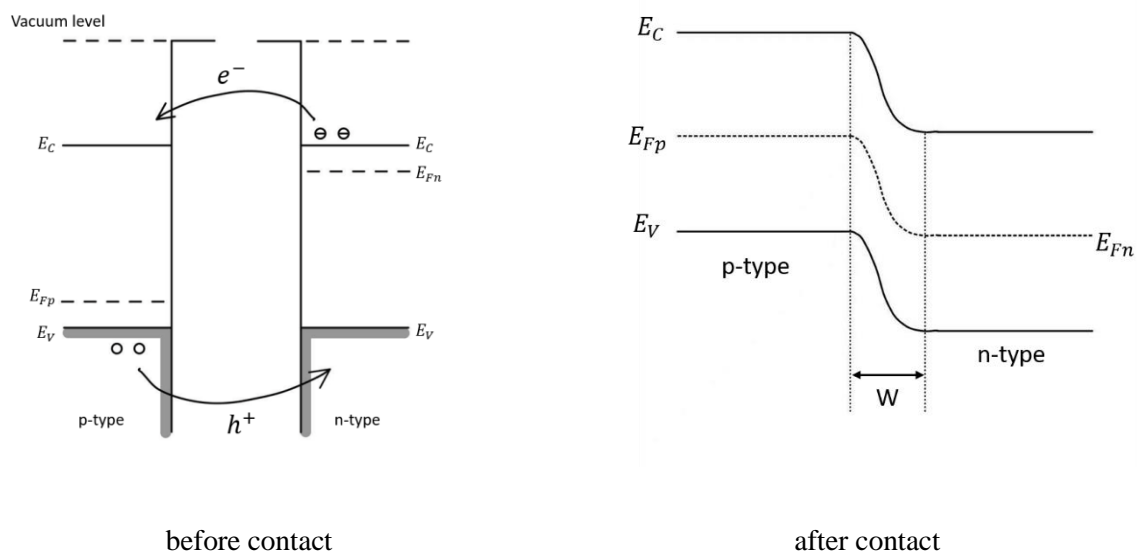
Figure 2. 10 Energy level diagrams for a pn junction

A simplified schematic of the pn junction can be found in Figure 2. 11. It can be seen that the depletion region formed in between. Since the electrons move from the n-type side to the p-type side, which leaves the net positive charge in the n-type side, and these positive charges refer to the donor ions. Similarly, there is a net negative charge in the p-type side because the holes from the p-type side move to the n-type side, leaving behind the acceptor ions and the

acceptor ions are negative. The relationship of the depletion width and the concentration of ions can be estimated by equation

$$\frac{W_p}{W_n} = \frac{N_D}{N_A}$$

(2- 1)

where W_p and W_n is the depletion width of p-type and n-type, the N_D and N_A represent the donor and acceptor consternation, respectively. The ratio of the depletion region width on the p-type and n-type side is inversely proportional to the concentration of the dopants. There are certain pn junction that is formed between the heavily doped p^+ region and a n region. In this particular case, N_A is usually greater than N_D, using the Eq. (2- 1), we have W_p is much smaller than W_n, so the depletion region is almost in the n-type side. Another extreme example of this can be found in the metal-semiconductor Schottky junction, in which the depletion region can be found on the semiconductor region. Because the charge density in the case of metal is much higher than that of semiconductor, in order to maintain to the charge neutrality, electrons are coming from the surface of the semiconductor to create the depletion region. This depletion region stays entirely on the semiconductor side.
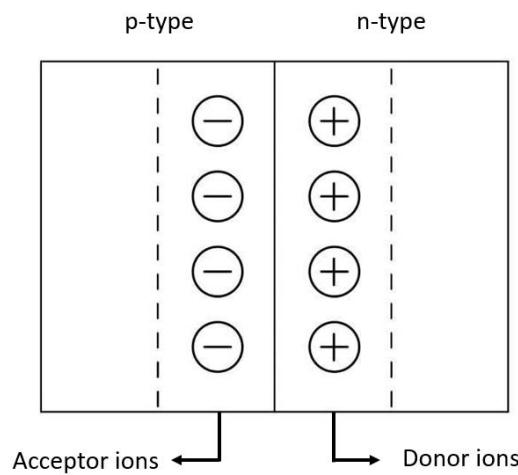
Figure 2. 11 Schematic of a pn junction

A comparison of the performance of Schottky diode and pn junction diode can be found in the Table 2. 2

Characteristics	Schottky diode	pn junction diode
Forward current mechanism	Majority carrier transport	Diffusion current (minority carrier transport)
Reverse current	Less temperature-dependent	Strong temperature-dependent
Switching speed	Fast respond (extremely small charge-storage time)	Limited by the recombination process
Breakdown voltage	Lower breakdown voltage	Comparatively large

Table 2. 2 Comparisons of Schottky diode and pn junction diode

The structure of pn junction has been widely used into the device such as a photodetector. The photodiode can transfer each photon from received optical signal into free electron instantaneously to generate photocurrent in an ideal situation. However, not every incoming photon can generate electron in a suitable semiconductor material caused by the non-efficient photoabsorption and carrier collection. A well-known method used to increase photon absorption efficiency is to insert a wide and undoped intrinsic layer between p-type and n-type semiconductors. The main advantages of a p-i-n diode structure are that the width of the depletion region can be significantly increased and determined in the fabrication, and the build-in electrical field is uniformed in the intrinsic region [34].

2.4 Conduction mechanism

The current transport in metal-semiconductor contact is mainly due to the majority carriers transport between the junction or pn junction where the minority carriers are responsible. In general, there are four different conduction mechanisms by which transport can occur: (a) thermionic emission, (b) tunnelling through the barrier, (c) recombination in the depletion region and (d) diffusion. In Schottky diodes, the thermionic emission is the dominant conduction mechanism, and such diodes are referred to as ideal Schottky diode. While the process of (b), (c), and (d) cause a departure from this ideal behaviour. In practice, the behaviour of the diode will lie somewhere between the diffusion theory and the thermionic emission theory.

2.4.1 Thermionic emission

The thermionic emission (TE) conduction theory is that the electron emitted over the barrier from the semiconductor into the metal. The electron must have enough energy to move through the high field depletion region. The emission of electrons into the metal is controlled by the density of available states in the metal. It is assumed in the TE theory that the effect of drift and diffusion process in the depletion region is negligible, the barrier height is much greater than kT, the Fermi level for the electrons remain flat throughout the depletion region and the

thermal equilibrium is established [35]. Since the barrier height of electron transport from semiconductor to metal is remain the same under bias, the current flowing through the junction is thus unaffected by the applied bias. The total current density [12] can be given by

$$J_n = J_{TE}[exp\left(\frac{qV}{kT}\right) - 1]$$ (2- 2)

and

$$J_{TE} = A^*T^2 exp(-\frac{q\phi_B}{kT})$$ (2- 3)

where J_{TE} is the saturation current density in A/cm^2, A^* is the effective Richardson constant in A/cm^2 $-$ K^2, ϕ_B is the barrier height in V, k is the Boltzmann constant in J/K, and T is the absolute temperature in K.

2.4.2 Diffusion

Before the electron can be emitted over the barrier into the metal, electrons must first be transported from the semiconductor to the interface. During the transmission process in the depletion region in semiconductor, the electron motion is under the usual mechanisms of diffusion and drift in the electric field of the barrier. Unlike the TE theory, where the Fermi level for both types of carriers is assumed to be flat throughout the depletion region. According to the diffusion theory, the Fermi level is assumed to be droop down through the depletion region. It is also an assumption in the diffusion theory that the concentration of conduction electrons in the depletion region in the semiconductor is unaffected by the bias voltage, the impurity concentration of the semiconductor is nondegenerate, and the barrier height is greater than kT [12, 35]. The expression of the diffusion theory for the diode current [36] can be found as:

$$J_n = J_D[exp\left(\frac{qV}{kT}\right) - 1]$$ (2- 4)

and

$$J_D = qSN_C\mu\mathcal{E}_m exp(-\frac{q\phi_B}{kT})$$ (2- 5)

where J_D is the saturation current density in A/cm^2, S is the diode cross-section area, N_C is the effective density of states in conduction band in cm^{-3}, μ is the electron mobility in cm^2/V-s and $\mathcal{E}_m$ is the maximum electric field in V/cm. All the other symbols have their usual meaning. The

current density equation for both TE theory Eq. (2- 2) and diffusion theory Eq. (2- 4) are similar. However, comparing Eq. (2- 3) and Eq. (2- 5), the saturation current density for the diffusion theory is much less depending on temperature and is more effective by the applied bias compared to TE theory.

2.4.3 Carrier generation and recombination in the depletion region

At zero bias the depletion region of the Schottky barrier is in thermal equilibrium, and the rate of electron-hole pair generation in this region is balanced by the rate of recombination. In the presence of bias voltage, the balance of the electron-hole pair will depart, and there will be a net generation process or net recombination of the carriers depends on the applied bias. In the case of a forward voltage applied to the Schottky junction made by a metal-n-type semiconductor, the electrons will be injected into the depletion region from the neutral bulk semiconductor holes will travel through the junction from the metal. These excess electron-hole pairs will recombine in the depletion region to generate a forward recombination current. If a reverse voltage is applied, the electron-hole pairs in excess of their thermal equilibrium value will be generated into the depletion region. These pairs will be swept out by the electric field of the barrier and causing a reverse current [36]. The current generated by the carrier generation and recombination in the depletion region can be expressed as [38]:

$$I = I_{R0}[exp(qV/2kT) - 1] \tag{2- 6}$$

and

$$I_{R0} = \frac{qSn_iW}{2\tau_0} \tag{2- 7}$$

where S is the diode cross-section area, τ_0 is the minority lifetime in the depletion region, n_i is the root of the electron-hole product, and W is the width of the depletion region. It is noted that the generated current is when the junction is reverse bias. While the junction is forward bias, the current is a recombination current. The recombination current is a common cause of the departure from ideal behaviour in the Schottky diode.
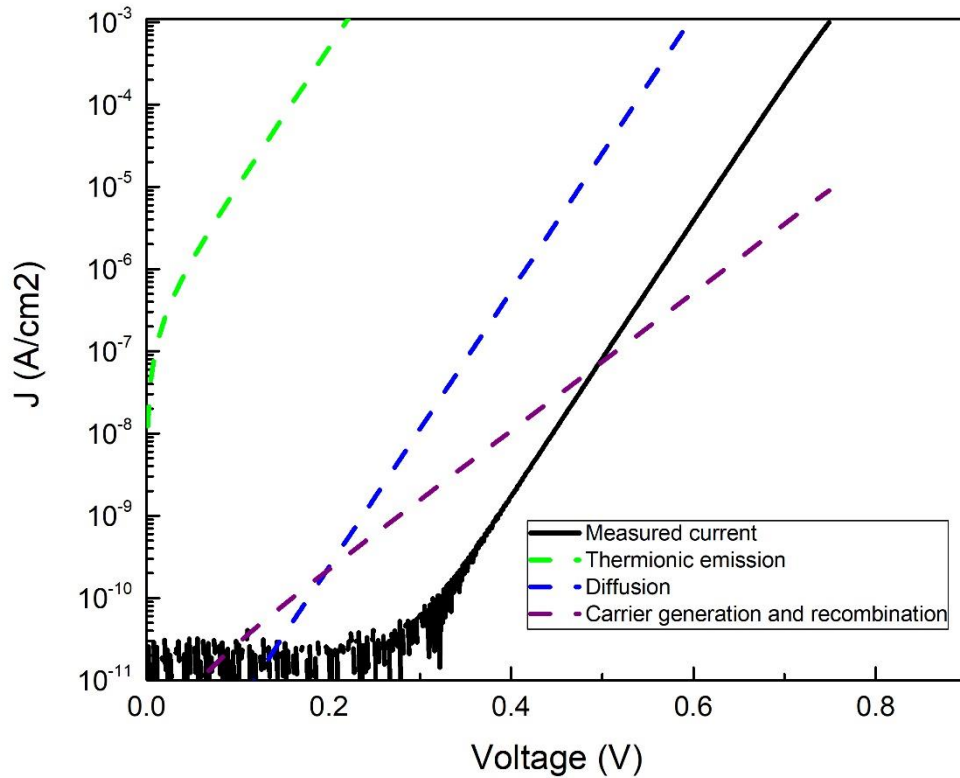
Figure 2. 12 Forward JV characteristics of a diode with different conduction mechanism simulation

An example of a diode forward JV characteristics has used to compare with the theoretical simulation of different conduction mechanism. The parameters used for the simulation have been listed in the appendix. While the figure used here is as an example to illustrate the JV characteristics of different conduction mechanism under particular circumstance, as each parameter presented in the appendix. It is less likely to observe one conduction mechanism for a practical diode. Therefore, the Figure 2. 12 may only be used as an example to understand the process of different conduction mechanism and how they may be used to identify the dominate process or differing regions within experimental data.

2.4.4 Tunnelling through the barrier

Besides the TE and diffusion theories, the electron with energies below the top of the barrier can also be transported through the barrier by quantum mechanical tunnelling. There are two types in which tunnelling can occur over the barrier junction, field emission (FE) and thermionics field emission (TFE). In the case of FE, the semiconductor is assumed to be doped to degeneracy, the depletion region is very thin, and at low temperatures, electrons with energy

close to the Fermi level can tunnelling through the semiconductor into the metal. As for TFE, if the temperature increases, many electrons are excited to higher energies. These electrons can tunnel in the metal before reaching the top of the barrier. The barrier height and thickness decrease since the number of electrons decreases rapidly with energy above the Fermi level. There is an energy level E_m which contribute to the maximum TFE level. If the temperature further increased, a limit is reached at which all the electrons can reach and travel through the barrier; at this point, the conduction mechanism is TE dominates [36].

The relative contributions of TE, EF and TFE depend on both temperature and doping level. The criterion can be set by comparing the thermal energy kT and E_{00} which is defined as [12]:

$$E_{00} = \frac{q\hbar}{2}\sqrt{\frac{N}{m^*\varepsilon_S}}$$
(2- 8)

where $\hbar$ is the reduced Planck constant in J-s, N is the doping concentration in cm^{-3}, m^* is the effective mass in kg and is the permittivity of the semiconductor. In the case when $kT \gg E_{00}$, the conduction mechanism is dominating by TE. When $kT \ll E_{00}$, FE dominates. And when $kT \approx E_{00}$, TFE is the main mechanism. The current density expression of FE under forward bias can be express as [37]:

$$J_{FE} = \frac{A^{**}T\pi exp[-\frac{q(\phi_B-V)}{E_{00}}]}{c_1 k sin(\pi c_1 kT)}$$
(2- 9)

where

$$c_1 \equiv \frac{1}{2E_{00}} log\left[\frac{4(\phi_B-V)}{-\phi_n}\right]$$
(2- 10)

And ϕ_n is the Fermi potential from conduction band edge in n-type semiconductor express as

$$\phi_n = \frac{E_F-E_V}{q}$$
(2- 11)

Where E$_F$ is Fermi level and E$_V$ is top edge of valence band in eV.

The equation for TFE under forward bias can be expressed as:

$$J_{TFE} = \frac{A^{**}T\sqrt{\pi E_{00}q(\phi_B-\phi_n-V)}}{k cosh(E_{00}/kT)} exp\left[\frac{-q\phi_n}{kT} - \frac{q(\phi_B-\phi_n)}{E_0}\right] exp(\frac{qV}{E_0})$$
(2- 12)

$$E_0 \equiv E_{00} coth(\frac{E_{00}}{kT})$$

(2- 13)

Where ϕ_n is the Fermi potential from conduction-bang edge in n-type semiconductor in V.

2.4.5 Reverse characteristics

In the thermionic emission theory, the reverse current density of a Schottky barrier junction should saturate at the value $J_{TE} = A^*T^2 exp(-\frac{q\phi_B}{kT})$. However, this saturate value cannot be observed in a practical diode; instead, there are some causes of departure from ideal behaviour.

One of the common causes is the field dependence of the barrier height. It is certain that the reverse current will not saturate if the barrier height depends on the reverse bias. Since the barrier height is reduced with increasing electric field inside the barrier [12]. The reverse bias increase with the electric field, making the reverse current to increase as $exp(-\frac{q\Delta\phi_B}{kT})$, where $\Delta\phi_B$ is the barrier lowering at reverse bias. The method used to lowering barrier including image force and dipole formation [39, 40], the primary cause of barrier lowering is the image force on the electron emitted from the metal into the semiconductor, it can be accounted as the reason to explain the departure of the reverse current from ideal.

Besides the barrier lowering, another mechanism that causes the reverse current depart from ideal is tunnelling of the electrons from the metal into the semiconductor conduction band through the barrier. As same as forward characteristics, the tunnelling can occur either as FE or TFE where electrons can enter at lower doping level at reverse bias case than for forward bias case. This is because a moderate reverse bias causes the potential barrier to become sufficiently thin enough for tunnelling of electrons before reaching the top can be emitted into the semiconductor by TFE [36].

Another mechanism causing the reverse current behaviour is the electron-hole pair generation in the depletion region. When the effects of image force lowering the barrier height and tunnelling are reduced to negligible by using a low donor density, there may be a considerable reverse current causing by the generation in the depletion region. Like the recombination in the forward bias, the generation current is important for large barrier heights and in low-lifetime semiconductors. It is also important at low temperature because it has lower activation energy than the thermionic-emission component.

2.5   Photodetector

Photodetectors are semiconductor devices that can detect incident photon or radiation through the electronic process. The performance of the photodetector is measured by its dark current, responsivity, bandwidth and spectral range [41]. Generally, the operation of a photodetector has three steps involved when we think about shining light onto a device and converting it into electrical current. First, the incident light generates carriers (electron-hole pair) in the devices. Once these carriers are generated, they need to be transported to the electrodes; sometimes, carrier multiplication is also possible. Finally, these carriers are then extracted out of the device in the form of current. When we look at the photodetector, there usually are two class of photodetector. First-class, we have a thermal detector. In this case, the light is incident on the device, which lead to a temperature rise. The raised temperature is directly proportional to the amount of light that is shining on the devices. It has been widely used in infrared radiation devices. The other class is the photon detector. In this type of device, the photon generates electron-hole pairs. In this thesis, we will mainly be dealing with the photon detector.

2.5.1   Metal semiconductor metal photodetector

Metal semiconductor metal (MSM) photodetector is the type of device based on the metal-semiconductor junction. Two Schottky barriers connected back-to-back on a coplanar surface, and the metal contacts usually have an interdigit shape. When the light beam exposes on the MSM, the light is received at the metal contact gap. A general MSM photodetector is shown in Figure 2. 13. (a). Unlike regular metal-semiconductor photodiode using photoexcitation over the barrier for conduction, in the MSM photodetector generation is through band-to-band excitation [12]. In typical operation, the photocurrent first increased with voltage and then reached saturated. This is due to the expansion of the depletion region in the reverse-biased Schottky junction. An example of the current-voltage (IV) characteristics of GaSbBi MSM photodetector has presented in Figure 2. 13. (b). The MSM photodetector has the advantages of high speed, and it is simple to fabricate into the device, which makes MSM a good candidate as an optoelectronic device to characteristics the semiconductor material. The main drawback of MSM photodetector is significant dark current due to the Schottky-barrier junction and a limited responsivity.
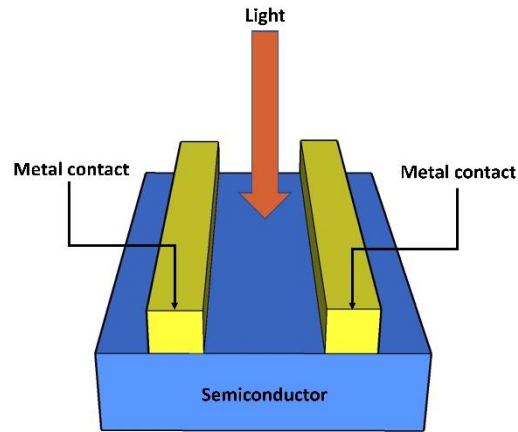
(a)
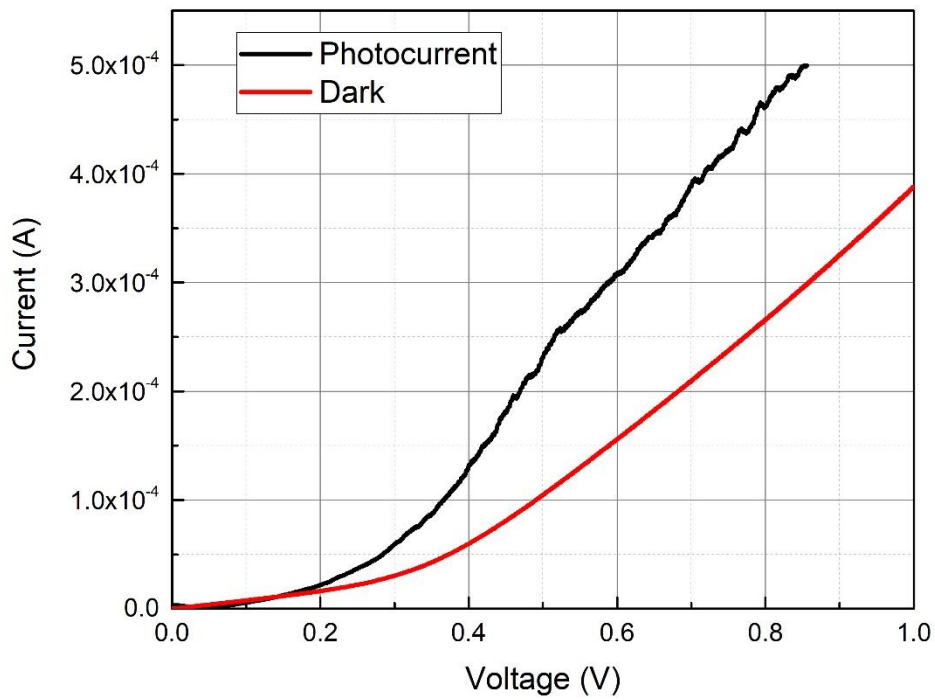
(b)

Figure 2. 13 (a) Schematic diagram of a general MSM photodetector device and (b) IV characteristics of a GaSbBi MSM photodetector

2.5.2 Avalanche photodiodes

Avalanche photodiodes (APDs) are operated at a high reverse-bias voltage where avalanche multiplication takes place. In the case of the photodiode, it can be defined by a pn junction or

the p-i-n junction. The electron-hole pairs are generated either in the depletion region of the pn junction or generated in the instinct region of the p-i-n junction. These electron-hole pairs are then separated by applying a reverse bias to the junction where the electrons go to the n-type side, and the holes go towards the p-type side to form the current. Considering a p-i-n photodiode under reverse bias, when the incident light shining on the device, the light generates electron in the conduction band and hole in the valence band. Because of reverse bias, these electrons and holes are separated, and they contribute to the current. There will be a small current in the absence of light, and this current is the saturation current of the device. The current is enhanced when the light is shining on the device due to the generated electrons and holes. In this case, p-type and n-type semiconductors tend to be very thin, so most of the absorption occurs within the intrinsic region. An example of the device schematic has presented in Figure 2. 14. (a).
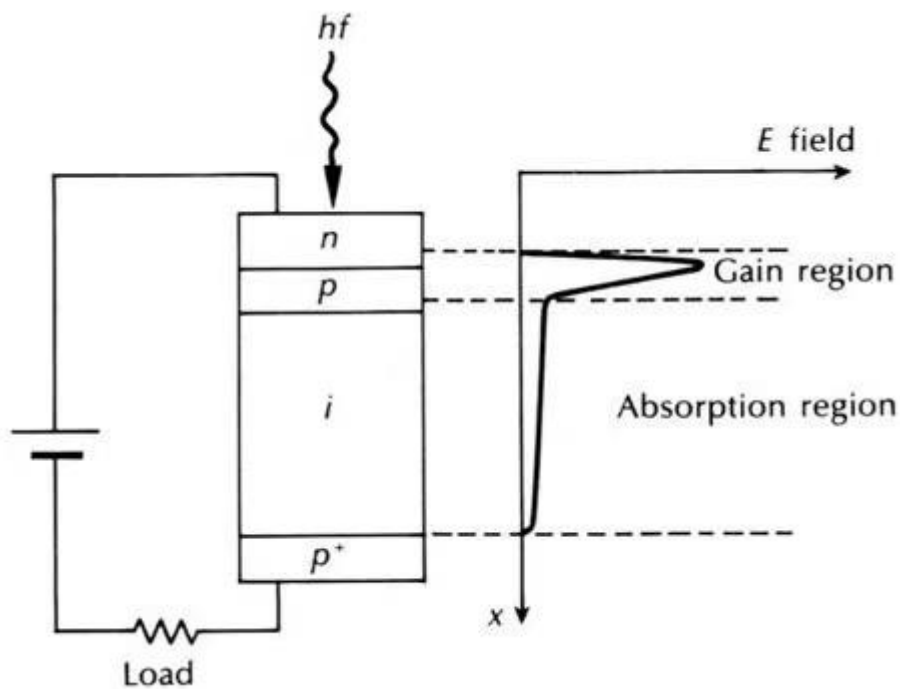
(a)
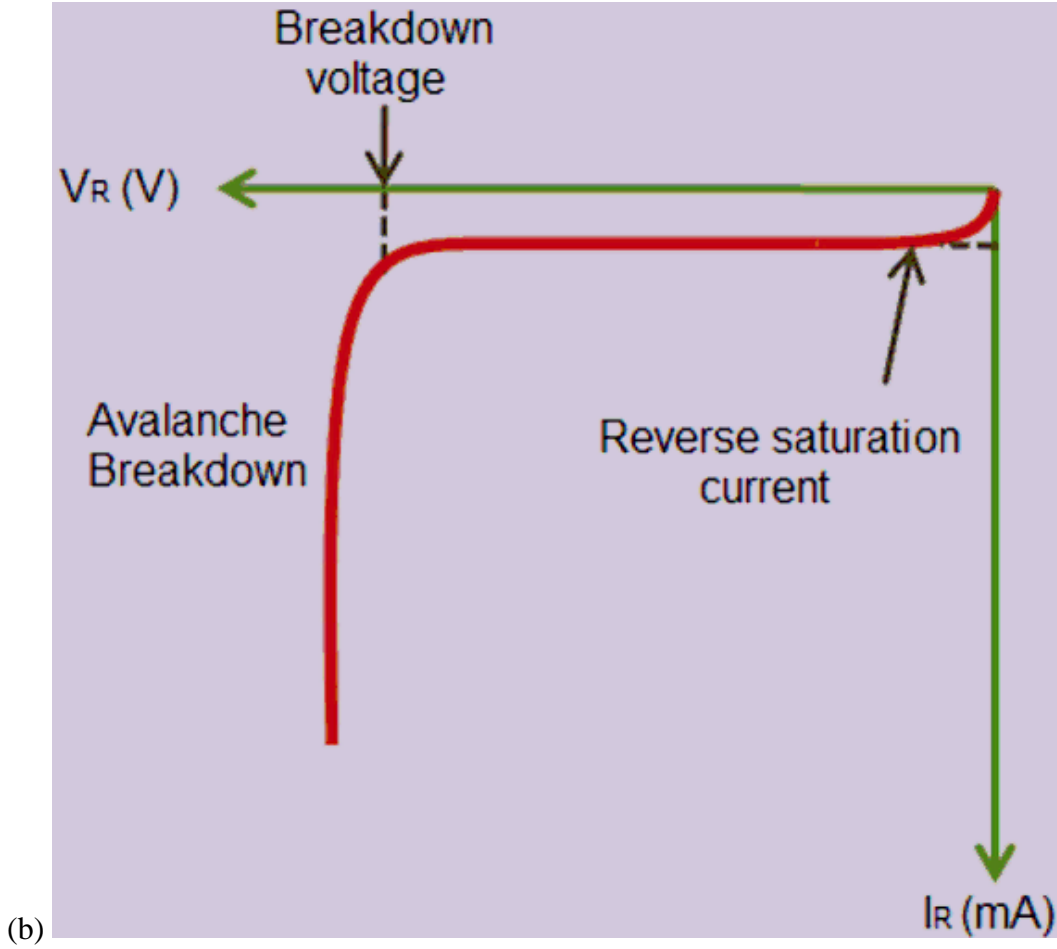
Figure 2. 14 (a) device schematic of an APDs and current-voltage characteristics of avalanche breakdown [42]

The avalanche gain (M) for the electrons can be expressed as [12]:

$$M = \left\{1 - \int_0^{W_D} \alpha_n exp\left[-\int_x^{W_D}(\alpha_n - \alpha_p)dx'\right]dx\right\}^{-1} \qquad (2\text{-}14)$$

where W_D is the depletion layer width, α_n is the electron ionization rate, and α_p is the hole ionization rate. As for a p-i-n diode where the ionization coefficients are position-independent, the avalanche gain is given by [12]:

$$M = \frac{\left(1-{\alpha_p}/{\alpha_n}\right)exp\left[\alpha_n W_D(1-{\alpha_p}/{\alpha_n})\right]}{1-\left({\alpha_p}/{\alpha_n}\right)exp\left[\alpha_n W_D(1-{\alpha_p}/{\alpha_n})\right]} \qquad (2\text{-}15)$$

In terms of equal ionization, where α_n equals to α_p, the avalanche gain is then given by the simple form [12]:

$$M = {1}/{1 - \alpha W_D}, \qquad (2\text{-}16)$$

while the breakdown voltage of the diode corresponds to the situation where αW_D equals to 1. The breakdown voltage of the APDs is usually depended on the doping density while increasing the doping density can reduce the breakdown voltage. An example of a typical breakdown voltage is presented in Figure 2. 14. (b).

A various semiconductor material has been used to fabricate into APDs including Si and III-V compounds alloys. Si APDs are working well at the radiation from 0.6 to 1 μm with a high value of quantum efficiency [12]. Since the ionization coefficient ratio in the Si depends on the electric field of the diode, lowering the electric field at the avalanche breakdown can minimise noise. III-V alloys based APDs also have many advantages compare to Si APDs, including changeable wavelength response by adjusting the alloy composition, high absorption coefficient, high quantum efficiency, high-speed performance of the device. The main advantage of III-V heterojunction APDs can use higher bandgap structure material in the multiplication region while keeping the lower bandgap material for light absorption. This type of structure can effectively prevent edge breakdown. Moreover, the noise effect can be further reduced if the multiplication region of the III-V heterojunction APDs is thin enough.

2.6   Reference

[1]   B. G. Yacobi, *Semiconductor materials: an introduction to basic principles*. Springer Science & Business Media, 2003.

[2]   G. Harbeke, *Polycrystalline Semiconductors: Physical Properties and Applications: Proceedings of the International School of Materials Science and Technology at the Ettore Majorana Centre, Erice, Italy, July 1–15, 1984*. Springer Science & Business Media, 2012.

[3]   L. Kazmerski, *Polycrystalline and amorphous thin films and devices*. Elsevier, 2012.

[4]   J. F. Wager and R. Hoffman, "Thin, fast, and flexible," *Ieee Spectrum,* vol. 48, no. 5, pp. 42-56, 2011.

[5] C. Pande, B. Rath, and M. Imam, "Effect of annealing twins on Hall–Petch relation in polycrystalline materials," *Materials Science and Engineering: A,* vol. 367, no. 1-2, pp. 171-175, 2004.

[6] T. Hickmott, "Annealing of surface states in polycrystalline-silicon–gate capacitors," *Journal of Applied Physics,* vol. 48, no. 2, pp. 723-733, 1977.

[7] I. S. Golovina, M. Falmbigl, A. V. Plokhikh, T. C. Parker, C. Johnson, and J. E. Spanier, "Effect of annealing conditions on the electrical properties of ALD-grown polycrystalline $BiFeO_3$ films," *Journal of Materials Chemistry C,* vol. 6, no. 20, pp. 5462-5472, 2018.

[8] J. Miao and B. Liu, "II–VI semiconductor nanowires: ZnO," in *Semiconductor Nanowires*: Elsevier, 2015, pp. 3-28.

[9] P. Hofmann, *Solid state physics: an introduction*. John Wiley & Sons, 2015.

[10] J.-P. Colinge and C. A. Colinge, *Physics of semiconductor devices*. Springer Science & Business Media, 2005.

[11] K. W. Böer, "Bands and Band Gaps in Solids," in *Handbook of the Physics of Thin-Film Solar Cells*: Springer, 2013, pp. 105-147.

[12] S. M. Sze and K. K. Ng, *Physics of semiconductor devices*. John wiley & sons, 2006, pp. 134-187.

[13] W. Lei, J. Antoszewski, and L. Faraone, "Progress, challenges, and opportunities for HgCdTe infrared materials and detectors," *Applied Physics Reviews,* vol. 2, no. 4, p. 041303, 2015.

[14]   A. Rogalski, P. Martyniuk, and M. Kopytko, "InAs/GaSb type-II superlattice infrared detectors: Future prospect," *Applied physics reviews,* vol. 4, no. 3, p. 031304, 2017.

[15]   N. Gautam *et al.*, "Barrier engineered infrared photodetectors based on type-II InAs/GaSb strained layer superlattices," *IEEE Journal of Quantum Electronics,* vol. 49, no. 2, pp. 211-217, 2012.

[16]   A. Haddadi, G. Chen, R. Chevallier, A. Hoang, and M. Razeghi, "InAs/InAs$_{1-x}$Sb$_x$ type-II superlattices for high performance long wavelength infrared detection," *Applied Physics Letters,* vol. 105, no. 12, p. 121104, 2014.

[17]   A. Rogalski, J. Antoszewski, and L. Faraone, "Third-generation infrared photodetector arrays," *Journal of applied physics,* vol. 105, no. 9, p. 4, 2009.

[18]   H. Foll. "Semiconductor I." Oct, 2019. [Online]. Available: https://www.tf.uni-kiel.de/matwis/amat/semi_en/kap_5/backbone/r5_1_4.html. [Accessed Feb. 15, 2021].

[19]   H. Li and Z. M. Wang, *Bismuth-containing compounds*. Springer, 2013.

[20]   D. Samajdar and S. Dhar, "Influence of Bi-related impurity states on the bandgap and spin–orbit splitting energy of dilute III–V-Bi alloys: InP$_{1-x}$Bi$_x$, InAs$_{1-x}$Bi$_x$, InSb$_{1-x}$Bi$_x$ and GaSb$_{1-x}$Bi$_x$," *Superlattices and Microstructures,* vol. 89, pp. 112-119, 2016.

[21]   M. K. Rajpalke *et al.*, "High Bi content GaSbBi alloys," *Journal of Applied Physics,* vol. 116, no. 4, p. 043511, 2014.

[22]   A. R. Mohmad, F. Bastiman, J. Ng, S. Sweeney, and J. David, "Photoluminescence investigation of high quality GaAs$_{1-x}$Bi$_x$ on GaAs," *Applied Physics Letters,* vol. 98, no. 12, p. 122107, 2011.

[23]   D. Cooke, F. Hegmann, E. Young, and T. Tiedje, "Electron mobility in dilute GaAs bismide and nitride alloys measured by time-resolved terahertz spectroscopy," *Applied physics letters,* vol. 89, no. 12, p. 122103, 2006.

[24]   S. Francoeur, M.-J. Seong, A. Mascarenhas, S. Tixier, M. Adamcyk, and T. Tiedje, "Band gap of $GaAs_{1-x}Bi_x$, 0< x<3.6%," *Applied physics letters,* vol. 82, no. 22, pp. 3874-3876, 2003.

[25]   V. Germogenov, Y. I. Otman, and V. Chaldyshev, "Width of the band gap in $GaSb_{1-x}Bi_x$ solid solutions," *Soviet Physics--Semiconductors(English Translation),* vol. 23, no. 8, pp. 942-3, 1989.

[26]   S. Das, T. Das, S. Dhar, M. De La Mare, and A. Krier, "Near infrared photoluminescence observed in dilute GaSbBi alloys grown by liquid phase epitaxy," *Infrared physics & technology,* vol. 55, no. 1, pp. 156-160, 2012.

[27]   S. Barnett, "Direct E_0 energy gaps of bismuth-containing III–V alloys predicted using quantum dielectric theory," *Journal of Vacuum Science & Technology A: Vacuum, Surfaces, and Films,* vol. 5, no. 5, pp. 2845-2848, 1987.

[28]   I. Vurgaftman, J. Meyer, and L. Ram-Mohan, "Band parameters for III–V compound semiconductors and their alloys," *Journal of applied physics,* vol. 89, no. 11, pp. 5815-5875, 2001.

[29]   M. Kondow, K. Uomi, K. Hosomi, and T. Mozume, "Gas-source molecular beam epitaxy of GaN_xAs_{1-x} using a N radical as the N source," *Japanese journal of applied physics,* vol. 33, no. 8A, p. L1056, 1994.

[30]   R. Maspero, S. Sweeney, and M. Florescu, "Unfolding the band structure of GaAsBi," *Journal of Physics: Condensed Matter,* vol. 29, no. 7, p. 075001, 2016.

[31]   X. Lu, D. Beaton, R. Lewis, T. Tiedje, and Y. Zhang, "Composition dependence of photoluminescence of GaAs 1− x Bi x alloys," *Applied physics letters,* vol. 95, no. 4, p. 041903, 2009.

[32]   A. Mascarenhas, B. Fluegel, S. Francoeur, S. Tixier, E. Young, and T. Tiedje, "Giant Spin-Orbit Bowing in GaAs1-xBix," in *APS Meeting Abstracts*, 2007.

[33]   K. C. Kao, *Dielectric phenomena in solids*. Elsevier, 2004.

[34]   R. Hui, *Introduction to fiber-optic communications*. Academic Press, 2019.

[35]   E. H. Rhoderick and R. H. Williams, *Metal-semiconductor contacts*. Clarendon Press Oxford, 1988, pp. 89-139.

[36]   B. Sharma, *Metal-semiconductor Schottky barrier junctions and their applications*. Springer Science & Business Media, 2013.

[37]   F. Padovani and R. Stratton, "Field and thermionic-field emission in Schottky barriers," *Solid-State Electronics,* vol. 9, no. 7, pp. 695-707, 1966.

[38]   A. S. Grove, *Physics and technology of semiconductor devices*. Wiley, 1967.

[39]   S.-H. Kim, G.-S. Kim, S.-W. Kim, and H.-Y. Yu, "Effective Schottky barrier height lowering technique for InGaAs contact scheme: DMIGS and Dit reduction and interfacial dipole formation," *Applied Surface Science,* vol. 453, pp. 48-55, 2018.

[40]   D. B. Suyatin *et al.*, "Strong Schottky barrier reduction at Au-catalyst/GaAs-nanowire interfaces by electric dipole formation and Fermi-level unpinning," *Nature Communications,* vol. 5, no. 1, pp. 1-8, 2014.

[41]   N. Youngblood, C. Chen, S. J. Koester, and M. Li, "Waveguide-integrated black phosphorus photodetector with high responsivity and low dark current," *Nature Photonics,* vol. 9, no. 4, pp. 247-252, 2015.

[42] ECSTUFF4U, "Avalanche photo diode," ECSTUFF4U for Electronics Engineer,

2018. [Online]. Available: https://www.ecstuff4u.com/2018/03/avalanche-photo-

diode.html. [Accessed: Feb. 22, 2021]

Chapter 3

3.   Fabrication and characterisation technologies

3.1   Introduction

The experimental and analysis methods used throughout this thesis are introduced in this chapter. This chapter consists of three sections; firstly, the method used to deposit a thin film has been explained in section 3.2; then, the physical characterisation techniques are discussed in section 3.3, following up with the electrical and optical characterisation methods in section 3.4.

3.2   Fabrication techniques

Many optoelectronic devices have been studied in this work including; Schottky diodes, Avalanche Photodiodes and Metal-Semiconductor-Metal Photodetectors. The detailed fabrication procedures for each of these devices are provided in chapter 4 to 6. The fabrication of each type of device requires the use of the same equipment to pattern the areas and deposit metal and insulator layers. A brief description of each of these techniques is given below.

3.2.1   Thermal evaporation

As one of the physical vapour deposition process, thermal evaporation is commonly used in microfabrication process, since depositing thin films on the substrate via thermal evaporation is relatively easy to secure the electrical connection of the semiconductor devices. For the work presented in this thesis, a Moorfield minilab 60 thermal evaporator was used. As the term "Thermal" indicates, the high temperature plays an essential role in this method. Like other deposition methodologies, the thermal energy is needed to produce the vapour of the evaporates material, the difference of the thermal evaporation method is the techniques used to heat the target material. The thermal evaporation process can be described in three steps, including the formation of the vapour phase, transport of molecules from source to substrate and condense of the particles on substrate surface [1].

The source material is heated first inside the vacuum chamber and heating directly by-passing electric current through the support until the surface atoms generate sufficient energy to leave the surface.

The heated particles in a vacuum then subsequently condense onto a target substrate. In this work, the substrate material is placed under the rotation plate above the evaporation source for

upward evaporation. A shutter is used between the substrate material and evaporation source to intercept the vaporised material and prevent un-wanted particles from reaching the substrate material. The evaporation process is undertaken in a vacuum chamber, the pressure in the vacuum chamber is usually kept at or below the 10^{-6} mbar scale, to minimise the gas particles in the chamber and avoid the collision between the vapour particle and gas particles. At such low pressure, the mean free path of the particles, which is the average distance a particle can travel, is larger than the distance between the evaporation source and substrate material

As the particles are deposited on the substrate, the vapour particles finally form a nucleus. This nucleus formation is first generated islands, by constant growth until a continuous film developed [2]. The film's uniformity is achieved by rotating the substrate under a sample holder above the evaporation source.

3.2.2   Sputtering

In thermal evaporation, an energy source causes the material to vaporise, and those vaporised particles are subsequently deposited on the substrate. On the other hand, in sputtering, positive ions created by plasma are bombarded towards the source material into the chamber. It is the process of ejecting the source material by kinetic energy transfer from an ionised particle. Because sputtering is not the result of melting a material, it can be performed at a lower temperature than thermal evaporation. As a result, typically sputtering vacuum pressure is in the range of 10^{-2} to 10^{-1} torr [3].

Different methods used to achieve the sputtering of a target include direct current (DC) sputtering, radio frequency (RF) sputtering and reactive sputtering. In DC sputtering, a constant negative electric potential, serving at target material as a cathode, is used to accelerate positive ions. As such, the target material should be electrically conductive and have the ability to emit electrons (metals). However, if an insulator is used as a cathode, the negative potential cannot directly apply, and the positive ions that attracted the surface during bombardment cannot be neutralised. While in RF sputtering, the electric potential applied to the target material alternate from positive to negative at high frequency (13.56MHz), so that electrons can directly ionise the gas atom, thereby this method can be used for both conductive (metal) and non-conductive material (insulator). In reactive sputtering a gas that chemically reacts with the target material is introduced into the system, and the products of reaction create the deposited film. In this work, a Moorfield NanoPVD RF Sputter system was used to deposition insulating passivation layers.

A schematic of the RF sputtering system is shown in Figure 3. 1. The vacuum chamber is pumped to a pressure in the scale of 10^{-7} torr to remove water and other gas molecules, followed by filling it with argon gas and applying high-frequency power supply at the target material. A larger electric field is formed on the target, once the striking voltage is achieved, the gas ionisation becomes self-sustaining, and a glow discharge (plasma) is created. During the negative cycle of sputtering, positively charged Ar^+ ions were attracted the target, which acts as a cathode. While the positive ions are bombarding on the target's surface, the charge build-up on the target leads to a complete secession of atoms being discharged for coating. By alternating the electrical potential, the charge build-up on the target surface can be neutralised via attracting some electron from plasma while the target becomes the anode during the positive cycle of sputtering [4].
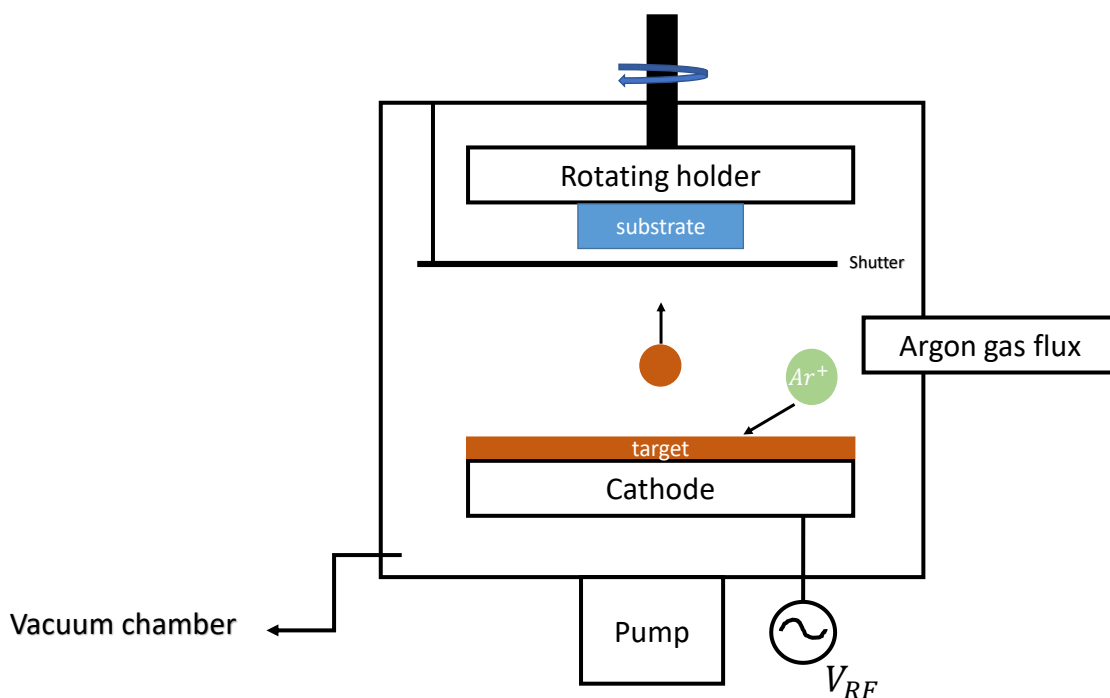
Figure 3. 1 Schematic diagram of the RF sputtering system

3.2.3   Photolithography

Since the beginning of the microelectronics industry, the photolithography process is the primary technique for fabrication of intergraded circuits. The principle of these techniques is

to transfer the pre-designed image of patterns on a mask onto a semiconductor wafer coated with photo sensitively material, so-called photoresist. The diagram of an optical projection lithography tool is shown in Figure 3. 2. It can be seen that the lithography tool consists of a light source, a mask containing the drawing of the circuit to be made and an optical system designed for projecting the reduced image of that mask onto the photoresist coated on the semiconductor surface. During the exposure, the photoresist is chemically altered in the area where the UV light exposure occurs. It then undergoes a baking process that makes the exposed area sensitive or insensitive to the development step [5]. In the case of positive photoresist, the exposed part is dissolved, while for those negative photoresists, the non-exposed area is soluble in the developer solution. Therefore, the resist is structuring the patterns presented on the mask, which will define the device's further process. The patterns defined can then be transferred to the semiconductor material during lift-off or an etch process step. As for the lift-off process, the photoresist remains after the development step is used as a shadow mask, while for the etch process step, the photoresist remains used as an etch mask, the areas protected by the resist will not be etched. All the steps are presented in Figure 3. 3.
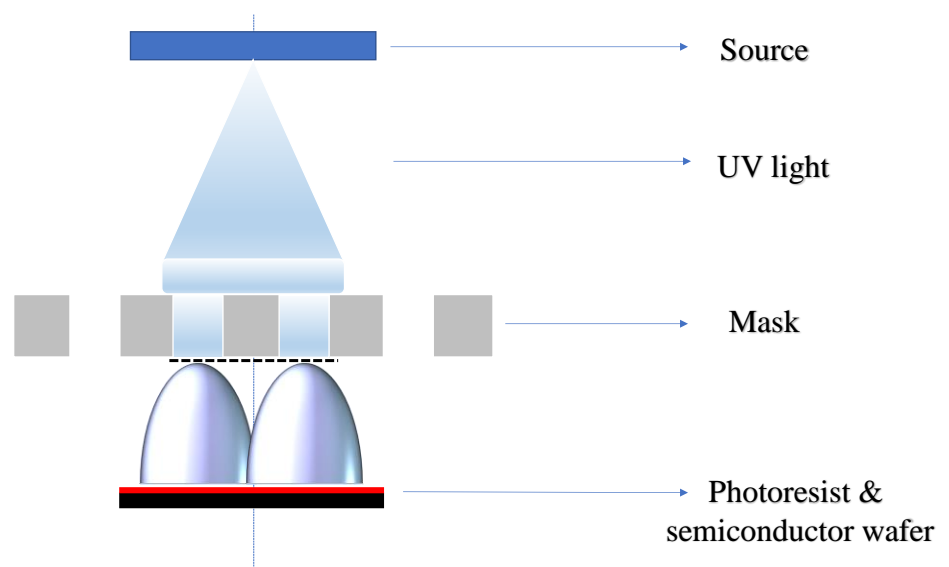
Figure 3. 2 Schematic diagram of aligner
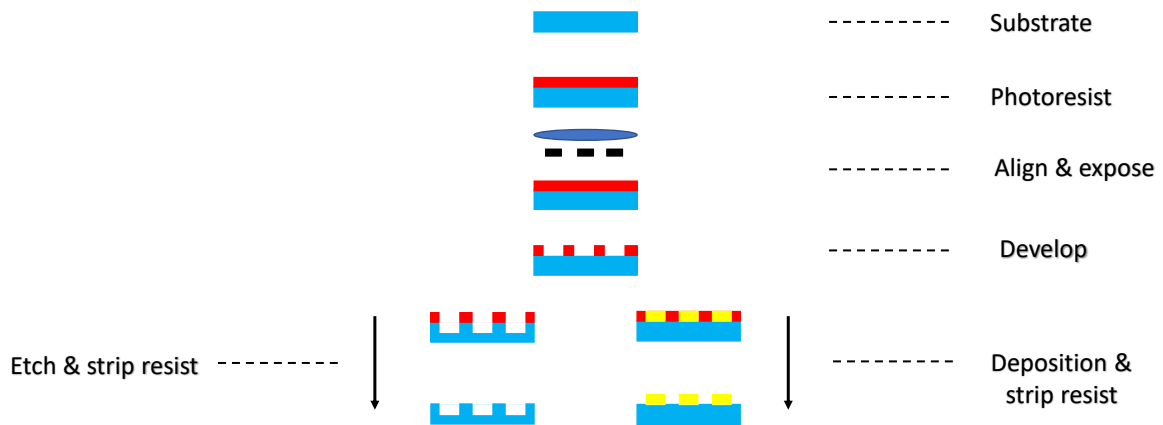
Figure 3. 3 Process diagram of photolithography

3.3   Physical characterisation

3.3.1   x-ray diffraction

X-ray diffraction is a measurement technique widely used in materials characterisation to obtain information on the atomic scale structure of various materials in a variety of states [6]. The object of X-ray diffraction is that the incident X-rays are completely in phase and reinforce each other to produce a detectable diffraction beam. If the incident X-rays strike the crystal where all atoms are placed in a regular periodic array, the diffraction beam with sufficient intensity can be detected when the condition satisfies Bragg's law [7],

$$n\lambda = 2d' \, sin(\theta) \tag{3-1}$$

where *n* is the order of reflection, λ is the wavelength, *d'* is the interplanar spacing and θ is the Bragg angle. The diffraction of X-rays from a set of lattice planes has shown in Figure 3. 4. The geometric relation of the plane normal, incident and diffracted X-ray beams are always coplanar. Furthermore, the angle between the diffracted X-ray beam and transmitted is always 2θ, this angle called diffraction angle [6]. The diffraction angle 2θ can be calculated by Bragg's

law and the plane spacing equation. For example, if the crystal is cubic, the plane spacing equation can by described as [6],

$$\frac{1}{d} = \frac{(h^2+k^2+l^2)}{a^2}$$

(3- 2)

where d is the interplanar spacing, a is the lattice parameter and $(h\ k\ l)$ is the Miller indices. By combing with Eq. (3- 3), the diffraction angle can be obtained from the following equation [6].

$$sin^2(\theta) = \frac{\lambda^2(h^2+k^2+l^2)}{4a^2}$$

(3- 3)

The average particle size can also be estimated by using the Scherrer equation [8],

$$L = \frac{K\lambda}{(B\ cos\ \theta)}$$

(3- 4)

where L is the linear dimension of a particle, K is Scherrer constant, λ is the incident X-ray wavelength, B is the half-value breadth of each XRD peak, and θ is the Bragg angle.
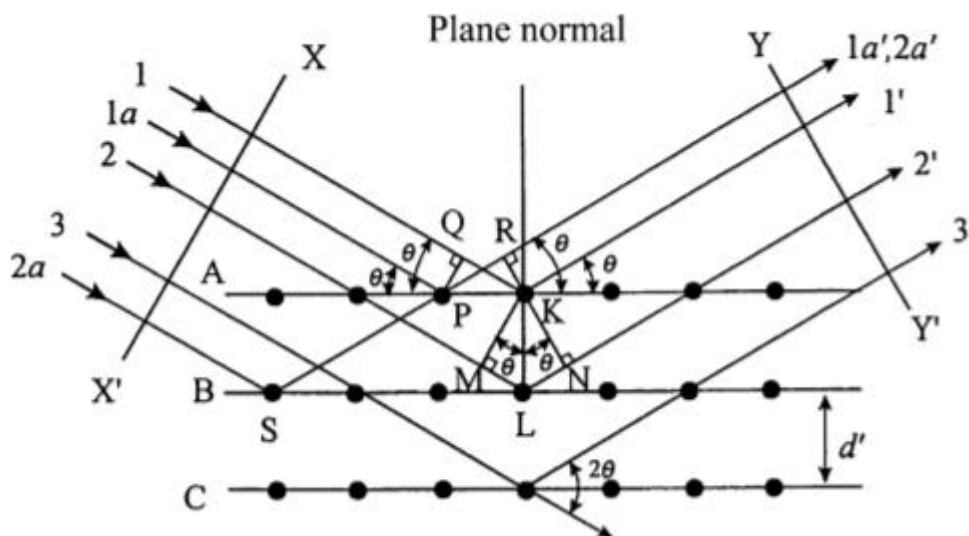
Figure 3. 4 Schematic diagram of x-ray interaction in XRD measurement [6]

3.3.2 Scanning Electron Microscopy

The electron microscope is a useful tool to investigate the structure of microelectronic devices in the nano-scales. Unlike conventional light microscope, an electron microscope uses electron beams to produce a magnified image of the sample [9], which provides much larger magnifications and much higher depth. The electron beam is usually generated by a heated cathode or a field emission gun. Then, an acceleration voltage is applied to provide sufficient kinetic energy with the electrons. When the electron beam hits on the sample, different types of physical process are generated. If the samples are thin enough, part of the electron with sufficient energy will be transmitted, either with or without scattering. The scattering process can be either elastic (without energy losses) or inelastic (with energy losses). Because of the large difference in mass between the electron and the atomic cores, minimal momentum is transferred from the incident electron to the atomic nucleus, which leads to an elastic scattering process. The incident electron can also lead to secondary electron emission by ionising atoms in the sample. After the ionisation process, other processes such as X-rays emission, filling the vacancy electron shell or emitting Auger electrons can all be possible; this would lead to a consequence with a loss of energy. As for the incident, electrons interact with the atoms' electron shells, both elastic and inelastic scattering process occur [10].

Scanning electron microscope (SEM) and transmission electron microscope (TEM) are the most common used electron microscope to investigate the semiconductor application. The SEM image is acquired by scanning the sample with a focused electron beam and detecting the secondary and backscattered electrons. In contrast, the image in TEM is obtained by the electron transmitted through the thin samples.

The SEM is also one of the powerful instruments capable of examining the microstructure morphology and chemical composition characterisations [11]. An SEM consists of an electron gun, lens system, scanning coils, aperture system, an electron detector and a cathode ray display tube (CRT). A schematic of the scanning electron microscope has shown in Figure 3. 5. The electrons were generated from an electron gun and pass through a group of lenses to form an electron beam. With the help of the aperture system, the electron beam focus and scan across the sample. The physical process is generated while the incident electron beam is scanning the samples. The detector collects secondary electrons; the density of collected electrons is amplified and displayed on the CRT.
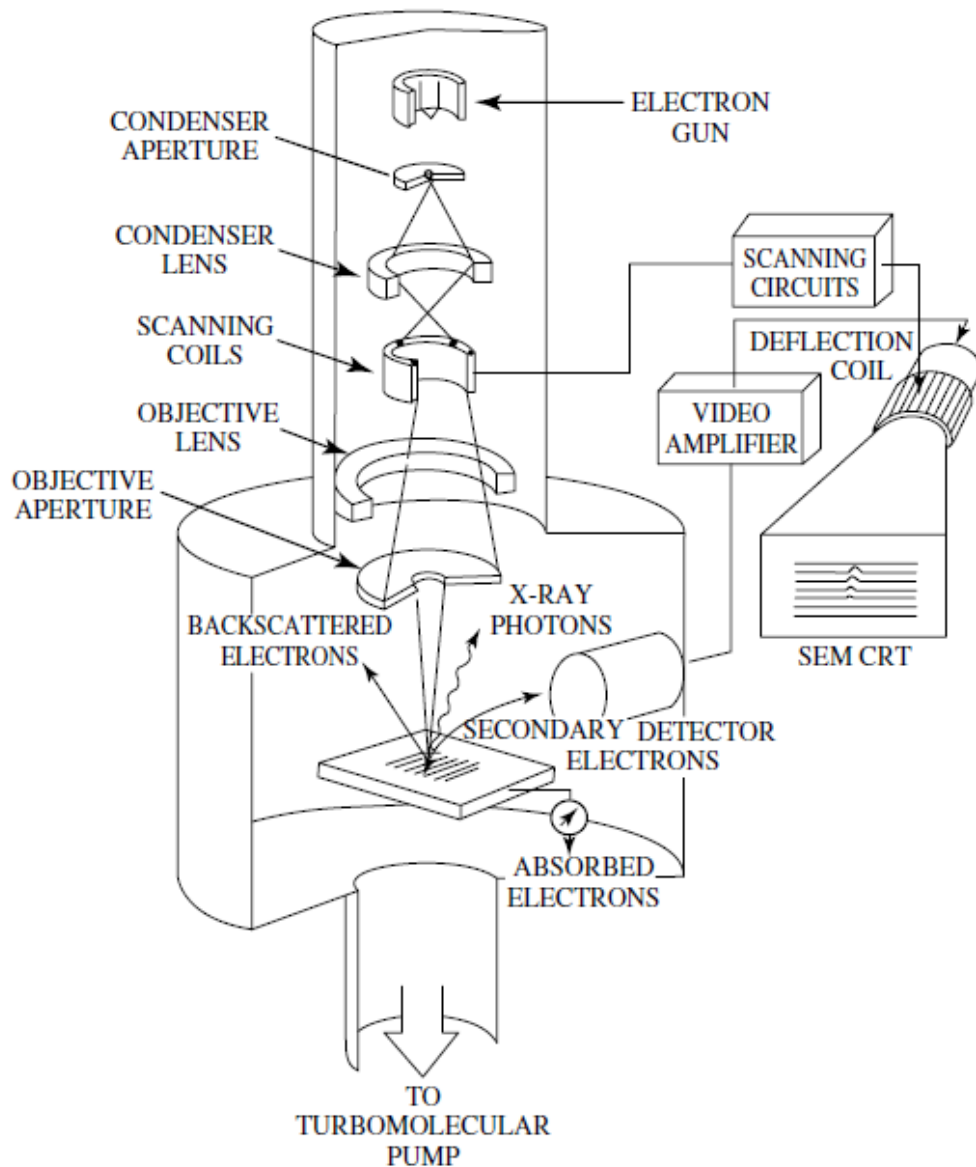
Figure 3. 5 Schematic diagram of a scanning electron microscope [12]

3.3.3 Transmission Electron Microscopy

The transmission electron microscopy (TEM) was widely used for highly magnified sample images. The main advantages of TEM lines in its extremely high resolution generally can reach 0.01nm. The shortcoming of TEM is its limited depth resolution, which makes the specimen used for TEM measurement must prepare extremely thin enough. A schematic diagram of the transmission electron microscope is shown in Figure 3. 6.   It consists of an electron gun, a condenser system, an objective system and a projector system. During the process, the electron generated from the electron gun is accelerated to high voltage, typically from 100 to 400 kV. Then the electron beam is focused on the sample by the condenser lenses. Since the nature of

transmission that the electron beam needs to travel through the specimen, the sample must be thin enough to be transparent to the electrons. With the help of an additional lens, the image is projected onto the screen for viewing. The three primary image modes of TEM are bright-field, dark-field and high-resolution microscopy [9]. The pictures obtained via TEM have a critical role in semiconductor material analysis, in particular, cross-sectional images through semiconductor devices have brought many aspects of the material's physical properties.
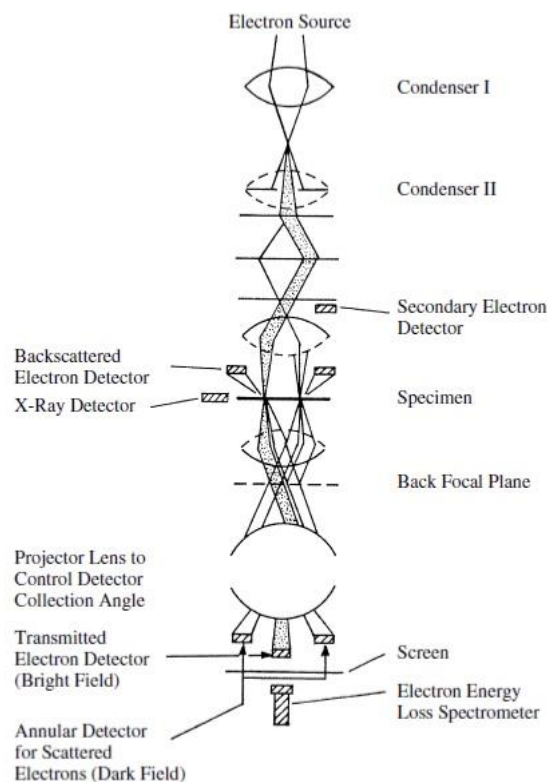
Figure 3. 6 Schematic diagram of a transmission electron microscope [9]

3.4   Electrical and optical characterisation

3.4.1   Current-voltage characteristics

Current-voltage (IV) measurements were performed with an Agilent Technology B1500A semiconductor device analyser connected to a screened probe station. The voltage sweeps were taken from zero to positive voltages and zero to negative voltages to investigate devices' behaviour. Semi-log plotting of IV was obtained to fit with the thermionic emission (TE) dominated conducting mechanism of the Schottky junction. The ideality factor, saturation current, series resistance and the effective barrier height can be determined by TE current-voltage expression [13, 14]

$$I = I_s \left\{ exp \left[\frac{q(V-IR_S)}{\eta kT} \right] - 1 \right\}$$

<div align="right">(3- 5)</div>

I_s is the saturation current defined by

$$I_S = AA^{**}T^2 exp[-q\varphi_b/kT]$$

<div align="right">(3- 6)</div>

where q is the electronic charge, V is the applied voltage,R_s is the series resistance, η is the ideality factor, k is the Boltzmann constant, T is the absolute temperature, A is the diode contact area, A^{**} is the effective Richardson constant and φ_b is the effective barrier height.

The current-voltage characteristics of a typical Si diode has shown in Figure 3. 7. An example of different conducting process on both forward and reverse bias in the PN junction has been compared with the ideal diode characteristics. Several aspects affect the current-voltage characteristics from the ideal situation has been listed in Figure 3. 7. At the forward bias, both diffusion current and recombination current are taken into consideration. When the ideality factor equals to 2, the recombination current dominates and when the ideality factor equals to 1, the diffusion current dominates. When both currents are comparable, the ideality factor value between 1 and 2. Another aspect is the high-injection condition. When the injected minority carrier density is comparable to the majority concentration, both drift and diffusion components are considered. Under the condition of high-injection current, the effect associate with serial resistance will be considered. This resistance absorbs part of the applied voltage between the diode terminals [15]. At the reverse bias, the total reverse current is the sum of diffusion current in the neutral region and the generation current in the depletion region. When sufficient high electric field applied on the PN junction, the junction breaks down occurs. The three main breakdown mechanism include thermal instability, tunnelling and avalanche multiplication [15].
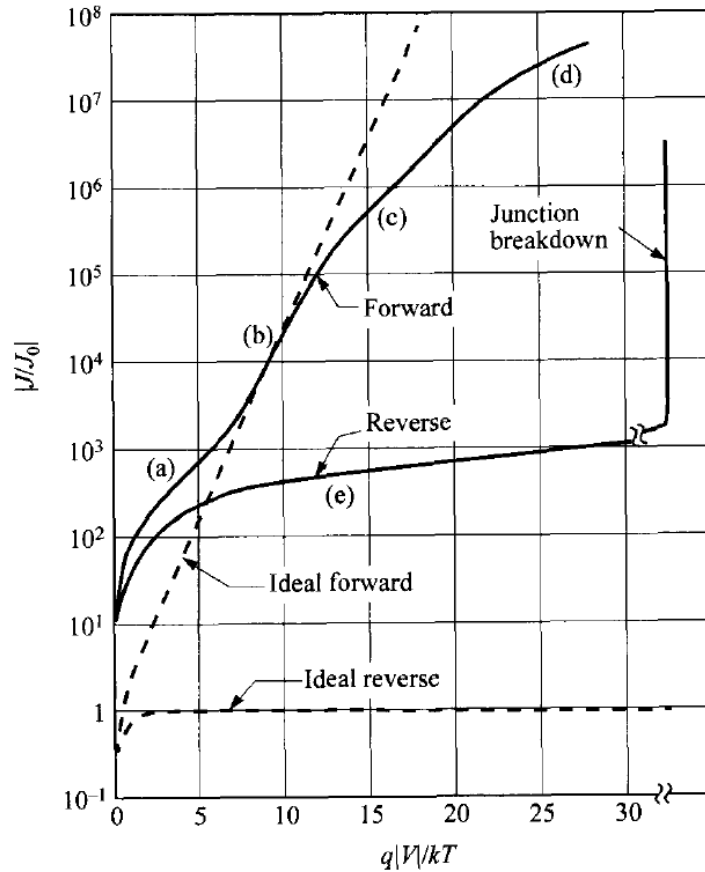
Figure 3. 7 I-V characteristics of a practical Si diode. (a) Generation-recombination current region. (b) Diffusion-current region. (c) High-injection region. (d) Series-resistance effect. (e) Reverse leakage current due to generation-recombination and surface effects [15].

3.4.2 Transmission line method

The transmission line method (TLM) is a commonly used measurement technique considering both the semiconductor sheet resistance and contact resistance [16]. A schematic diagram of a TLM measurement structure is shown in Figure 3. 8. (a). An array of rectangular metal contacts with different spacing are formed over the semiconductor region. Resistance measurements between each pair of contact can be used to construct the TLM plot. The measured total resistance can be expressed as

$$R_T = 2R_m + 2R_C + R_S \qquad (3\text{-}7)$$

where R_T is the measured total resistance, R_m is the resistance of metal contact, R_C is the contact resistance, and R_S is the semiconductor resistance.

The semiconductor resistance can be represented as

$$R_S = R_{sh}\frac{L}{W}$$ (3- 8)

where R_{sh} is the sheet resistance, L is the length of the metal contact, and W is the width of the metal contact. In most cases, the resistivity of the metal contact is extremely low that R_C >> R_m. Therefore, the resistance of metal contact can be ignored.

Substituting for R_S in Eq. (3-9) leads to

$$R_T = 2R_C + R_{sh}\frac{L}{W}$$ (3- 9)

The total resistances are measured for different contact spacing, and the total resistance is plotted as a function of spacing, as illustrated in Figure 3. 8. (b). Two parameters can be extracted from the figure. The slope leads to the sheet resistance and the intercept giving the contact resistance of the metal-semiconductor contact.
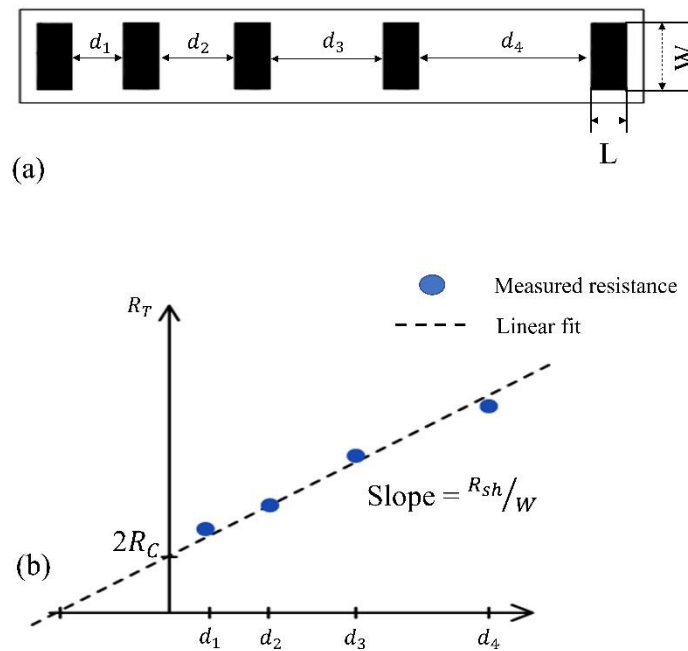
Figure 3. 8. (a) schematic diagram of TLM measurement structure and (b) plot of total resistance against resistor length

3.4.3 Photocurrent and Spectral Response

Phase-sensitive detection is a useful method for observing small signals in the presence of overwhelming noise. The lock-in amplifier, first developed in the 1960s [17], is the instrument which makes this method possible. The lock-in amplifier is used to reduce the error by modulating the input signal by a reference signal such as optical chopper, and upon signal detection, measuring only the voltage input modulated by the reference signal. The

monochromator provides a narrow band of wavelength light, divided from a wide range of wavelength light source.

Figure 3. 9 shows the experimental set-up of the lock-in amplifier system with a monochromator. A HORIBA iHR320 monochromator shown in Figure 3. 10 is used to divide the spectrum from a lamp source (wide range of wavelengths) into a selectable narrow band of light or other wavelengths radiation. The fabricated photodiodes were first mounted onto a custom PCB and wire-bonded by hand to enable electrical contact. The resultant PCB was then secured onto an appropriate translation stage at the exit port of the monochromator. Both monochromator and the photodiode were attached securely on the aluminium breadboards, allowing sufficient room for accessories such as lens, optical chopper and filter can be placed in between. The light beam was centred on the photodiode, and the optical chopper was placed between the monochromator and photodiode so that blades could obstruct the beam. The optical chopper was attached to the lock-in amplifier to provide the reference frequency. The photodiode output was connected to a flexible pre-amplifier, and the output of the amplifier was connected to the input of the lock-in amplifier. A focus lens was placed in the path of the beam, which used to focus the beam. During the measurement, a typical time constant of $3s$ was used. The typical frequency of the optical chopper is at 330 kHz.
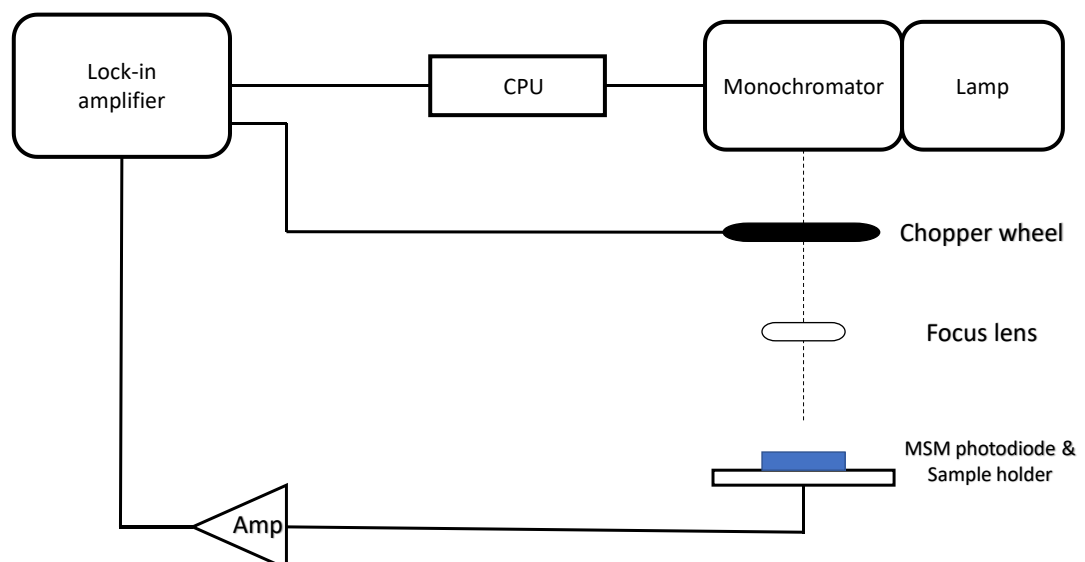
Figure 3. 9 Schematic of the experimental set-up to measure optical respond
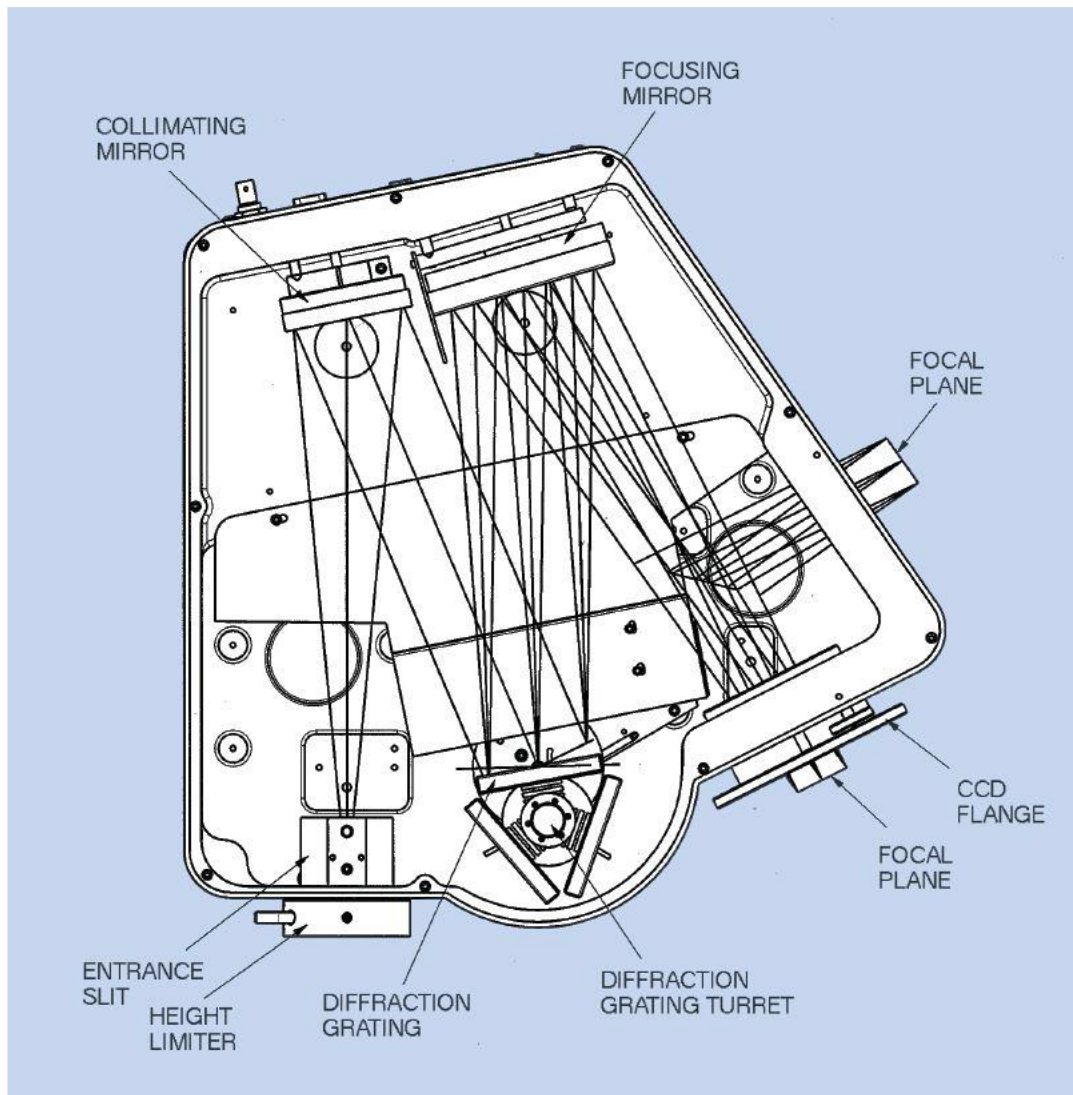
Figure 3. 10 Schematic diagrams of the HORIBA iHR320 monochromator Scientific [18]

3.5   Reference

[1]   R. F. Bunshah, *Handbook of deposition technologies for films and coatings: science, technology, and applications*. William Andrew, 1994.

[2]   H. Frey and H. R. Khan, *Handbook of thin film technology*. Springer, 2015.

[3]   T. M. A. R. A. Layton, "Introductory MEMS: Fabrication And Applications."

[4]   P. Davidse, "Theory and practice of RF sputtering," *Vacuum,* vol. 17, no. 3, pp. 139-145, 1967.

[5]   S. Landis, *Lithography*. John Wiley & Sons, 2013.

[6]   Y. Waseda, E. Matsubara, and K. Shinoda, *X-ray diffraction crystallography: introduction, examples and solved problems*. Springer Science & Business Media, 2011.

[7]   M. Kakudo and N. Kasai, *X-ray Diffraction by Macromolecules*. Kodansha Limited and Springer-Verlag Berlin Heidelberg, 2005.

[8]   A. Patterson, "The Scherrer formula for X-ray particle size determination," *Physical review,* vol. 56, no. 10, p. 978, 1939.

[9]   D. K. Schroder, *Semiconductor material and device characterisation*. John Wiley & Sons, 2015.

[10]   H. Borchert, *Solar cells based on colloidal nanocrystals*. Springer, 2014.

[11]   W. Zhou, R. Apkarian, Z. L. Wang, and D. Joy, "Fundamentals of scanning electron microscopy (SEM)," in *Scanning microscopy for nanotechnology*: Springer, 2006, pp. 1-40.

[12]   R. A. Young and R. V. Kalin, "Scanning Electron Microscopic Techniques for Characterization of Semiconductor Materials," ACS Publications, 1986.

[13]   S. M. Sze and K. K. Ng, *Physics of semiconductor devices*. John wiley & sons, 2006.

[14]   E. H. Rhoderick, "Metal-semiconductor contacts," *IEE Proceedings I-Solid-State and Electron Devices,* vol. 129, no. 1, p. 1, 1982.

[15]   S. M. Sze and K. K. Ng, *Physics of semiconductor devices*. John wiley & sons, 2006, pp. 134-187.

[16]   G. Reeves and H. Harrison, "Obtaining the specific contact resistance from transmission line model measurements," *IEEE Electron device letters,* vol. 3, no. 5, pp. 111-113, 1982.

[17]   G. B. Armen, "Phase sensitive detection: the lock-in amplifier," *Knoxville, University of Tennessee,* 2008.

[18] H. Scientific. "iHR Series Brochure", 2013. [Online]. Available: https://static.horiba.com/fileadmin/Horiba/Products/Scientific/Optical_Components_and_OEM/iHR_Series/iHR_Series_Brochure.pdf. [Accessed Jan. 02, 2021].

Chapter 4

4. Influence of annealing on GaSb based Schottky diodes

4.1 Introduction

GaSb is a III-V compound semiconductor material with the bandgap of 0.72eV. It is typically used in optoelectronic devices working in the near-infrared, such as gas and chemical sensing. [1-3] Introducing small amounts of Bi into GaSb can significantly reduce the bandgap and thus potentially extend the emission wavelength from 1.7 μm for GaSb to beyond 3 μm, opening up a window for extended applications in biological and chemical sensing. While the reduction in the bandgap is primarily due to a downward shift in the conduction band, there is also a concomitant raising of the valence band. [4-8] However, successful incorporation of Bi into the GaSb matrix requires nonstandard growth conditions such as very low growth temperatures, potentially reducing the quality of the material. As such, obtaining high Bi incorporation while still retaining a high crystal quality remains a challenge that has not been fully addressed and optimized.

Despite significant work over recent years focused on introducing Bi into GaAs, [9-11] there has been limited attention paid to GaSb-based alloys. GaAsBi alloys also require a nonstandard growth parameter space and as such a number of refinements and advances to the growth and subsequent fabrication have had to be realised to enable functioning laser diodes to be obtained. For instance, Feng et al. [12] have investigated the influence of annealing on the optical properties of $GaAs_{0.968}Bi_{0.032}$ by photoluminescence intensity and HR-XRD measurements which were performed to characterize the structural changes during annealing, this showed that the PL peak intensities remain stable for annealing temperatures of up to 700 °C and then severely deteriorate at 800 °C.

Comparatively, there are a few articles reported on Bi incorporation in GaSb, [8, 13-18] especially the electrical properties of GaSbBi. Rajpalke et al. [18] have realized $GaSb_{1-x}Bi_x$ material by molecular beam epitaxy (MBE) with 9.6% Bi incorporation, with droplet-free smooth surfaces and high crystalline quality, resulting in a bandgap of 410 meV. More recently, even higher Bi contents in the range of 11–14.5% have been demonstrated by Delorme et al., [13] Yue et al., [19] and Hilska et al. [20] To try and achieve better electrical performance, Dier et al.[21] and Rotelli et al. [22] have investigated various passivation processes to reduce oxide layers on the surface of GaSb. Recently, a GaSbBi-based laser diode has been demonstrated; [23], however the performance was limited by a high level of defects and leakage current mechanisms which were attributed to the introduction of Bi to the GaSb matrix.

As such, while lasing devices have been demonstrated, there is still significant work needed to optimize and improve the material quality to realize efficient laser sources for device applications. The physical and electrical characteristics of annealed GaSbBi are presented and discussed.

4.2   Experimental detail

The following GaSbBi films were grown by the Department of Physics at University of Warwick. A series of thin GaSbBi films were grown using a Mod Gen II using a cracker cell to provide the Sb flux and Vecco Sumo cells to provide the Bi and Ga fluxes, it is assumed that the Sb fluxes comprise Sb_2 for the valve temperature of 800 °C. The samples consisted of 400 nm thick nominally undoped GaSbBi layers grown on 100 nm thick GaSb buffer layers grown directly onto the substrate. Samples with Bi concentrations of 3.5% and 4% were grown at a temperature of 325 and 250 °C, respectively, with growth rates of 0.75 μm/h and 0.5 μm/h.

The Bi content of the GaSbBi films was determined using x-ray diffraction (XRD) using the fact that the previous work from Stephenson Institute for Renewable Energy group at University of Liverpool, who have quantified the dependence of lattice parameter on Bi content by combining XRD and Rutherford backscattering. [18] The XRD measurements in this chapter used a Rigaku Smartlab x-ray diffractometer, with a rotating copper anode and a Ge (220) four bounce monochromator, under ambient conditions. The Cu $K\alpha_1$ line was used with a wavelength of 1.5406 Å. The 004 Bragg reflections were measured. A series of reference GaSb samples was grown, where a nominally undoped 400 nm layer of GaSb was grown at temperatures of 250, 300, 325, and 400 °C.

Epitaxial wafers were initially cleaved and then cleaned with acetone and isopropyl alcohol for 10 min each. The samples were annealed with different temperatures and time, under a nitrogen rich background in an annealing furnace. The samples were sandwiched between two dummy GaSb wafers and placed in a sealed ampoule during the annealing process to prevent out diffusion of Sb. The Ohmic contact of the backside was made by evaporating Au-Zn-Au, before patterning of the top contact via photolithography. The top Schottky contact consisted of Ti-Au and was deposited via thermal evaporation. Electrical, current-voltage (I-V) measurements were performed with an Agilent Technology B1500A Semiconductor Device Analyser. The Schottky diode structure used in this chapter is shown below in Figure 4. 1.
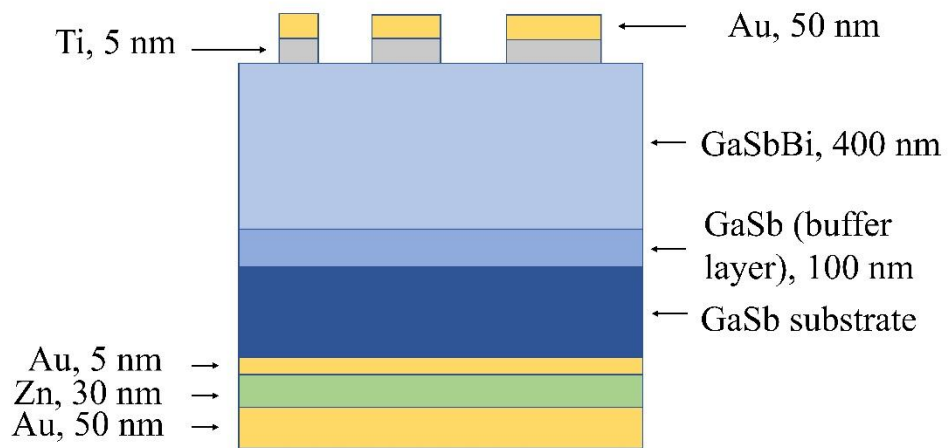
(a)
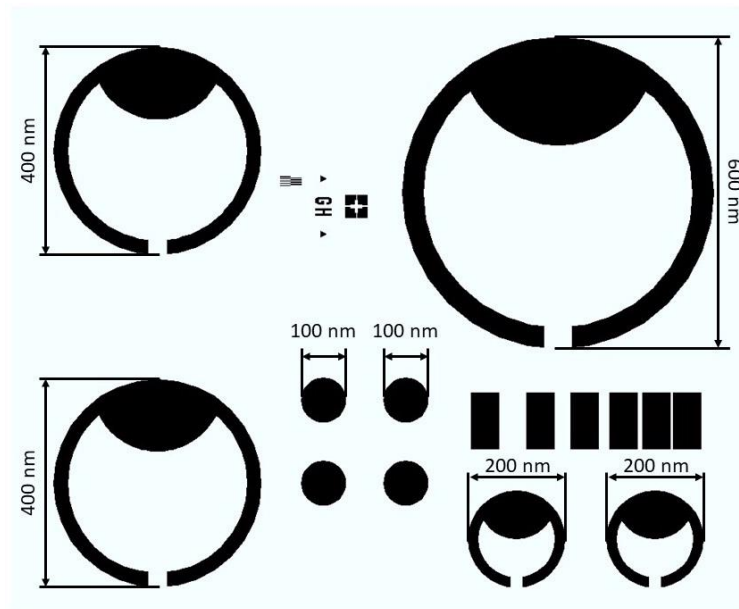
(b)

Figure 4. 1 Schematic of (a) cross section and (b) top view of Au/GaSbBi Schottky diode

To investigate this more closely, the transmission electron microscopy (TEM) was performed at the Imaging Centre at University of Liverpool to look for changes in the material as the anneal temperature is increased. For transmission electron microscopy (TEM) measurements, electron transparent thin lamella specimens were prepared from wafer sections, using the focused ion beam (FIB) lift-out method, [24] using a dual beam FEI Helios 600i FIB instrument. Trenching and thinning were performed using a 30 kV Ga ion beam before damaged surface layers were removed with a 5 kV beam. Bright field (BF) and high angle annular dark field (HAADF) images were recorded using a probe side aberration corrected JEOL 2100FCs

scanning transmission electron microscope (STEM) operating at 200 keV. HAADF z-contrast images were formed using electrons collected over a semiangle range from 70 to 190 mrad. Energy dispersive x-ray (EDX) spectroscopy was performed, in the TEM, using an EDAX windowless x-ray detector.

4.3   Annealing effects on GaSb Schottky diode

As GaSbBi films have to be grown at low temperatures in order to incorporate Bi, [8, 13, 18] I initially measured a series of Schottky diodes fabricated from GaSb thin films grown at different temperatures (ranging from 250 °C to 400 °C), to study the influence of growth temperature on device performance. This series of samples was grown on p-type GaSb substrates and consisted of 400 nm thick nominally undoped GaSb layers. The I-V characteristics of the resultant diodes are shown in Figure 4. 2. As the growth temperature decreases, there is a significant decrease in the diode rectification, with nondiode like I-Vs being observed at growth temperatures below 400 °C. Similar results have been obtained previously [25] and were attributed to the low surface mobility of elemental antimony at these growth temperatures, resulting in Sb having an increased probability of being incorporated at antisites.

The postgrowth annealing process on all the samples grown at low temperatures (lower than 400 °C) were performed and to see if improved electrical performance could be obtained. All the as-grown samples were annealed at 400 °C for 20 min. The I-V characteristic for the annealed diode have shown different level improvement on the electrical properties, with the diode grown at 325 ºC demonstrated the most significant improvement on the electrical performance, as shown in Figure 4. 2 (dashed line). This confirms that the electrical properties of low growth temperature GaSb can be dramatically improved by a subsequent annealing process. The results shown indicate that the annealed low growth temperature sample actually has better diode characteristics than the corresponding high growth temperature sample. Similar annealing results have been reported previously on different materials, such as GaN [26] and more recently GaAsBi. [12]
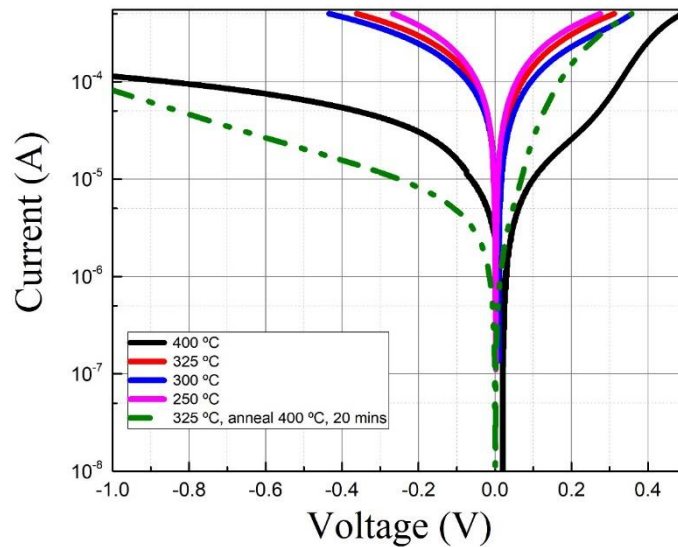
Figure 4. 2. I-V characteristic of Au/GaSb Schottky diodes for different GaSb growth temperatures and also after postgrowth annealing.

4.4   X-ray diffraction measurement on annealed GaSbBi samples

The annealing process was then repeated to see if similar annealing could improve the performance of GaSbBi devices grown; for initial measurements, the sample with a Bi composition of 3.5% (corresponding to a growth temperature of 325 °C) were utilized. Samples were annealed at temperature of between 400 and 500 °C for duration between 5 and 30 min. To initially verify that the annealing process has not altered the Bi concentration, x-ray diffraction (XRD) measurements were performed on each of the GaSbBi samples.

The XRD patterns of the GaSbBi for the as-grown reference layer and layers annealed at 400 and 500 °C for 30 min are shown in Figure 4. 3 (symbols), along with corresponding simulations (line). It can be seen that the peak corresponding to the GaSbBi film is at a lower angle than the substrate GaSb. This corresponds to the expansion of the lattice of the GaSbBi epilayers with respect to the substrate. [7] Good simulation were obtained for each of the samples using the film thickness and Bi content parameters given in Table 4. 1. It is clear from the XRD that the main epilayer peak does not shift significantly during the annealing process, and the simulation result indicates that the bismuth incorporation is unaffected by the annealing procedures. Within the accuracy of the modelling of XRD data, the film thickness is constant for all annealing treatments apart from 500 °C for 30 min. For that one annealing treatment, the deduced change may be a real change of the GaSbBi layer thickness due to out-diffusion

of Bi, but the apparent change in film thickness may instead be a manifestation in the XRD modelling; and this result will be revisited at the end of the chapter.

Annealing temperature (°C)	Annealing time (min)	Film thickness (nm) ± 10 nm	Bi content (% of anion sublattice) ± 0. 01
As-grown	As-grown	308	3.45
400	30	290	3.45
500	5	290	3.15
500	15	290	3-70
500	30	245	3.70

Table 4. 1 The parameters used to model the XRD patterns after different annealing temperatures.
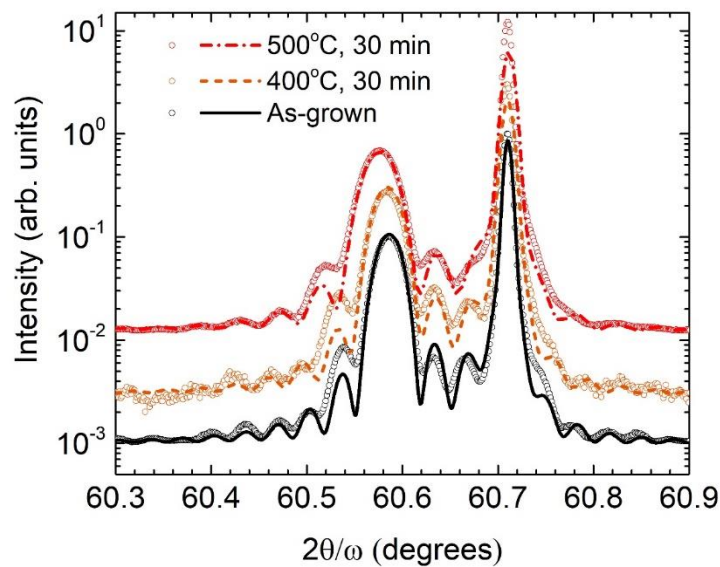
Figure 4. 3. XRD patterns of the 004 reflections of GaSbBi films containing 3.5% Bi with different annealing temperatures. The experimental data are shown as open circles and the simulations are shown as lines.

4.5   Electrical characteristics of annealed GaSbBi Schottky diode

To investigate potential improvements in the electrical performance, the same samples were fabricated into Schottky diodes, and room temperature I-V measurements were performed, with the results shown in Figure 4. 4. It can be seen that the diode characteristics are improved upon annealing, with lower dark currents being observed as a function of both increasing annealing temperature and time, resulting in the device annealed at 500 °C for 30 min showing good diodelike behaviour. We have fitted the experimental data with the diode equation to enable us to extract the ideality factor and saturation current for the diodes as a function of annealing the condition. Figure 4. 5. (a) gives the values obtained for devices annealed for 15 min, while Figure 4. 5. (b) gives the values for those annealed for 30 min. for the samples annealed for 15 min,

the values of saturation current decreased from 2.64×10^{-4} A (as-grown) to 1.68×10^{-5} A (at 500 °C), and the ideality factor decreased from 2.57 (as-grown) to 1.62 (at 500 °C). A similar trend can be observed in Figure 4. 5. (b) for devices annealed for 30 min with the saturation current and the ideality factor decreased to 3.72×10^{-5} A and 1.3, respectively, after annealing at a temperature of 500 °C. The extracted values of the ideality factor are relatively high, particularly for the as-grown sample. This suggests that the dominant recombination process in these diodes is not thermionic emission, [27, 28] but rather other current processes are actively contributing to the diode performance. These additional current paths could come from a range of potential sources including, but not limited to, surface roughness, [29] tunnelling due to high background doping, [17] impurities, or the presence of native oxide layers. [30] The improvement in the I-V curves observed in Figure 4. 4 suggests that dislocations or point defects, which are subsequently repaired upon annealing, [31, 32] may well be contributing to these additional current paths. The key result obtained here that postgrowth annealing can significantly improve the diode performance and it's extracted ideality factor. To fully analysis the conduction mechanism of the Schottky diode, an extra temperature dependence measurement with different size of the device could be investigated. However, due to the limit source of the material, this topic of conducting mechanism of annealed GaSbBi Schottky diode has not been investigated throughout this thesis. These results also indicate longer annealing times, at least up to 30 min results in an improved electrical performance compared to shorter times. Of course, the optimum annealing conditions will be determined by the thermal does induced in the sample, which will be a function of temperature and time. These results show that postgrowth annealing can result in dramatically improved electrical performance of GaSbBi alloys.
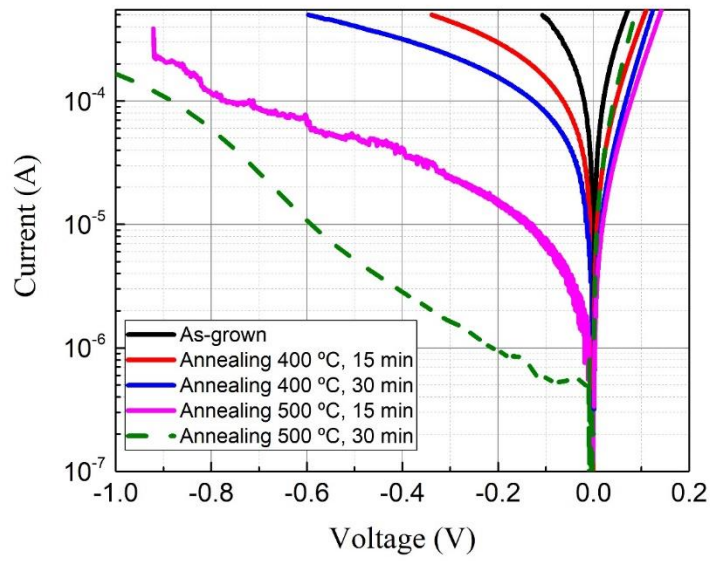
Figure 4. 4. I-V characteristics of Au/GaSbBi containing 3.5% Bi Schottky diode after different annealing conditions.
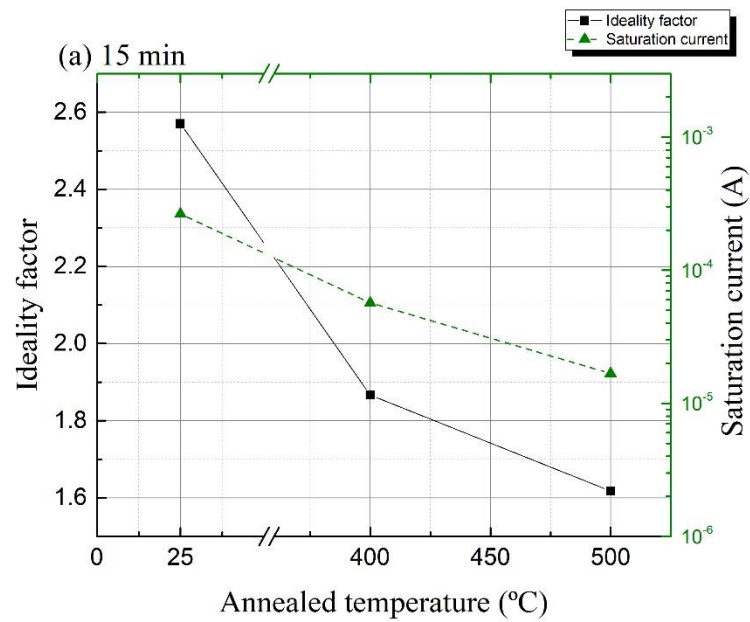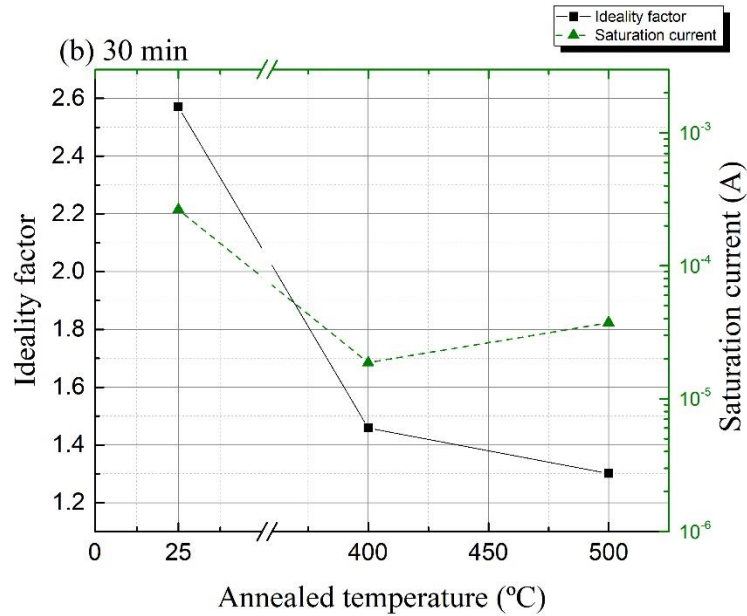
Figure 4. 5. Temperature dependent ideality factor and semi-log plot saturation current of Au/GaSbBi containing 3.5% Bi Schottky diode under different annealing conditions: (a) 15 min and (b) 30 min.

To investigate the repeatability of this result as well as the influence of higher annealing temperatures, an additional group of samples with Bi composition of 4% was also annealed and the measurement were repeated. The resultant I-V characteristics of Schottky diodes are presented in Figure 4. 6. As before, a clear improvement is observed in the diode characteristics as the annealing temperature increased to 500 °C. However, when the annealing temperature increase further to 550 °C, a resultant deterioration in the electrical performance is noted. From fitting the experimental data, similar reductions in the ideality factor and saturation current [presented in Figure 4. 6. (b)] are interesting to note that electrical properties initially degrade (higher saturation current and ideality factors) as the sample is annealed up to a temperature of 450 °C, which is in contrast to the results noted in the previous sample. The most likely explanation for this is nonuniformity across the wafer, potentially leading to a higher number of defects in the sample annealed at 450 °C. This seems particularly likely as this piece of the wafer originated much closer to the wafer edge than the other pieces what were annealed.

While this result confirms the previous result and indicates that annealing can help improve the electrical performance, it also suggests that a secondary process is also occurring during the annealing process. Initially, upon annealing, the material quality is improved, leading to improved electrical performance. However, as the temperature is increased, a second change in the material occurs, which has a detrimental effect on the electrical performance.
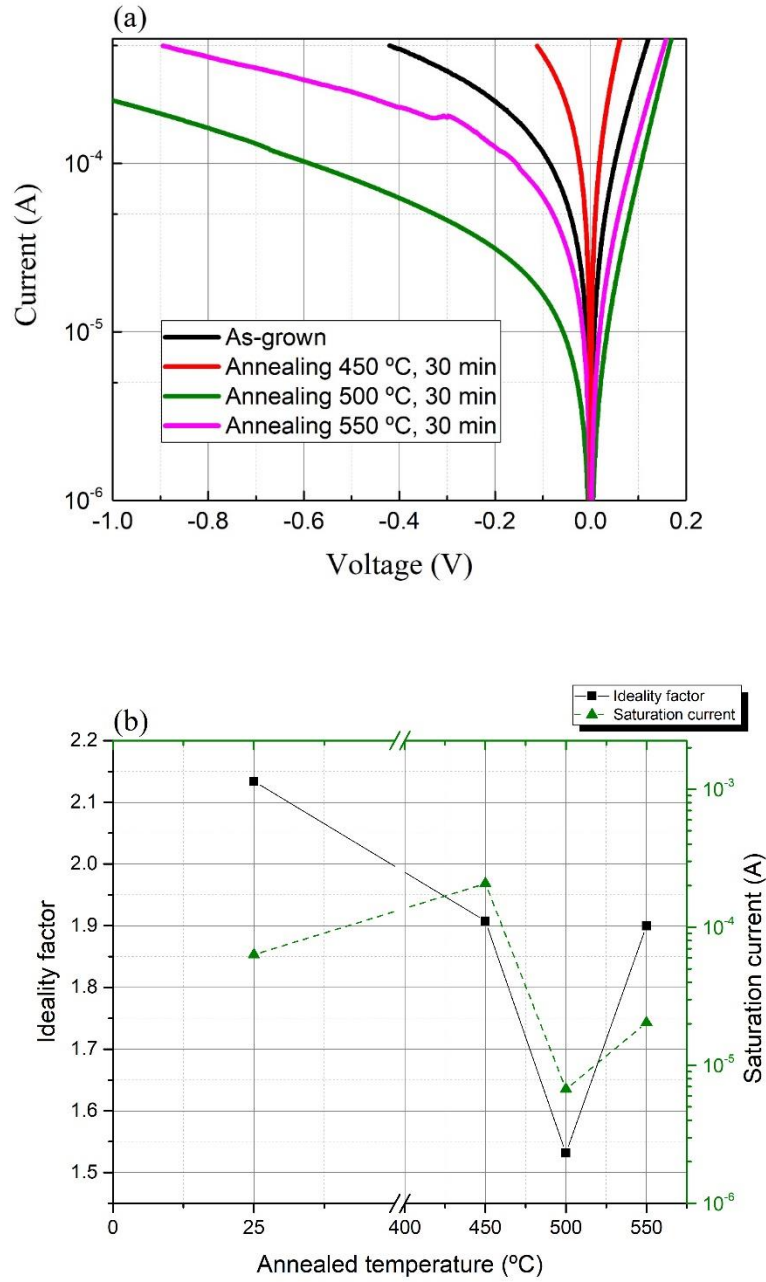
Figure 4. 6. (a) I-V characteristics of Schottky diode sample with 4% Bi at differing annealing temperatures and (b) extracted ideality factor and semi-log plot saturation currents.

4.6 Transmission electron microscopy measurement on annealed GaSbBi samples

To investigate the electrical improvement more closely, the transmission electron microscopy (TEM) was performed on the samples with a Bi content of 4% to look for changes in the material as the anneal temperature is increased. Figure 4. 7 to Figure 4. 11 shows TEM images from the various samples. Three different areas from each sample are also compare with

different resolution. From the as-grown sample [Figure 4. 7], significant defect is noticed as shown in the red circle of Figure 4. 7 (a), it is not possible to determine the exact origin of these defects and faults from this technique, and are likely to be due to a number of different causes including vacancy defects and elemental clustering. A large number of diagonal dislocations can also be observed at the interface between the substrate and epitaxial layer, as show in the red circle of Figure 4. 7 (b), these are characteristic of stacking faults occurring due to the strain mismatch of the layers. Under different resolution, different area (areas 1 to 3) from the same as-grown sample has also been compared between Figure 4. 7(a), (b) and (c), those results confirm the existence of the diagonal dislocation across the sample. Figure 4. 8 shows an increased magnification image around the defects with an ultrahigh atomic scale resolution image in the inset. Unidentified features, which appear as crystallographic faults lying parallel to the {111} planes, can be observed in the Bi alloyed epilayer. These larger stacking faults range in size between 100 and 200 nm.

For the sample annealed at 450 °C [Figure 4. 9], a dramatic reduction can be seen in the density of these dislocations shown in Figure 4. 9(a) and Figure 4. 9(b), with them only being apparent at length scales less than 10 nm [Figure 4. 9(c)]. The dislocations appear to have been completely removed by an annealing temperature of 500 °C across different resolution [Figure 4. 10]. Fast Fourier transform (FFT) intensities [shown in the inset of Figure 4. 10(c)] are consistent with 011 zone axis orientation of the cubic GaSb F-43m structure, [33] indicating that a high quality crystallographic structure has been obtained. It seems likely that these dislocations are one of the key sources of high leakage currents in the devices and that annealing has allowed them to be repaired, giving rise to an improved electrical performance. For the sample annealed at 550 °C [Figure 4. 11] while again there is no evidence of dislocations, there does appear to be a further change in the material with some material clustering be observed, comparing Figure 4. 10(b) and Figure 4. 11(b). Indeed, the lattice parameter obtained from the FFT intensity plot of 6.1180 Å corresponds to a local Bi content of 6.6%, once the elastic constants of GaSb are applied to account for the increased lattice expansion in the growth direction due to pseudomorphic growth. While the XRD of the material annealed at 500 °C indicates negligible change in the average Bi content upon annealing, the TEM suggests that there are regions locally with much higher Bi content of up to 6.6% Bi.

(a)

(b)

(c)
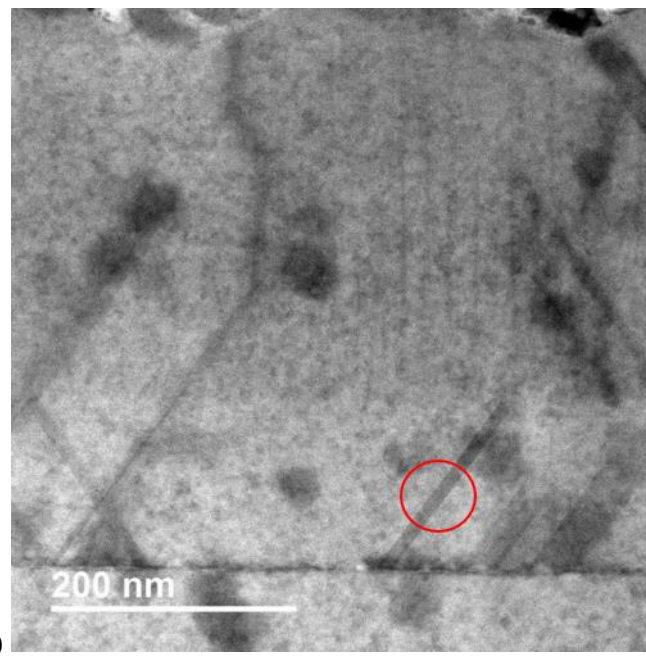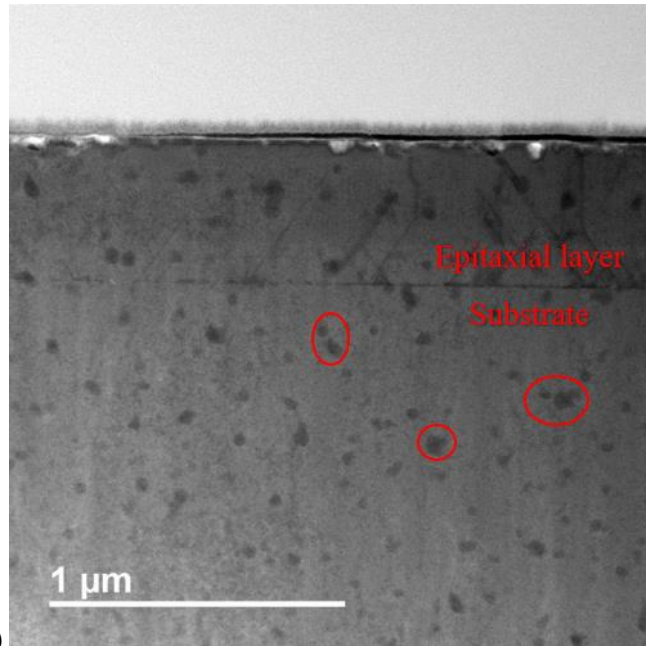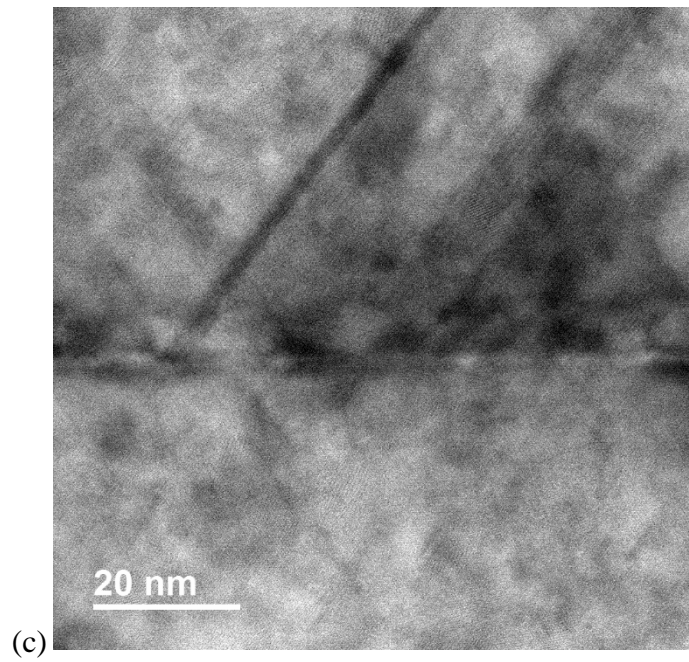
Figure 4. 7. TEM image of Au/GaSbBi Schottky diode, as-grown sample of different area: (a) area 1, (b) area 2 and (c) area 3.
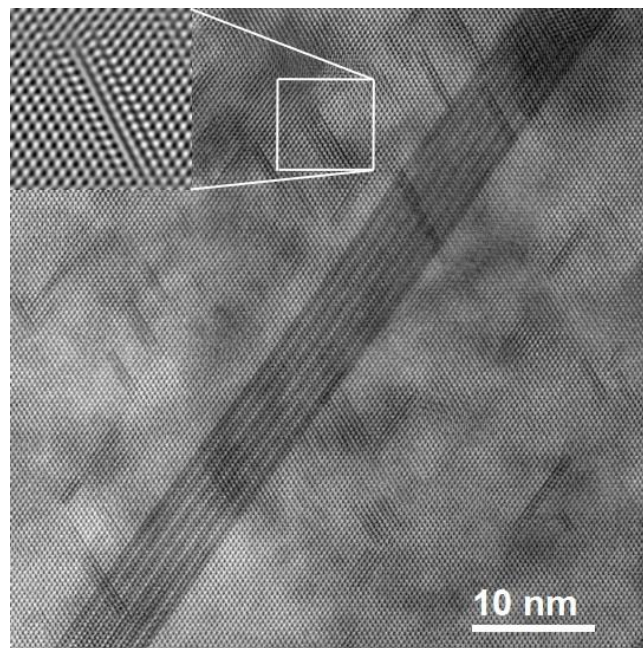
Figure 4. 8. TEM image of Au/GaSbBi Schottky diode, zoomed in image of as-grown sample with atom scale image of crystal matrix in the inset

(a)

(b)

(c)
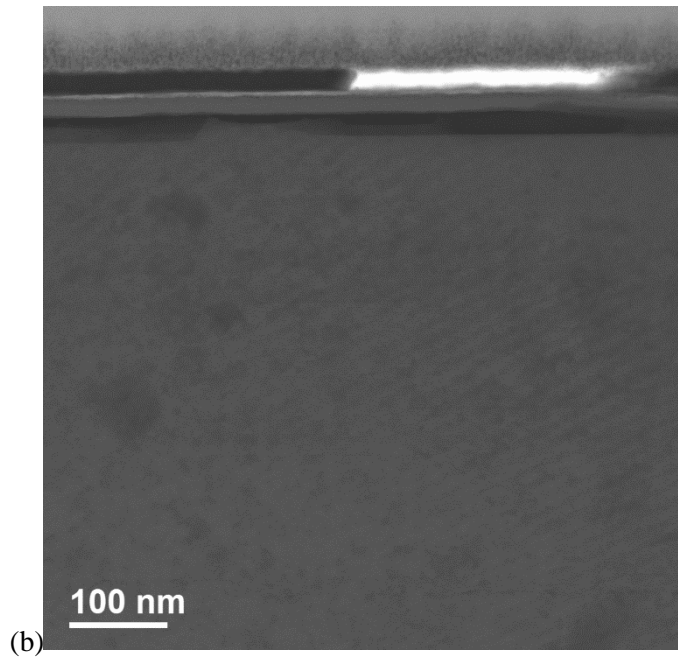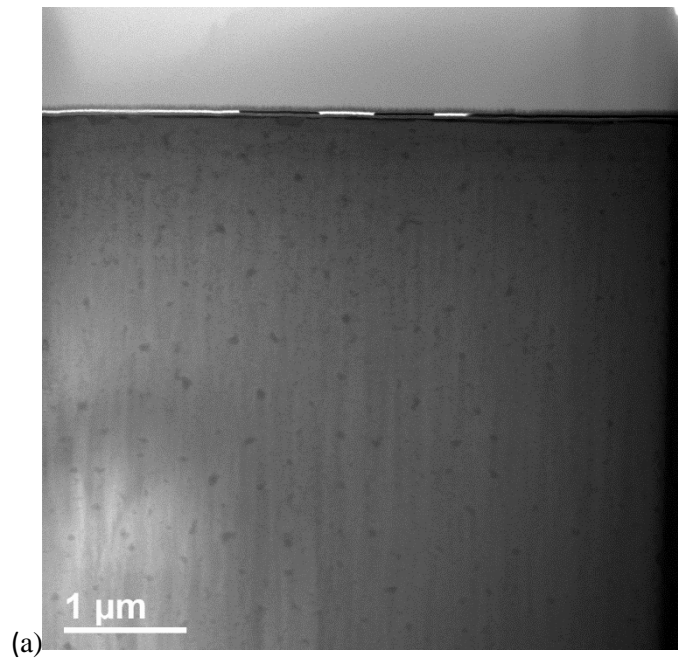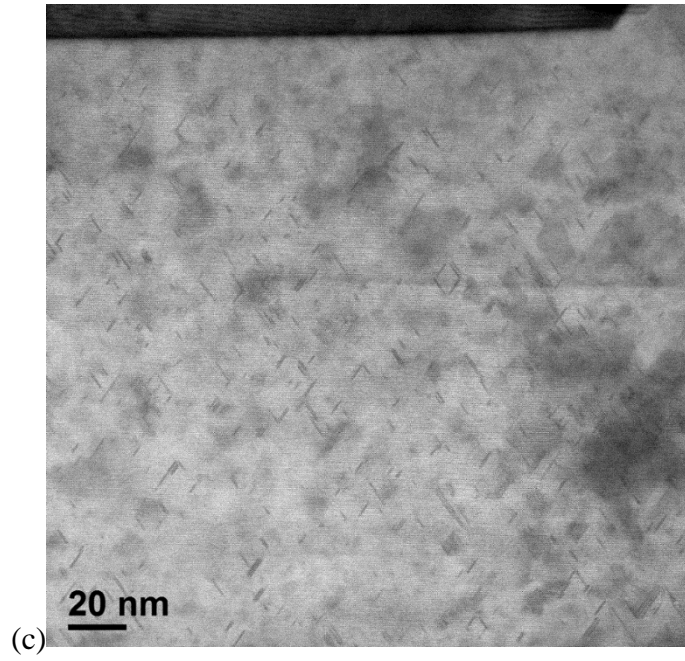
Figure 4. 9. TEM image of Au/GaSbBi Schottky diode, sample annealed at 450 °C of different area: (a) area 1, (b) area 2 and (c) area 3.

(a)

(b)

(c)
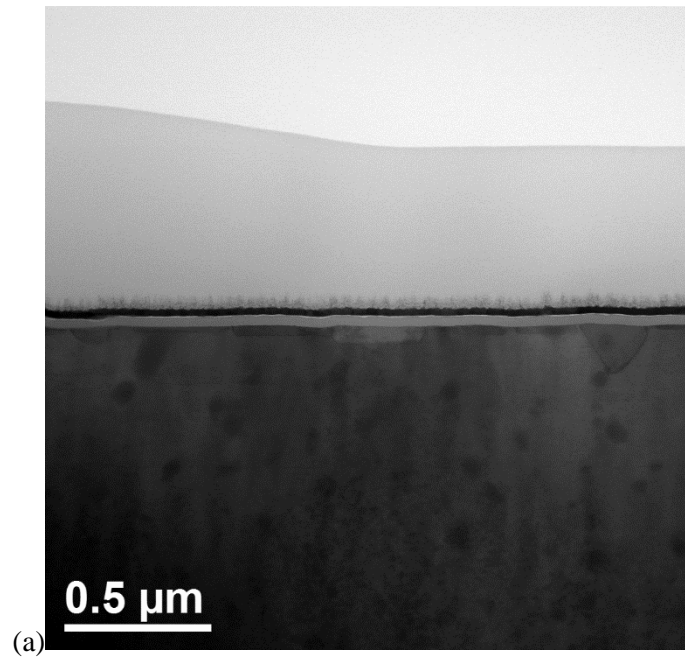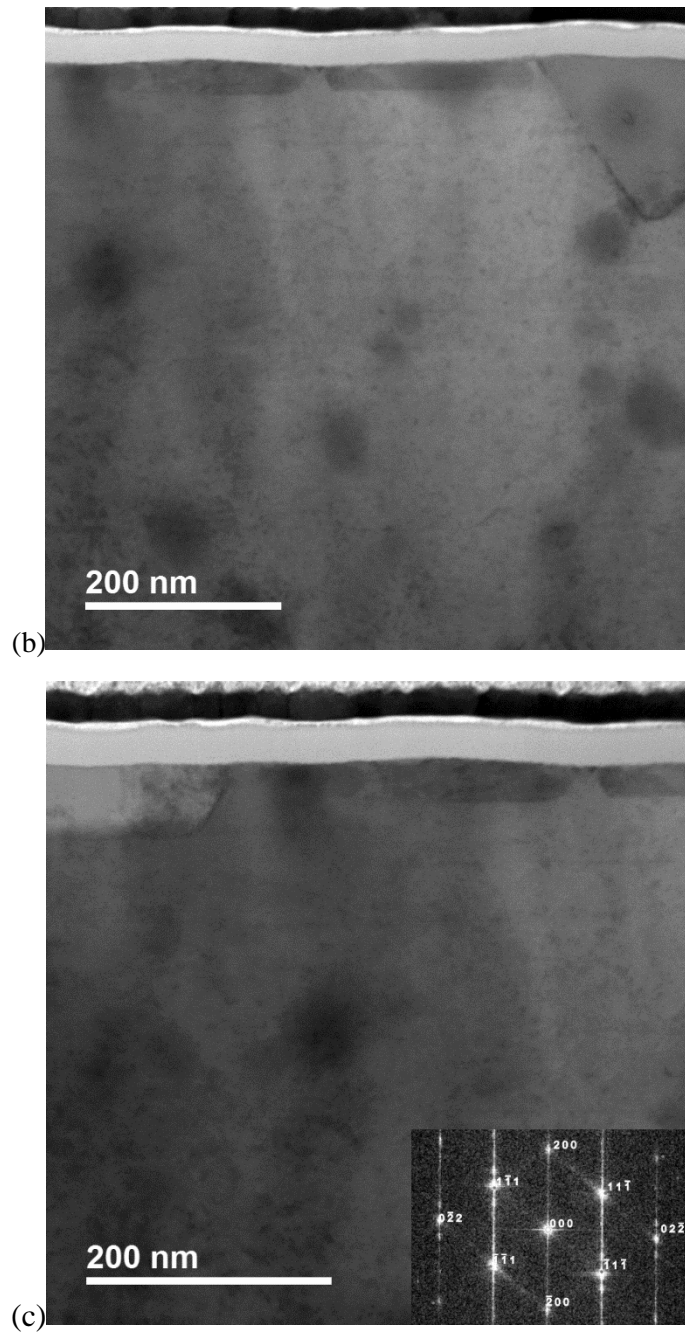
Figure 4. 10. TEM image of Au/GaSbBi Schottky diode, sample annealed at 500 °C of different area: (a) area 1, (b) area 2 and (c) area 3, with inset showing fast Fourier transform (FFT) intensity.

(a)

(b)

(c)
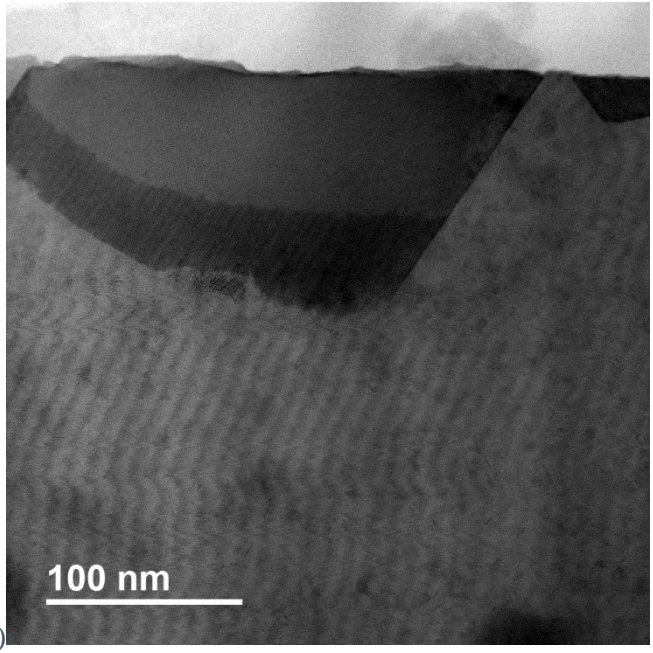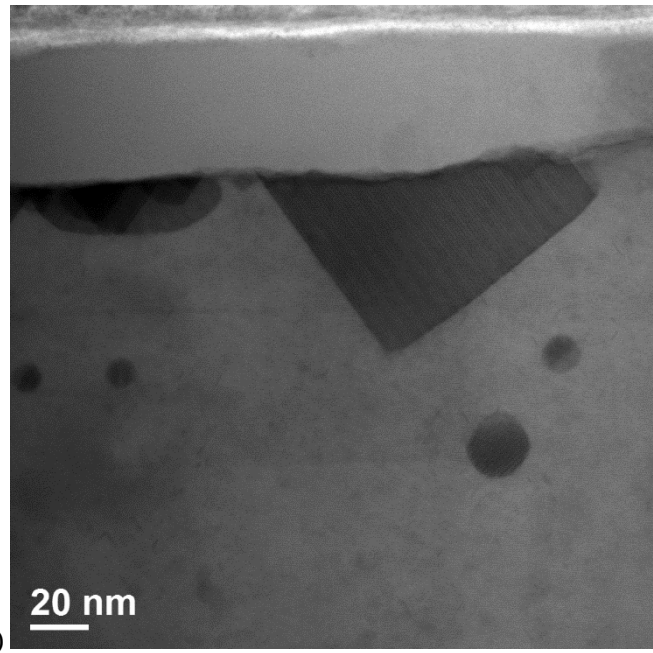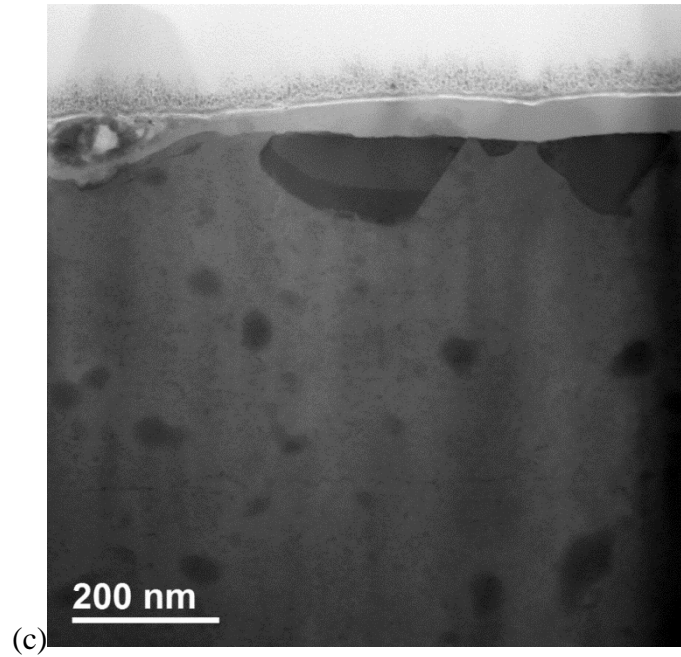
Figure 4. 11. TEM image of Au/GaSbBi Schottky diode, sample annealed at 550 °C of different area: (a) area 1, (b) area 2 and (c) area 3.

4.7 Energy dispersive X-ray measurement on annealed GaSbBi samples

Energy dispersive X-ray (EDX) analysis of this (Figure 4. 12) suggests that the clustering is due to Sb segregation within the epitaxial layer at these higher annealing temperatures. While less apparent at 500 °C, some small areas of Sb segregation are also observed at this temperature. While the mechanism responsible for this apparent movement of Sb within the sample is not clear, one possible explanation could be the movement of Sb atoms via vacancies, through the lattice. This change in material composition is likely to account for the subsequent degradation in the electrical performance of the diodes observed in Figure 4. 6, at the highest annealing temperature. The EDX data has also been used to further investigate the previous anomaly noted in the XRD (Figure 4. 3) data, which suggested a potential reduction in the Bi layer thickness upon annealing. Within the accuracy of the TEM and EDX measurements, the epitaxial layer thickness does not change after annealing; additionally, the Bi composition appears to be uniform in each sample, indicating that Bi out-diffusion has not occurred. The movement of the Sb atoms observed in Figure 4. 12 and the previously discussed Bi clustering noted from the FFT intensity are likely to be influencing the observed XRD result in Figure 4. 3, as after annealing at the highest temperature, compositional nonuniformity has been introduced to the sample, which will influence the experimental data and has invalidated some of the assumptions used in the modelling.

From the TEM and EDX analysis, it appears that upon annealing, the stacking faults are repaired within the sample. However, at higher temperatures, subsequent Sb clustering is observed, indicating that the optimum annealing temperature for GaSbBi is between 450 and 500 °C.

In the previous work [17], researchers have performed capacitance voltage measurements to extract the doping density in GaSbBi Schottky diodes, observing a relatively high p-type doping, which was, in part, attributed to acceptor type defects. In this report, the C-V measurement were performed at room temperature over a range of AC frequencies, and the doping density is extracted from the slope of the $1/C^2$ plot using the Mott-Schottky relationship:

$$ 1\!/\!C^2 = \left(\frac{2}{A^2 \varepsilon_o \varepsilon_s N_{dep}} \right) \left(V_{bi} - \frac{kT}{q} - V \right) \tag{4-1} $$

where A is the area of the device, ε_o is the permittivity of free space, ε_s is the dielectric constant of the semiconductor, N_{dep} is the doping density, V_{bi} is the build-in potential of the junction, V is the applied potential, k is the Boltzmann constant, T is the temperature and q is the charge of the electron.

Utilizing the same approach here for GaSbBi, the hole densities for the as-grown samples were observed as $3.7 \pm 1.5 \times 10^{18}$ cm^{-2} (for the 3.5% Bi sample) and $7.6 \pm 2.4 \times 10^{18}$ cm^{-2} (for the 4% Bi sample), which are in broad agreement with the previous work [17]. After annealing process, the C-V measurement were repeated, no significant change of the doping density of the annealed sample was observed, within the uncertainty of the measurement. This appears to suggest that the annealing process has not significantly altered the number of acceptor type defects present; however, this result should be treated with some caution for two reasons. Firstly, the relatively large uncertainty in the extracted values may be hiding a small change in the doping density, while, secondly, there may be more than one process taking place during the annealing process with each having a different effect on the overall doping density. For example, some of the acceptor-based defects may be repaired during the annealing process, leading to a lowering of the doping density, while the annealing temperature may provide sufficient thermal energy to enable other dopants to become active and hence increasing the effective density.
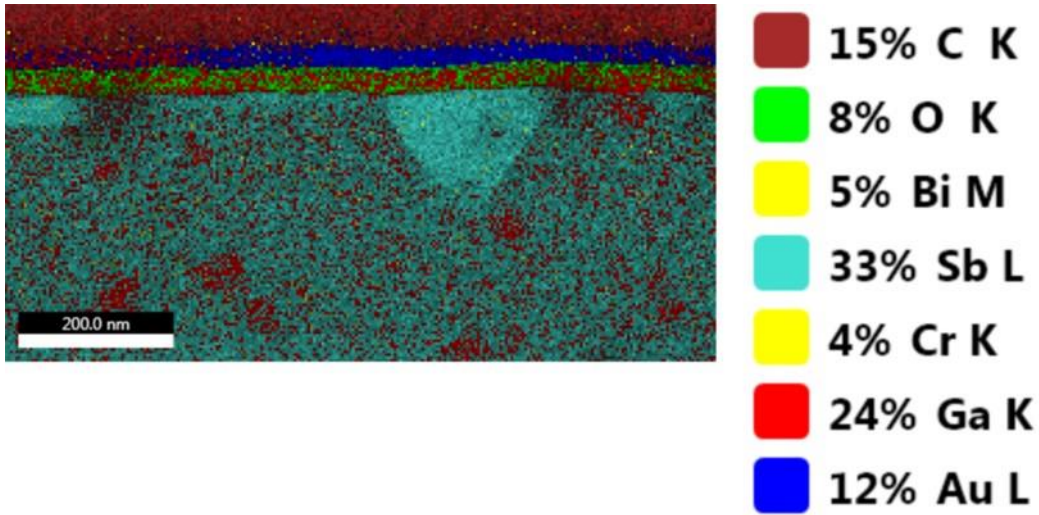
(a)
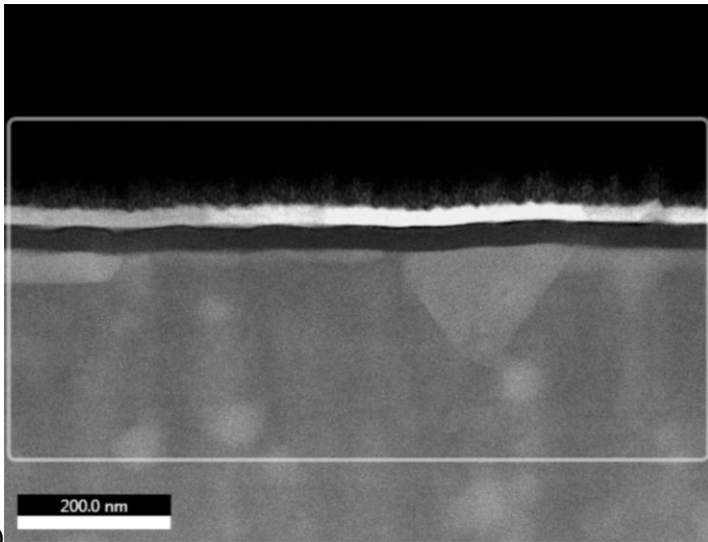
(b)

Figure 4. 12. (a) EDX map and corresponding (b) TEM image of the GaSbBi sample annealed at 550 °C.
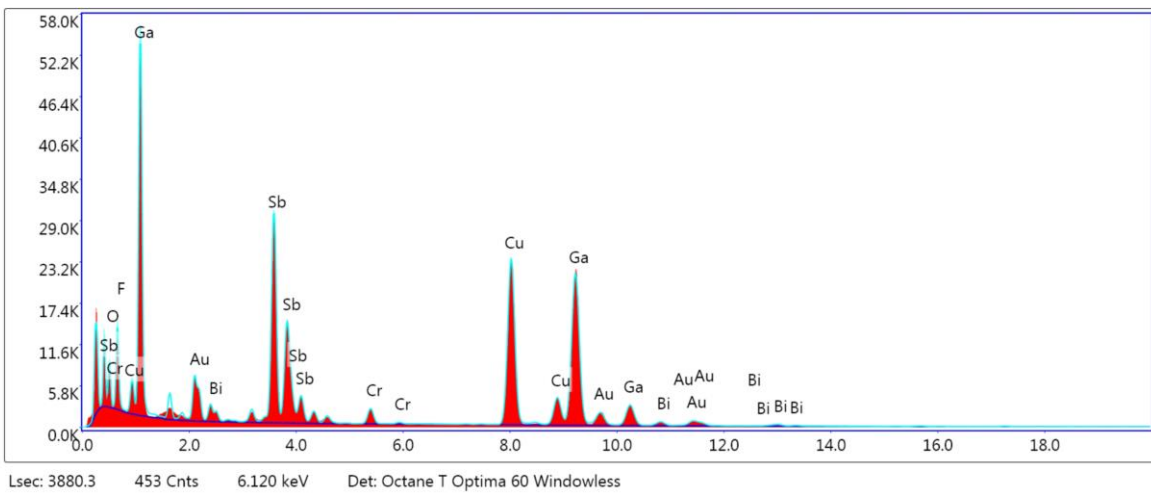
Figure 4. 13. Sum spectrum of GaSbBi sample annealed at 550 °C.

4.8   Conclusion

In this chapter, the influence of postgrowth thermal annealing of GaSbBi Schottky barrier diodes has been investigated. The effects of the annealing temperature and time on the material quality and electrical characteristics of the diodes has been studied. The I-V characteristics indicated a better ideality factor and less leakage current at the reverse bias, resulting in an improvement of the ideality factor from 2.6 to 1.3, as the annealing temperature increased up to 500 °C for a duration of 30 min. X-ray diffraction measurements was performed to verify that the bismuth composition was unaffected during the annealing process. Transmission electron microscopy analysis indicates that this improvement is due to the repair of crystalline dislocations when the sample is annealed. Transmission electron microscopy and energy dispersive X-ray have also indicated a secondary material change associated with Sb movement/clustering that occurs at higher annealing temperatures, causing a degradation in the electrical performance. This chapter indicates that the optimum annealing temperature for GaSbBi alloys is in the range of 450–500 °C. These results provide a route for improving the electrical performance of GaSbBi epitaxial layers, which has potential benefits in realizing high performance optoelectronic devices.

4.9   Reference

[1]   F. M. Mohammedy and M. J. Deen, "Growth and fabrication issues of GaSb-based detectors," *Journal of Materials Science: Materials in Electronics,* vol. 20, no. 11, pp. 1039-1058, 2009.

[2]   M. Motyka *et al.*, "Optical properties of GaSb-based type II quantum wells as the active region of midinfrared interband cascade lasers for gas sensing applications," *Applied Physics Letters,* vol. 94, no. 25, p. 251901, 2009.

[3]   L. Ma *et al.*, "Room-temperature near-infrared photodetectors based on single heterojunction nanowires," *Nano letters,* vol. 14, no. 2, pp. 694-698, 2014.

[4]   H. Li and Z. M. Wang, *Bismuth-containing compounds*. Springer, 2013.

[5]   D. Cooke, F. Hegmann, E. Young, and T. Tiedje, "Electron mobility in dilute GaAs bismide and nitride alloys measured by time-resolved terahertz spectroscopy," *Applied physics letters,* vol. 89, no. 12, p. 122103, 2006.

[6]   M. Polak *et al.*, "Theoretical and experimental studies of electronic band structure for GaSb1− xBix in the dilute Bi regime," *Journal of Physics D: Applied Physics,* vol. 47, no. 35, p. 355107, 2014.

[7]   M. Rajpalke, W. Linhart, K. Yu, T. S. Jones, M. Ashwin, and T. D. Veal, "Bi flux-dependent MBE growth of GaSbBi alloys," *Journal of Crystal Growth,* vol. 425, pp. 241-244, 2015.

[8]   M. Rajpalke *et al.*, "Growth and properties of GaSbBi alloys," *Applied Physics Letters,* vol. 103, no. 14, p. 142106, 2013.

[9]   H. Kim, Y. Guan, S. E. Babcock, T. F. Kuech, and L. J. Mawst, "Characteristics of OMVPE grown GaAsBi QW lasers and impact of post-growth thermal annealing," *Journal of Applied Physics,* vol. 123, no. 11, p. 113102, 2018.

[10]   I. P. Marko *et al.*, "Optical gain in GaAsBi/GaAs quantum well diode lasers," *Scientific reports,* vol. 6, p. 28863, 2016.

[11]   R. D. Richards, C. J. Hunter, F. Bastiman, A. R. Mohmad, and J. P. R. David, "Telecommunication wavelength GaAsBi light emitting diodes," *IET Optoelectronics,* vol. 10, no. 2, pp. 34-38, 2016.

[12]   G. Feng, K. Oe, and M. Yoshimoto, "Influence of thermal annealing treatment on the luminescence properties of dilute GaNAs–bismide alloy," *Japanese Journal of Applied Physics,* vol. 46, no. 8L, p. L764, 2007.

[13]   O. Delorme, L. Cerutti, E. Tournié, and J.-B. Rodriguez, "Molecular beam epitaxy and characterization of high Bi content GaSbBi alloys," *Journal of Crystal Growth,* vol. 477, pp. 144-148, 2017.

[14]   Y. Song, S. Wang, I. Saha Roy, P. Shi, and A. Hallen, "Growth of GaSb1− xBix by molecular beam epitaxy," *Journal of Vacuum Science & Technology B, Nanotechnology and Microelectronics: Materials, Processing, Measurement, and Phenomena,* vol. 30, no. 2, p. 02B114, 2012.

[15]   S. Das, T. Das, and S. Dhar, "Effect of post-growth anneal on the photoluminescence properties of GaSbBi," *Semiconductor Science and Technology,* vol. 29, no. 1, p. 015003, 2013.

[16]   C. R. Tait and J. M. Millunchick, "Kinetics of droplet formation and Bi incorporation in GaSbBi alloys," *Journal of Applied Physics,* vol. 119, no. 21, p. 215302, 2016.

[17]   N. Segercrantz *et al.*, "Hole density and acceptor-type defects in MBE-grown GaSb1-x Bi x," *Journal of Physics D: Applied Physics,* vol. 50, no. 29, p. 295102, 2017.

[18]   M. K. Rajpalke *et al.*, "High Bi content GaSbBi alloys," *Journal of applied physics,* vol. 116, no. 4, p. 043511, 2014.

[19]   L. Yue *et al.*, "Molecular beam epitaxy growth and optical properties of high bismuth content GaSb1-xBix thin films," *Journal of Alloys and Compounds,* vol. 742, pp. 780-789, 2018.

[20]   J. Hilska, E. Koivusalo, J. Puustinen, S. Suomalainen, and M. Guina, "Epitaxial phases of high Bi content GaSbBi alloys," *Journal of Crystal Growth,* vol. 516, pp. 67-71, 2019.

[21]   O. Dier, C. Lin, M. Grau, and M.-C. Amann, "Selective and non-selective wet-chemical etchants for GaSb-based materials," *Semiconductor Science and Technology,* vol. 19, no. 11, p. 1250, 2004.

[22]   B. Rotelli, L. Tarricone, E. Gombia, R. Mosca, and M. Perotin, "Photoelectric properties of GaSb Schottky diodes," *Journal of applied physics,* vol. 81, no. 4, pp. 1813-1819, 1997.

[23]   O. Delorme *et al.*, "GaSbBi/GaSb quantum well laser diodes," *Applied Physics Letters,* vol. 110, no. 22, p. 222106, 2017.

[24]   L. A. Gianuzzi and F. A. Stevie, "Introduction to focused ion beams," *Instrumentation, theory, techniques and practice. New York: Springer Science+ Business Media,* p. 201, 2005.

[25]   S. Haywood, N. Mason, and P. Walker, "Growth of GaSb by MOVPE; Optimization of electrical quality with respect to growth rate, pressure, temperature and IIIV ratio," *Journal of Crystal Growth,* vol. 93, no. 1-4, pp. 56-61, 1988.

[26]   P. K. Rao and V. R. Reddy, "Effect of annealing temperature on electrical and structural properties of transparent indium tin oxide electrode to n-type GaN," *Materials Chemistry and Physics,* vol. 114, no. 2-3, pp. 821-826, 2009.

[27]   R. T. Tung, "Recent advances in Schottky barrier concepts," *Materials Science and Engineering: R: Reports,* vol. 35, no. 1-3, pp. 1-138, 2001.

[28]   J. H. Werner and H. H. Güttler, "Barrier inhomogeneities at Schottky contacts," *Journal of applied physics,* vol. 69, no. 3, pp. 1522-1533, 1991.

[29]   F. Ruffino, M. Censabella, G. Piccitto, and M. Grimaldi, "Surface roughness effect on the electrical characteristics of Pd/SiC nanocontacts," *Applied Surface Science,* vol. 529, p. 147142, 2020.

[30]   S.-H. Jang and J.-S. Jang, "Electrical characteristics and carrier transport mechanism for Ti/p-GaN Schottky diodes," *Electronic Materials Letters,* vol. 9, no. 2, pp. 245-249, 2013.

[31]   A. Duzik and J. M. Millunchick, "Surface morphology and Bi incorporation in GaSbBi (As)/GaSb films," *Journal of crystal growth,* vol. 390, pp. 5-11, 2014.

[32]   X. Liu, H. Li, F. Guo, M. Li, and L. Zhao, "Effect of annealing on electrical properties of InAsSb films grown on GaAs substrates by molecular beam epitaxy," *Physica E: Low-dimensional Systems and Nanostructures,* vol. 41, no. 9, pp. 1635-1639, 2009.

[33]   R. Wyckoff, "Interscience publishers, new york, new york rocksalt structure," *Crystal structures,* vol. 1, pp. 85-237, 1963.

Chapter 5

5. GaSbBi metal semiconductor metal detectors for mid-infrared sensing

5.1 Introduction

The Mid-infrared (MIR) spectral range has been widely employed in many sciences and technical fields, optoelectronic devices working between 2 to 5 μm spectral domain have great potential in areas such as night vision imaging, telecommunications and molecular spectroscopy. Night vision imaging is obtained as objects emit radiation in the MIR regimes, which applied in the condition without additional light source [1]. Gas sensing with a high resolution can also be developed because lots of polluting gas, such as CO (4.8μm), CO_2 (4.24μm) and CH_4 (3.4μm), have strong absorption lines in the MIR domain [2]. MIR radiation can also travel through the atmosphere without significant losses. Due to this high transparency, MIR radiation can find many application in free-space communications [3]. Military vision enhancement, industrial leakage detection and missile tracking are among important usages of MIR detection.

In order to fulfil the increasing demand, high-performance MIR detectors with high responsivity and low dark current are eagerly pursued. One of the most widely used semiconductor materials for fabricating MIR detectors is Mercury Cadmium Telluride (HgCdTe). The specific advantages of HgCdTe are the direct energy gap, ability to obtain both low and high carrier concentrations, high mobility of electrons and low dielectric constant. The minimal change of lattice constant with composition makes it possible to grow high-quality layers and heterostructures [4]. However, the primary motivation for replacing HgCdTe is the price and the technological disadvantage to fabricate the material [5], which makes it less completive in some area. Others material such as InGaAs have also been used to explore the infrared area due to the similar band structure with HgCdTe. Commercial InGaAs photodiodes mainly operate in the wavelength range around 2 μm, some of the InGaAs photodiodes have shown high device performance close to the theoretical limits which can get extended to 2.5 um, but the performance decreases rapidly due to large lattice mismatch [6].

Over the past few years, researchers have begun to investigate on the band structure of GaSbBi and GaSbN. Das et al. [7] have investigated the band structure of GaSbBi as functions of Bi mole fraction and along with different symmetry directions of the crystal by using a 14 band

k.p anti-crossing model. Sharma et al. [8] have used a two-oscillator model to investigate the relevant parameters that explain the temperature dependence of the bandgap energy for GaSbBi. The effect of two different phonon modes, due to GaSb and GaBi, on the temperature dependent bandgap is interpreted. The result indicates that the phonon dispersion co-efficient (the relationship between phonon frequency and wave vector is known as the phonon dispersion) is reduced with the increase of Bi content in the material, which is due to the decrease in the contribution of low energy acoustical phonon with the increase in Bi. Wang et al. [9] have studied the band structure of dilute nitride GaSbN bulk materials by photoluminescence and optical absorption measurements, demonstrating a bandgap reduction up to 300 meV with increasing nitrogen incorporation. Comparatively, there are few journals reported realizing band structure and optical properties of GaSbBi and GaSbN via a complex optoelectronic device such as quantum well laser diodes [10, 11], quantum dots [12] and nanowire structure [13]. As such, there is still significant work that can be achieved to simplify the fabrication process for a proof of concept.

In this chapter, the viability of using GaSbBi and GaSbN as active layers in photodetector is investigated. The epitaxial growth of a full GaSbBi photodetector structure is complicated, due to the need to grow thick layers and possible strain issues, additionally the fabrication process will need extensive development of appropriate etching and passivation procedures. To simplify the research process, the thin film GaSbBi and GaSbN grown on GaSb substrates are used to assess the material property as a photoconductive detector. The spectral response characteristics are compared to study the quality of the device and the effect of Bi incorporation on the photo responses.

5.2   Experimental detail

5.2.1   GaSbBi and GaSbN growth

The following thin film GaSbBi and GaSbN wafers were grown by the Department of Physics at the University of Warwick. The thin film GaSbBi were grown by solid-source MBE on GaSb (001) undoped substrates with an initial GaSb 100nm buffer layer. The Bi incorporations in the GaSbBi epilayers were characterised using Rutherford backscattering [14]. The Bi concentration in the GaSbBi samples used in this work varying from 2.9% to 4.5%, are listed in Table 5. 1. The thin film GaSbN used in this work were grown by plasma-assisted MBE semi-insulating GaAs (001) substrates. The N contents of the relaxed films were determined from x-

ray diffraction [15]. The N concentration in the GaSbN sample used in this work is listed in Table 5. 1.

Table 5. 1 Content details of GaSb, GaSbBi and GaSbN samples.

	Material	Bi%	N%
Sample 1	GaSb	GaSb control	GaSb control
Sample 2	GaSbBi	2.9	
Sample 3	GaSbBi	3.8	
Sample 4	GaSbBi	4.5	
Sample 5	GaSbN		1.5

5.2.2 Device fabrication

Group of thin film GaSbBi, GaSbN and GaSb wafers, as shown in Table 5. 1, are used and fabricated into metal-semiconductor-metal photodetectors (MSM-PDs). The wafers were first cleaved into the size of 1×1 cm^2 and then cleaned with acetone and isopropyl alcohol for 10 min each. The samples were dried by nitrogen gun before patterned with different geometry contacts via a standard photolithography process, using the positive photo-resist Shipley 1813. The interdigit top electrode was patterned, and Al was deposited by thermal evaporation to a thickness of 50 nm. The unwanted Al was lifted off using acetone then the sample was dried under N_2. Six different types of geometry with interdigit gaps varying from 20 to 100 µm were compared to study the effect on spectral responses, as shown in Figure 5. 1. The shape of bar and zigzag are both common electrode shapes that many other researchers have used to study the different optical characteristics of MSM-PDs. The main advantages of a zigzag geometry compared to bar electrodes is the increased surface area giving a greater "edge" between the electrodes for carriers to be extracted Also, the gap distance is the standard distance used in the research. In my design, I have also managed to keep metal contact ratio at same level, as to keep the reflection over absorption ratio same. The detail of different geometry is listed in Table 5. 2.

Current-voltage (IV) measurements under dark conditions and under illumination from a Thorlabs SLS202L/M infrared light source were performed by an Agilent Technology B1500A Semiconductor Device Analyzer. The MSM-PDs were directly probed via a probe station at room temperature. The infrared light source is directed at the centre of the device using a single-mode fibre.

In order to investigate the photo responses upon illumination, the fabricated MSM-PDs sample is placed into a calibrated Horiba iHR320 monochromator system. A Stanford Research SR570 low-noise current pre-amplifier and a Stanford research SR850 DSP lock-in amplifier with an optical chopper are used to recover the photocurrent and minimise the effect of noise. The optical chopper rotates at 330 Hz is placed in between the output light source of the monochromator system and the fixed sample. The Lock-in amplifier utilises phase-sensitive-detection to enable weak signals to be extracted from noisy signals. The lock-in-amplifier uses the frequency of the optical chopper as a reference signal to detect input signals that vary with the same frequency and hence suppresses other sources of noise. For this reason, the chopping frequency was selected to be away from an integer multiple of 50 Hz, to ensure no mains related noise was picked up.
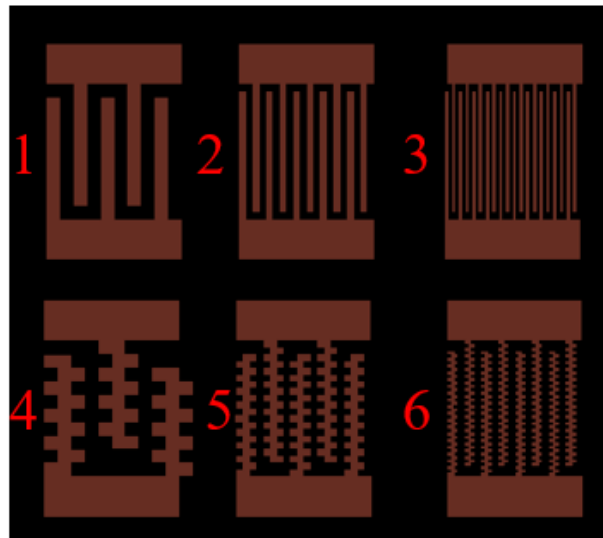
Figure 5. 1 Top view of different interdigit electrode.

Table 5. 2 Detail of different geometry of the interdigit electrode.

Active area (μm^2)	Device number	Gap (μm)	Finger numbers	Metal contact ratio	Finger type
	1	100	5	0.66	Bar
	2	50	10	0.67	Bar
	3	25	20	0.67	Bar
1000*1600	4	100	3	0.71	Zigzag
	5	50	5	0.66	Zigzag
	6	50	8	0.61	Zigzag

5.3   Result and discussion

5.3.1   Cut-off wavelength comparison of GaSb, GaSbBi and GaSbN MSM-PDs

To better understand the spectral responsivity of different material, a group of GaSb and GaSbBi MSM-PDs device with different Bi content were compared. Figure 5. 2 shows the normalised intensity responses of GaSb and GaSbBi MSM-PD device with the Bi content of 2.9% and 3.8%. A clear extension in the cut-off wavelength (defined as 10% of the maximum intensity in this chapter) can be observed for GaSbBi samples. The cut-off wavelength has extended from a reference GaSb MSM-PD device at 1720 nm, to 1990 nm for the GaSbBi MSM-PD device with 3.8%. The cut-off wavelength extension has also been observed depending on Bi incorporation, which the GaSbBi sample with the Bi content of 2.9% has a cut-off wavelength length at 1950 nm. This extended cut-off wavelength is caused by the incorporation of Bi into the active layer of the MSM-PDs, indicating a direct bandgap reduction. The bismuth content of the sample used in this work has been confirmed by Rutherford backscattering experiment in previous work [14]. As such, the 230-270 nm cut-off wavelength extension observed in the spectral response measurement. This cut-off wavelength shift on GaSbBi MSM-PDs suggest a corresponding bulk bandgap reduction in the range of 26-29 meV/%Bi.

Most previous studies on GaSb have indicated a bandgap at room temperature of about 720 meV [16, 17], which corresponds to a cut-off wavelength at around 1722 nm. While incorporated Bi atom into GaSb host material can modify both conduction and valence band, and thus significantly reduce the bandgap. For the GaSbBi, several literatures have shown that the bandgap reduction is about 28-40 meV/%Bi at room temperature [18-22]. The key parameters for the MSM-PDs GaSb and GaSbBi spectral responses measurements are listed in Table 5. 3. It can be seen that good agreement with these previous studies have suggested the viability of using Bi to extend the operation wavelength of GaSb photodetectors.
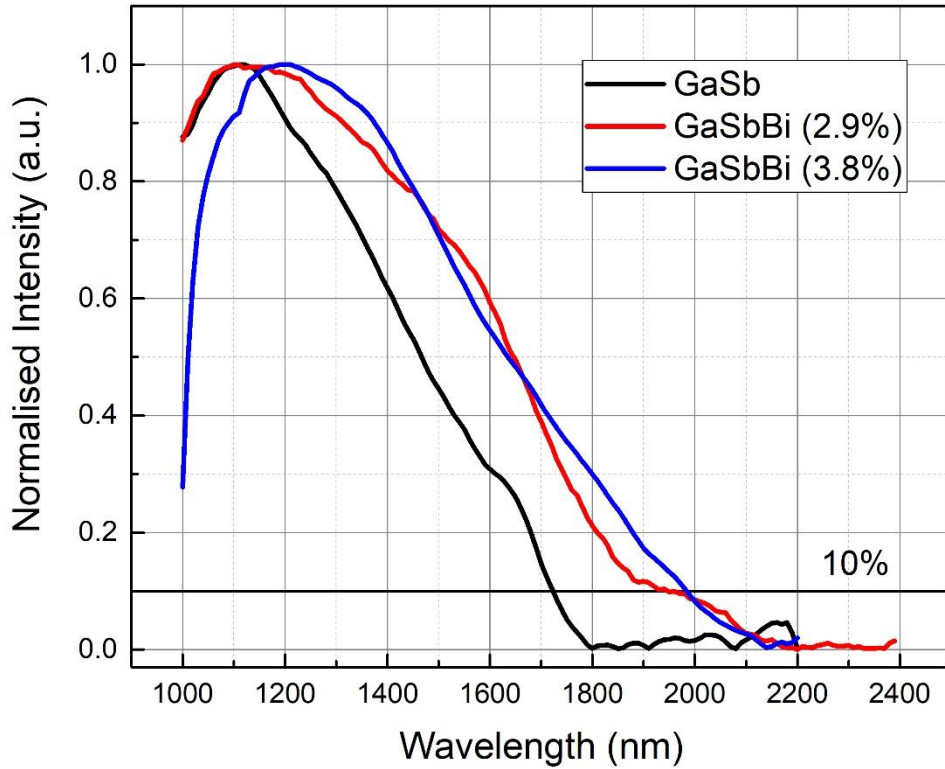
Figure 5. 2 Spectral responses of GaSb and GaSbBi MSM-PDs with different Bi incorporation at room temperature

Table 5. 3 Key parameters for the GaSb and GaSbBi MSM-PDs with different Bi incorporation

Material	Device type	A bias voltage (V)	Cut-off wavelength (nm)	Estimate bandgap reduction (meV/Bi%)
GaSb	3	0.1	1720	N/A
GaSbBi (2.9%)	3	0.2	1950	29
GaSbBi (3.8%)	3	0.01	1990	26

To better understand the cut-off wavelength extension on the Bi incorporation and also study the effect of dilute nitride on GaSb photodetector, another group of thin film GaSbBi and GaSbN MSM-PDs have been used to investigate the cut-off wavelength by comparing with a

reference GaSb MSM-PDs. All the device is measured under photoconductive mode. Figure 5. 3 show the spectral response of GaSb, GaSbBi (4.5%) and GaSbN (1.8%) MSM-PDs. Significant wavelength extension has also been observed for the GaSbBi device with 4.5% Bi incorporation. The cut-off wavelength has extended from 1720 nm (reference GaSb device) to 2080 nm, as shown in Table 5. 4. The estimated bandgap reduction is around 28 meV/%Bi, which has good agreement with previous studies [22] as well as the results above.

Meanwhile, the GaSbN device with 1.5% N incorporation has presented a 470 nm wavelength extension compared to the GaSb device. It is noticed that the estimated bandgap reduction for the GaSbN device has indicated a 103 meV/%N. However, previous studies on the band structure of GaSbN has suggested the bandgap reduction of N is in a range of 168 to 300 meV/%N [9, 23, 24], the estimated result obtained in this work indicating some of the difficulties in achieving accurate low-level N incorporation. The smaller than expected bandgap reduction could due to the GaSbN layer being too thin to generate appreciable absorption, the film was grown to a thickness in 350 nm on GaSb (001) substrate. As such light at wavelengths up to the cut off wavelength of GaSb have a significant thickness in which to be absorbed, however at the longer wavelengths only absorbed by GaSbN there is only a thin layer in which to generate carriers. This may have caused the longer wavelength tail of the spectra to be obscured and masked. reducing the mobility of the carrier leading to a reduced shift of the absorption edge [9], therefore getting the effect of noise. Another possibility for this discrepancy may come from any non-uniformity in the N content of the GaSbN layer, the previous RBS measurements, provide an average content for a relatively large area on the wafer (in the order of $1mm^2$), as such this may form areas of higher and lower concentration.

However, to the best of my knowledge, this is the first observation of an extended wavelength response in an actual photodetector device. While the wavelength extension indicates that both Bi and N can indeed be used to extend the operation wavelength of GaSb photodetectors, it does not provide any information regarding any change in efficiency upon Bi and N incorporation.
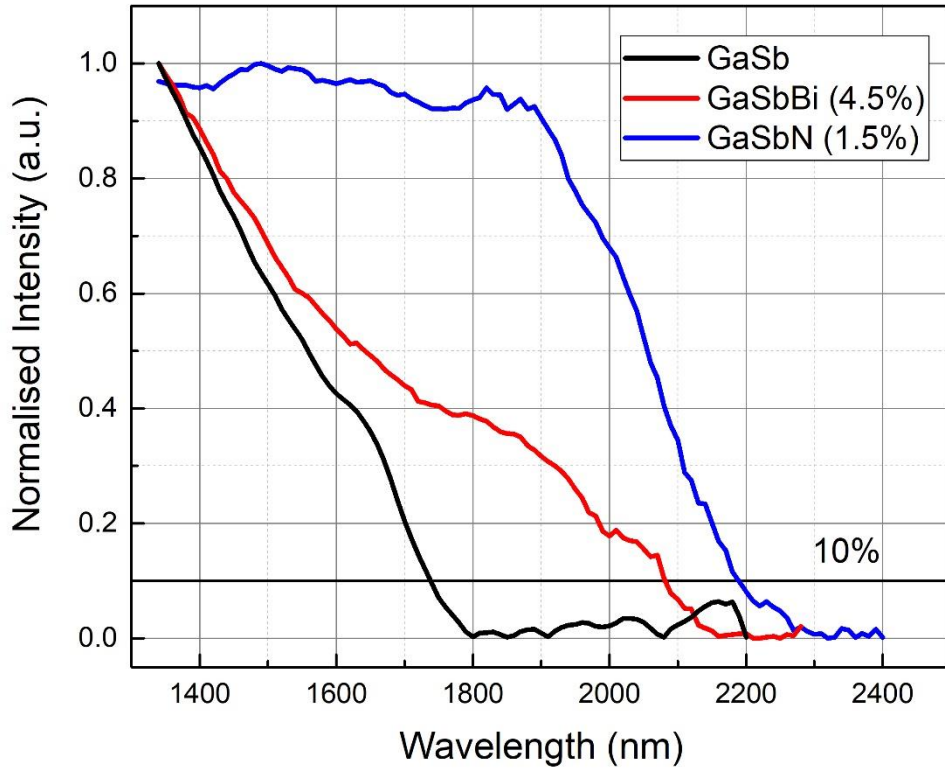
Figure 5. 3 Spectral responses of GaSb, GaSbBi and GaSbN MSM-PDs at room temperature

Table 5. 4 Key parameters for the spectral responses of GaSb, GaSbBi and GaSbN MSM-PDs

Material	Device type	A bias voltage (V)	Cut-off wavelength (nm)	Estimate bandgap reduction (meV/Bi%)
GaSb	2	0.1	1720	N/A
GaSbBi (4.5%)	2	0.1	2080	28
GaSbN (1.5%)	2	-0.02	2190	103

5.3.2   Responsivity
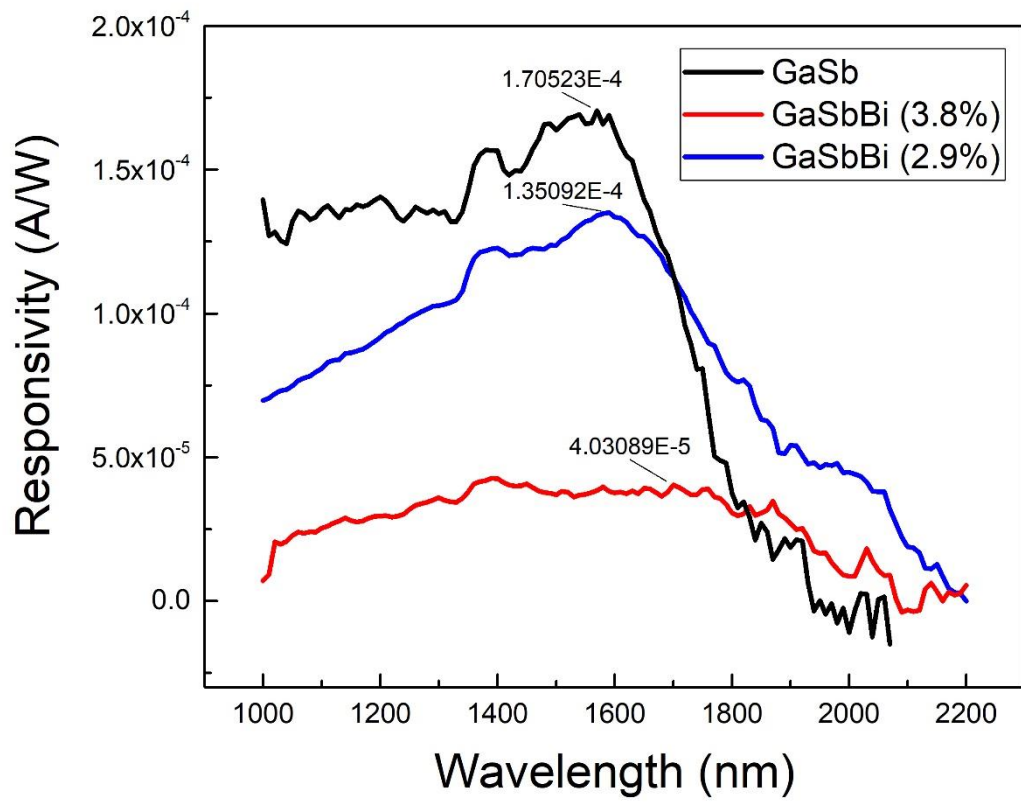
Figure 5. 4 Spectral photo response of GaSb and GaSbBi MSM-PDs with different Bi incorporation, measured at room temperature
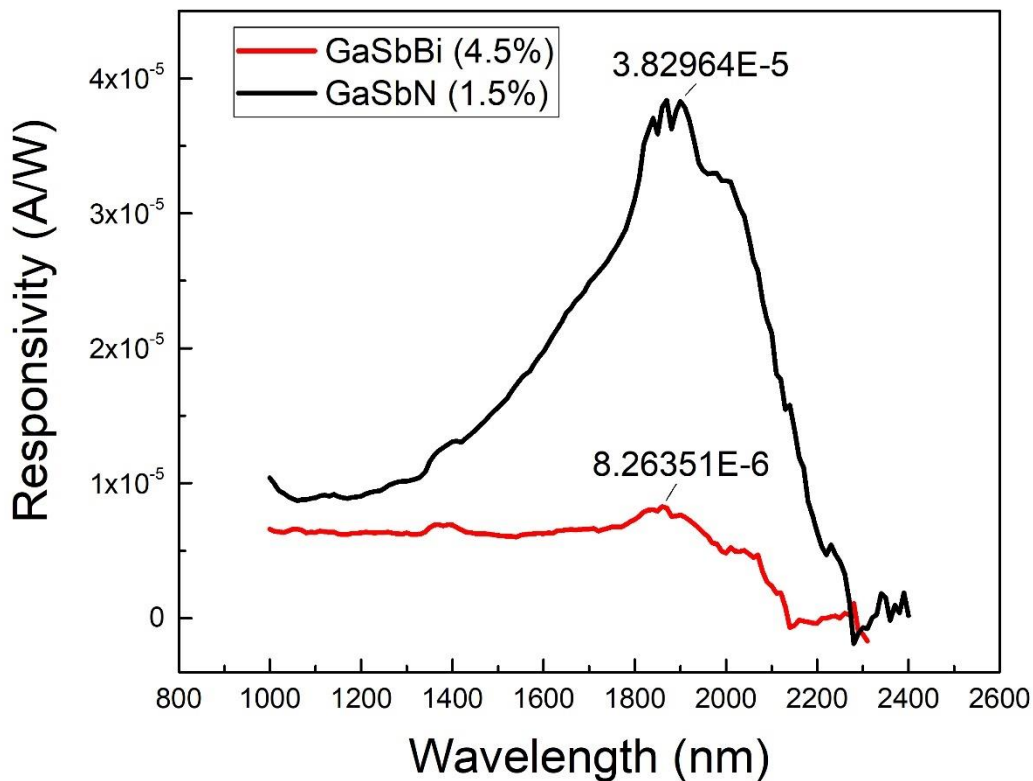
Figure 5. 5 Spectral photo response of GaSbBi and GaSbN MSM-PDs measured at room temperature

To better understand the wavelength extension and resulting material quality, two groups of MSM-PDs devices have also been measured and used to calculate the spectral responsivity. The output power of the monochromator system is quantified by using a Thorlabs FD05D InGaAs photodiode. The measured photocurrent is used in conjunction with the known responsivity of the commercial diode to calculate the output power from the monochromator as a function of wavelength. The calculated incident light power is then used to calculate the spectral responsivity of the MSM-PDs devices. Different bias is applied for each device, with the response generating the maximum response being used here. An improvement of responsivity for the device is expected as the bias voltage increased, due to the external field improving the extraction of the photo generated carriers, however this comes at a cost of higher dark currents.

In this work, multiple devices were fabricated under the same condition were measured (minimum of six per wafer). The typical results obtained from each device were used to compare the spectral photo response of different material. Figure 5. 4 illustrate the spectral responsivity for the GaSb and GaSbBi MSM-PDs with different Bi incorporation. It can be

seen that the responsivity of the device decreases with an increase in the wavelength. A similar trend of the responsivity has been observed for different devices, with the GaSb device exhibited the highest value of the peak responsivity of 1.7×10^{-4} A/W at 1570 nm, and the GaSbBi device with 3.8% Bi content has the lowest value of the peak responsivity of 4.0×10^{-5} A/W at 1700 nm. The obtained result seems to suggest that the wavelength extension is achieved with a slight reduction in the responsivity. One possible explanation for the differences between the measured responsivity is the misalignment of the light beam on the device during each measurement. The magnitude of which could be due to experimental uncertainties. This result seems to suggested that the device quality is not significantly degraded by the addition of Bi.

Repeated measurement on the second group GaSbBi and GaSbN devices, shown in Figure 5. 5, illustrate that the peak responsivity for the GaSbBi and GaSbN device, which were shown to be 8.3×10^{-6} A/W at 1860 nm and 3.8×10^{-5} A/W at 1900 nm, respectively. These results are confirming that the wavelength extension of the devices have not degraded the optical quality. While it should be noted that these values of responsivity are very low, the key results of this work are in confirming the predicted wavelength extension in a photodetector device, while exhibiting minimal degradation in the responsivity compared to the reference GaSb device. The photocurrent generated in the devices is influenced by both the absorption coefficient of the material and the extraction efficiency of the device (i.e. how easily the photo generated carriers can move to the contacts), as such it is not possible to directly calculate the absorption coefficient of GaSbBi samples from this work. However, previous study [21] has used transmittance measurements on thin layers of as-grown GaSbBi samples (similar thickness to those used here) with Bi content ranging from 1.6 to 9.6%. The subsequent absorption coefficient, calculated from the transmittance data, has given values for the peak absorption coefficient for GaSbBi samples is up to 1.7×10^4 cm^{-1}. Based on these values we would only expect around 20% of the light incident on our samples to be absorbed at the peak wavelength. This indicates the scope and need for enhanced device designs (thicker layers) to help improve the responsivity values calculated here.

Commercially available photodetectors typically utilise either a pn or p-i-n configuration, enabling much thicker layers to be used, allowing more absorption of the incident signal, such configurations also exhibit stronger internal electric fields to enhance carrier extraction. Based on the previous work [21], it is estimated that only around 10% of the incident light will be absorbed in these devices, indicating there is considerable room for further improvement in terms of device design.

Additionally, commercial detectors are made from much more mature materials (i.e. Ge, InGaAs, etc.) whereas the GaSbBi here, is very much in its infancy, with considerable room for further improvement in material growth and development, for example perhaps by utilising post growth annealing techniques to enhance the material quality as shown in chapter 4. As such, comparison between these results and commercial devices is not appropriate here. The calculation used in this work has also underestimated the responsivity. It is assumed that all of the light outputted from the monochromator at each wavelength is incident on the active area of the device, however as noted in Figure 5. 2, only around a third of the device area is exposed semiconductor, with the rest being metal which will reflect the incident light. Secondly a typical semiconductor surface has a reflectivity of around 0.35 in air, further reducing the light entering the device. Finally, the device is 1.6×10^{-6} m^2 while the incident light is focused to a spot size of 2×10^{-5} m^2, as such only approximately 2.6% of the outputted light is incident on the device. Combining these factors means that the real responsivity is around 20 times higher than the estimates given here. As the key result here is the demonstration of an extended wavelength with minimal degradation to the responsivity rather than the absolute values, the omission of these factors in calculating the responsivity is valid as they will have the same effect on all devices and samples measured. The overall comparison of the responsivity and external quantum efficiency (EQE) has listed in Table 5. 5.

Sample	Responsivity (A/W)			External quantum efficiency		
	1000 nm	1500 nm	2000 nm	1000 nm	1500 nm	2000 nm
GaSb	1.54×10^{-4}	1.64×10^{-4}	1.54×10^{-5}	1.91×10^{-4}	1.36×10^{-4}	9.55×10^{-6}
GaSbBi (2.9%)	6.98×10^{-5}	1.24×10^{-4}	4.47×10^{-5}	8.66×10^{-5}	1.03×10^{-4}	2.77×10^{-5}
GaSbBi (3.8%)	6.98×10^{-6}	3.69×10^{-5}	8.53×10^{-6}	8.66×10^{-6}	3.05×10^{-5}	5.29×10^{-6}
GaSbBi (4.5%)	6.61×10^{-6}	6.14×10^{-6}	4.83×10^{-6}	8.20×10^{-6}	5.08×10^{-6}	2.99×10^{-6}
GaSbN (1.5%)	1.04×10^{-5}	1.56×10^{-5}	3.24×10^{-5}	1.29×10^{-5}	1.29×10^{-5}	2.01×10^{-5}

Table 5. 5 Comparison of devices responsivity and external quantum efficiency at different wavelength

5.3.3 Same material different geometry comparison

In order to study the effect of different geometry on the spectral photo responses, a comparison between the bar and zigzag interdigit fingers have been investigated. Figure 5. 6 show spectral photo response of MSM-PDs devices with different types of geometry. It can be seen that a good agreement of the responsivity measured from different types of the electrode has been obtained. As Figure 5. 6 (a) show the bar and zigzag (from Figure 5. 1) fabricated from the same GaSb wafer, with the same interdigit gap of 100 nm. The 50 nm interdigit gap of bar and zigzag

devices have also been compared for GaSbBi with 3.8% Bi content and GaSbN wafer, as show in Figure 5. 6 (b) and Figure 5. 6 (c), respectively. Small changes of the measured responsivity, indicating that in this work, the effect of the interdigit fingers' shape at the same gap distance is not significant. However, some other research on MSM-PDs structure have suggested the effect of inter-electrode gap distance on the device performance [25, 26].
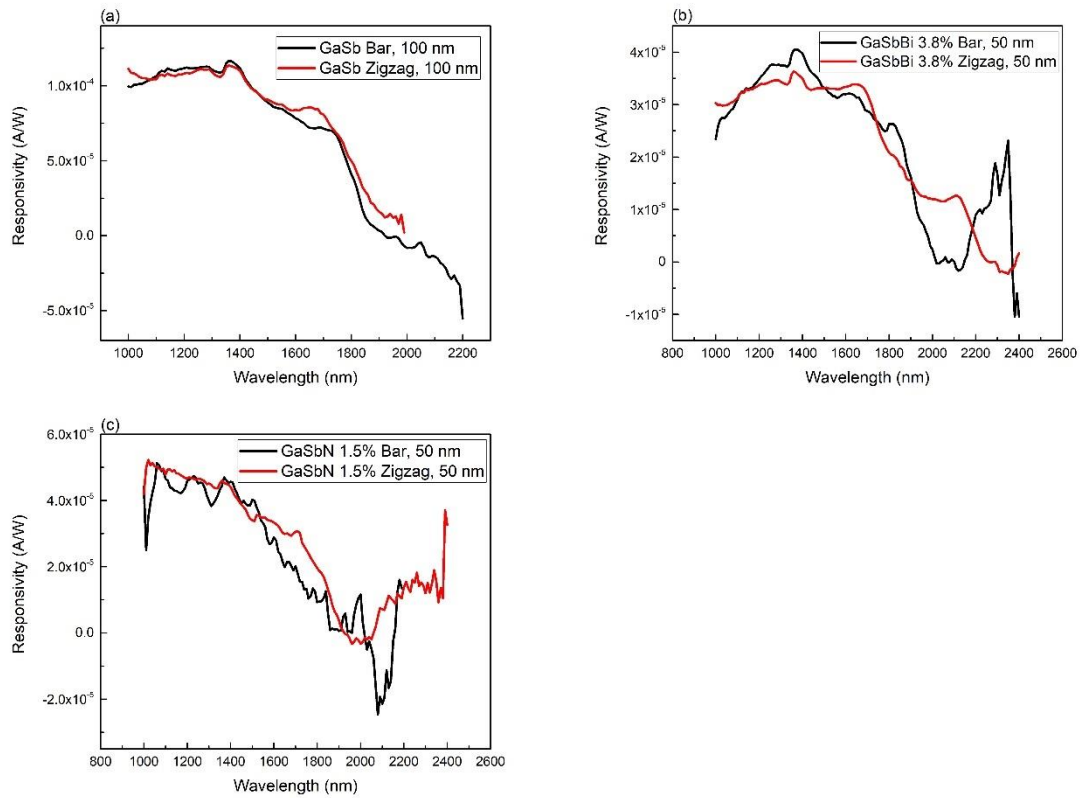
Figure 5. 6 The spectral response of (a) GaSb, (b) GaSbBi and (c) GaSbN MSM-PDs with different geometry of the top electrode
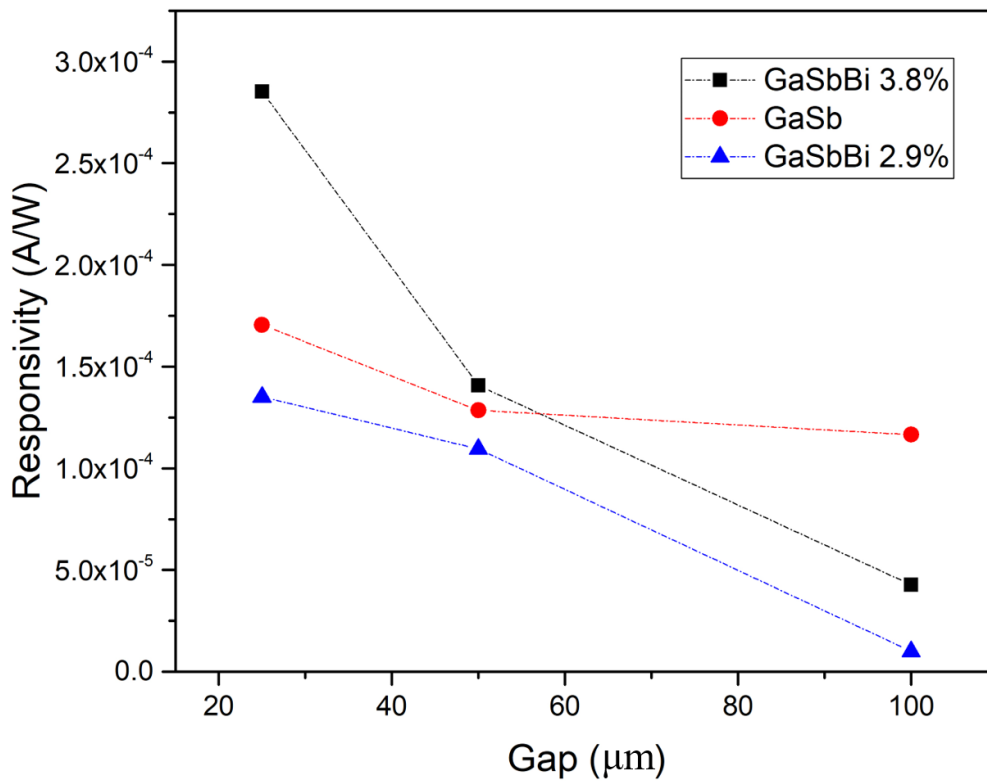
Figure 5. 7 Spectral photo responses of the Interdigit distance dependence of the peak responsivity of bar electrode MSM-PDs

To better understand the effect of the gap distance on spectral photo responses and also to explore the effect of Bi on the optical response of the device, GaSb and GaSbBi MSM-PDs fabricated from bar type electrode with different gap distance has been compared. As shown in Figure 5. 7, the peak responsivity decreases with the gap distance increase. The GaSb MSM-PDs have a relatively constant responsivity as the gap distance is increased, showing a slight reduction from 1.7×10^{-4} A/W at 25 nm gap distance to 1.2×10^{-4} A/W at 100 nm gap distance. However, for the Bi containing samples, a more pronounced decrease can be observed in Figure 5. 7. The GaSbBi devices with Bi incorporation of 2.9% shows a responsivity decrease from 1.3×10^{-4} A/W at 25 nm gap distance to 1.0×10^{-5} A/W at 100 nm gap distance. A similar trend has also been observed for the GaSbBi devices with Bi incorporation at 3.8%, shows an even more significant decrease from 2.8×10^{-4} A/W at 25 nm gap distance to 4.2×10^{-5} A/W at 100 nm gap distance. As mentioned previously the generated photocurrent (and hence responsivity) is affected by both the absorption coefficient and subsequent extraction of the photo generated carriers. For each sample the absorption coefficient will be independent of the gap size used, as such the reduction in responsivity as the gap size increases for the Bi containing samples

108

indicates that the extraction efficiency of the generated carriers decreases as the gap size increases.

These results seem to suggested that the conducting properties of GaSbBi MSM-PDs depended strongly on the gap distance and Bi incorporation. Small gap distance, for the same Bi content devices, is found to exhibit much more responsivity than long gap distance. Meanwhile, the Bi incorporation seems also contribute to the peak responsivity, as the 3.8% Bi device exhibit greater responsivity at all gap distance than the 2.9% Bi devices. This uneven conducting characteristics on GaSbBi devices could due to the extension of lattice constant. Since previous studies on thin film GaSbBi sample, grown via MBE, have suggested that the lattice constant increase while more Bi incorporated into GaSb [27]. The minimum carrier concentration on GaSbBi device may be caused by a relative maximum of lattice constant, which decrease the conducting characteristics. Similar results have also been found in other materials, such as β-Ga_2O_3 [28].

Another potential factor that may reduce the surface photoconductivity include the distribution of Bi droplets on the surface [29]. To better understand this process, extra measurement such as using Ellipsometry to measure the surface states induced by absorption on the semiconductor surface [30] or using surface photovoltage spectroscopy [31], Raman scattering spectroscopy [32] for characterizing metal-semiconductor interface could be applied. However, further studies on the sample is not carried out throughout this thesis due to the shortage resource of wafers and the impact of the COVID-19 restrictions.

It is noticed by the fact from Figure 5. 7 that the responsivity depends on the bandgap and effective masses as a wider bandgap semiconductor material is expected to have smaller responsivity compared to the narrow bandgap semiconductor material. Some of the peak responsivity value in Figure 5. 7 seem does not have good agreement with the fact. While due to the experiment circumstance, the position of the device holder may change for the different measurement. This could lead to a slight difference in power illuminated on the sample. However, the changes seem not to affect the trending of peak responsivity against gap distance and Bi incorporation.

5.4   Conclusion

In this chapter, the viability of incorporating Bi and N into GaSb layers for use as practical photo detectors has been investigated. The cut-off wavelength and responsivity of MSM-PDs

have been investigated. Clear wavelength extensions have been observed for GaSbBi and GaSbN samples, with the cut-off wavelength extended to 1950 nm (2.9% Bi), 1990 nm (3.8% Bi), 2080 nm (4.5% Bi) and 2190 nm (1.5% N) respectively, demonstrating the viability of using Bi and N for mid-infrared sensing. The bandgap reduction for GaSbBi and GaSbN samples, obtained from wavelength extension, has suggested in a range of 26-29 meV/%Bi for GaSbBi and 103 meV/%N for GaSbN devise. While the responsivity and subsequent EQE values extracted for the devices are quite low, these are not directly comparable to current commercial devices due to differences in device design and material maturity. However, the responsivity results indicate that the introduction in Bi or N only results in a modest decrease in the peal responsivity of 23%. As such these materials show great promise for potential future use as infrared photodetectors.

Comparisons of devices with differing gap size between the electrodes indicates that for Bi containing samples the carrier extraction efficiency decreases with increasing gap size. The most likely cause for this is the presence of an increased density of surface defects and traps due to the inclusion of bismuth. As the gap size then increases, there is an increased probability that the carriers encounter one of these traps before arriving at the electrode, reducing the subsequent photocurrent. While the origin of these defects/traps is not clear, the work presented in chapter 4 showed the presence of a number of different defects in "as-grown" GaSbBi, the results in chapter 4 also showed that subsequent annealing resulted in these being repaired and as such may be a possible route to enhance the carrier extraction in these devices.

5.5   Reference

[1]   M. Razeghi and B.-M. Nguyen, "Advances in mid-infrared detection and imaging: a key issues review," *Reports on Progress in Physics,* vol. 77, no. 8, p. 082401, 2014.

[2]   L. S. Rothman *et al.*, "The HITRAN molecular database: editions of 1991 and 1992," *Journal of Quantitative Spectroscopy and Radiative Transfer,* vol. 48, no. 5-6, pp. 469-507, 1992.

[3]   K. Karstad *et al.*, "Detection of mid-IR radiation by sum frequency generation for free space optical communication," *Optics and lasers in engineering,* vol. 43, no. 3-5, pp. 537-544, 2005.

[4]   A. Rogalski, "HgCdTe infrared detector material: history, status and outlook," *Reports on Progress in Physics,* vol. 68, no. 10, p. 2267, 2005.

[5]   W. Lei, J. Antoszewski, and L. Faraone, "Progress, challenges, and opportunities for HgCdTe infrared materials and detectors," *Applied Physics Reviews,* vol. 2, no. 4, p. 041303, 2015.

[6]   P. Jurczak, K. A. Sablon, M. Gutiérrez, H. Liu, and J. Wu, "2.5-µm InGaAs photodiodes grown on GaAs substrates by interfacial misfit array technique," *Infrared Physics & Technology,* vol. 81, pp. 320-324, 2017.

[7]   S. Das, M. Bhowal, and S. Dhar, "Calculation of the band structure, carrier effective mass, and the optical absorption properties of GaSbBi alloys," *Journal of Applied Physics,* vol. 125, no. 7, p. 075705, 2019.

[8]   A. S. Sharma and S. Dhar, "Influence of Bi on the temperature dependent fundamental band gap parameters of GaSb1− xBix," *Materials Research Express,* vol. 6, no. 4, p. 046208, 2019.

[9]   D. Wang *et al.*, "Band edge optical transitions in dilute-nitride GaNSb," *Journal of Applied Physics,* vol. 105, no. 1, p. 014904, 2009.

[10]   L. Yue *et al.*, "Structural and optical properties of GaSbBi/GaSb quantum wells," *Optical Materials Express,* vol. 8, no. 4, pp. 893-900, 2018.

[11]   O. Delorme *et al.*, "GaSbBi/GaSb quantum well laser diodes," *Applied Physics Letters,* vol. 110, no. 22, p. 222106, 2017.

[12]   T. Das, D. Samajdar, M. Bhowal, S. Das, and S. Dhar, "Photoluminescence studies of GaSbBi quantum dots grown on GaAs by liquid phase epitaxy," *Current Applied Physics,* vol. 16, no. 12, pp. 1615-1621, 2016.

[13]   F. Chowdhury, S. Sadaf, Q. Shi, Y.-C. Chen, H. Guo, and Z. Mi, "Optically active dilute-antimonide III-nitride nanostructures for optoelectronic devices," *Applied Physics Letters,* vol. 111, no. 6, p. 061101, 2017.

[14]   M. Rajpalke, W. Linhart, K. Yu, T. S. Jones, M. Ashwin, and T. D. Veal, "Bi flux-dependent MBE growth of GaSbBi alloys," *Journal of Crystal Growth,* vol. 425, pp. 241-244, 2015.

[15]   N. Segercrantz *et al.*, "Increased p-type conductivity in GaN$_x$ Sb$_{1-x}$, experimental and theoretical aspects," *Journal of Applied Physics,* vol. 118, no. 8, p. 085708, 2015.

[16]   S. Adachi, "Optical dispersion relations for GaP, GaAs, GaSb, InP, InAs, InSb, Al x Ga1− x As, and In1− x Ga x As y P1− y," *Journal of Applied Physics,* vol. 66, no. 12, pp. 6030-6040, 1989.

[17]   S. Adachi, "Model dielectric constants of gap, gaas, gasb, inp, inas, and insb," *Physical review B,* vol. 35, no. 14, p. 7454, 1987.

[18]   M. Polak *et al.*, "Theoretical and experimental studies of electronic band structure for GaSb1− xBix in the dilute Bi regime," *Journal of Physics D: Applied Physics,* vol. 47, no. 35, p. 355107, 2014.

[19]   S. Das, T. Das, S. Dhar, M. De La Mare, and A. Krier, "Near infrared photoluminescence observed in dilute GaSbBi alloys grown by liquid phase epitaxy," *Infrared physics & technology,* vol. 55, no. 1, pp. 156-160, 2012.

[20]   D. Samajdar, T. Das, and S. Dhar, "Valence band anticrossing model for GaSb1− xBix and GaP1− xBix using kp method," *Materials Science in Semiconductor Processing,* vol. 40, pp. 539-542, 2015.

[21]   M. K. Rajpalke *et al.*, "High Bi content GaSbBi alloys," *Journal of applied physics,* vol. 116, no. 4, p. 043511, 2014.

[22]   O. Delorme, L. Cerutti, E. Tournié, and J.-B. Rodriguez, "Molecular beam epitaxy and characterization of high Bi content GaSbBi alloys," *Journal of Crystal Growth,* vol. 477, pp. 144-148, 2017.

[23]   T. Veal *et al.*, "Band gap reduction in GaNSb alloys due to the anion mismatch," *Applied Physics Letters,* vol. 87, no. 13, p. 132101, 2005.

[24]   J. Mudd *et al.*, "Optical absorption by dilute GaNSb alloys: Influence of N pair states," *Applied Physics Letters,* vol. 103, no. 4, p. 042110, 2013.

[25]   S. Averine, Y. Chan, and Y. Lam, "Geometry optimization of interdigitated Schottky-barrier metal–semiconductor–metal photodiode structures," *Solid-State Electronics,* vol. 45, no. 3, pp. 441-446, 2001.

[26]   S. Averine, P. Kuznetzov, V. Zhitov, and N. Alkeev, "Solar-blind MSM-photodetectors based on AlxGa1−xN/GaN heterostructures grown by MOCVD," *Solid-State Electronics,* vol. 52, no. 5, pp. 618-624, 2008.

[27]   M. Rajpalke *et al.*, "Growth and properties of GaSbBi alloys," *Applied Physics Letters,* vol. 103, no. 14, p. 142106, 2013.

[28]   E. G. Villora, K. Shimamura, T. Ujiie, and K. Aoki, "Electrical conductivity and lattice expansion of β-Ga 2 O 3 below room temperature," *Applied Physics Letters,* vol. 92, no. 20, p. 202118, 2008.

[29]   L. Brillson, "The structure and properties of metal-semiconductor interfaces," *Surface Science Reports,* vol. 2, no. 2, pp. 123-326, 1982.

[30]   F. Meyer, "Surface-state densities on clean semiconductor surfaces measured by ellipsometry," *Physical Review B,* vol. 9, no. 8, p. 3622, 1974.

[31]   L. Burstein, J. Bregman, and Y. Shapira, "Characterization of interface states at III-V compound semiconductor-metal interfaces," *Journal of applied physics,* vol. 69, no. 4, pp. 2312-2316, 1991.

[32]   W. Ji, B. Zhao, and Y. Ozaki, "Semiconductor materials in analytical applications of surface-enhanced Raman scattering," *Journal of Raman Spectroscopy,* vol. 47, no. 1, pp. 51-58, 2016.

Chapter 6

6. Suppression of surface leakage currents in InAs avalanche photodiodes via sputtering of high-k dielectric layers

6.1 Introduction

The ability to detect mid-infrared light efficiently is increasingly important for a range of applications, such as communications, security, medicine and metrology [1-4]. Currently, most applications operating in this wavelength region utilize Cadmium Mercury Telluride (CMT) [5, 6]. However, CMT is an expensive and challenging semiconductor to grow and fabricate, limiting both the price and quantity of devices, that are available. The other semiconductor-based materials, which have successfully demonstrated as photodetectors operating in the 2 – 3 µm range, include GaAsSb/InGaAs Type-II superlattices [7, 8]. Photodiodes utilizing the bulk semiconductor material InGaAsSb have also been realized over wavelength range [9, 10]. However, the growth and fabrication of this material are still at a very early stage.

Over recent years, InAs has been demonstrated to operate as an excellent avalanche photodiodes (APDs) over this spectral range with single carrier multiplication and low excess noise [11, 12]. This has more recently led to the demonstration of a linear array of InAs APDs [13], as well as single diodes demonstrating room temperature gains in excess of 100 [14] and APDs capable of detecting down to near single photon levels [7]. However, despite these achievements, the commercial uptake and development of InAs based APDs have not yet occurred. One of the primary reasons for this is that the surface passivation of these devices is a nontrivial matter. Mesa etched diodes, fabricated from narrow bandgap semiconductors, are particularly susceptible to surface leakage currents. For InAs, it has been reported that the etched surface of InAs results in electron accumulation which leads to the fermi level being pinned above the conduction band minimum and providing an efficient conduction path [15, 16]. In other compound semiconductor systems (e.g., GaAs and InGaAs), surface passivation techniques applied to block parasitic current paths are typically realized by depositing a layer of dielectric such as silicon nitride over the semiconductor surface [17, 18]. However, such techniques have proved unsuccessful when applied to InAs, most likely due to the small bandgap and the relatively high deposition temperatures required to achieve a high-quality dielectric layer.

This has led to polymer-based dielectrics being utilized in the best performing InAs devices reported to date. However, these polymers are highly sensitive to their deposition conditions

(temperature, relative moisture), making repeatable and reliable manufacture difficult, and these layers can also degrade over time. A further disadvantage of making use of these polymer layers is that while they suppress surface leakage currents at room temperature in moderate-sized diodes (i.e. mesa's with diameters > 100 μm), surface-based currents remain present at low temperatures and in smaller devices [19], limiting the potential size of pixel elements in array-based systems. A final issue with such passivation layers is that they can be difficult to obtain good adhesion for electrical bond pads.

A potential alternative passivation route may be to utilize so-called "high-k" dielectrics to act as the surface passivation layer. High-k dielectric material is a material with a high dielectric constant (relative permittivity) which is a number referring the material's ability act as an insulator and hence a higher value may be expected to lead to improved passivation. It has been widely used in semiconductor manufacturing process where it acts as gate dielectric material for devices. The capacitance created by high-k material is relative to the dielectric constant of the material. This class of dielectrics possess a high dielectric constant, which could provide much greater surface passivation, particularly on narrow bandgap materials. Possible dielectrics such as aluminium oxide (Al_2O_3) and hafnium oxide (HfO_2) are now utilized in the production of CMOS circuits and as such are a well-characterized and understood class of materials [20, 21]. They can also be deposited using a low temperature and high throughput techniques such as atomic layer deposition (ALD) and radio frequency (RF) sputtering. A recent example [22] investigated the passivation of surface contamination on InAs(100) by removing the native oxide using annealing in ultra-high vacuum (UHV) under a flux of atomic hydrogen and growing a stoichiometrically controlled oxide (thermal oxide) in UHV, prior to ALD of an Al_2O_3 high-k layer. Capacitance-voltage measurements confirmed a reduction of the interface trap density compared with an untreated sample, however such work is yet to progress beyond analysing the material interface layer into device applications.

These high-k dielectrics and, in particular, Al_2O_3 have been investigated in recent years for the potential suppression of leakage currents in various III–V semiconductor-based devices [23-27]. For example, He *et al.* [27] have investigated the effect of Al_2O_3 passivation layer on the interface electrical properties of MOS capacitors fabricated using HfTiO as the dielectric on InGaAs. This work resulting in the low leakage current of 1.17×10^{-5} A/cm^2 at an applied gate voltage of 1 V. There have also been a handful of studies on utilizing these passivation layers on other narrow bandgap photodetectors, such as type-II superlattices [28, 29]; however, to date, there are no reports of high-k-based dielectrics being used in the passivation of InAs

117

photodetectors. In this chapter, a systematic investigation of the use of sputtering different dielectric layers as potential passivation layers for InAs APDs has been investigated. By utilizing the same device structure and deposition technique for the passivation layer, the direct comparisons in terms of the effect of different dielectric layers on suppressing surface leakage currents has been presented.

6.2   Experimental detail

The epitaxial wafer was grown by the National Epitaxy Facility at University of Sheffield via metal organic chemical vapour deposition (MOCVD) on a 2'' n-doped InAs substrate. The epitaxial structure consisted of a 1.5-μm n^+-doped InAs (1×10^{18} cm^{-3} of Si) layer followed by 4 μm of nominally undoped InAs and then a 3.5-μm p-doped layer (with a linearly graded doping profile extending from 1×10^{16} to 1×10^{18} cm^{-3} of Zn), which was then capped with a 0.5-μm p^+-doped layer (1×10^{18} cm^{-3} of Zn).

The wafer was then fabricated into circular mesa diodes (with radii ranging from 50 to 600 μm) using a standard mask lithography process, same photo lithography mask as shown in Figure 4.1 has been used in this chapter. The wafer was then etched using preferred chemical etching procedures for InAs of a 1:1:1 (phosphoric acid: hydrogen peroxide: deionized water) etch, followed by a finishing etch of 1:8:80 (sulfuric acid: hydrogen peroxide: deionized water) [11, 12]. The cross-section schematic of InAs APDs is shown in Figure 6. 1. The wafer was then cleaved into a series of approximately 2 cm × 2 cm pieces for passivation. For the deposition of high-k layers, the samples were placed into a Moorfield NanoPVD RF Sputter system, and in total, four different dielectric layers were deposited: zirconium oxide (ZrO_2), zinc oxide (ZnO), aluminium oxide (Al_2O_3), and magnesium oxide (MgO).
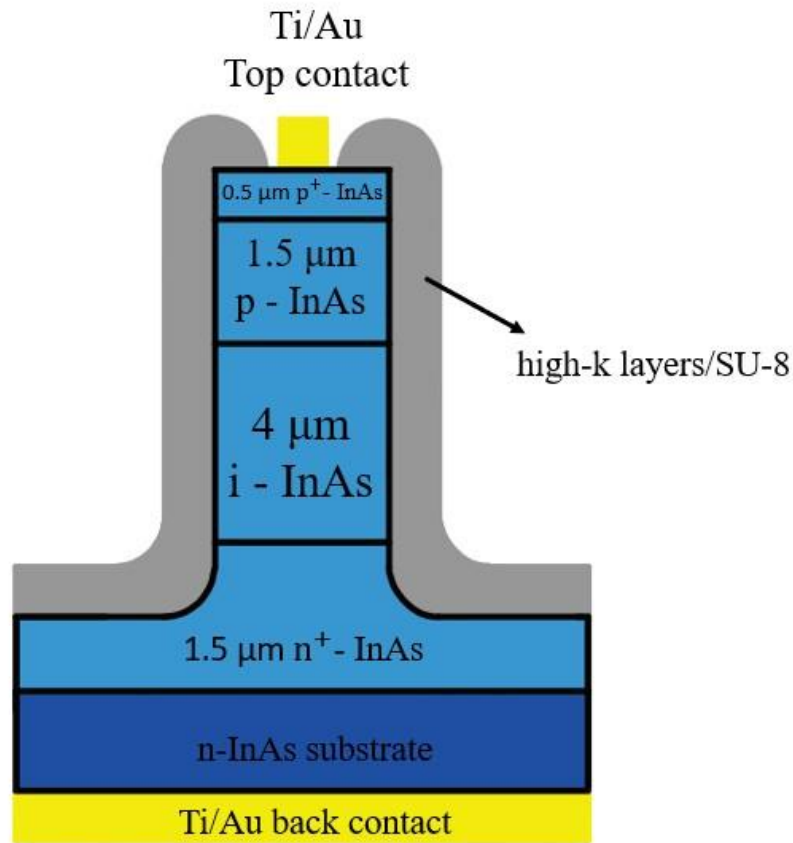
Figure 6. 1. Cross-section schematic of passivated InAs APDs

To determine the optimum deposition conditions for each dielectric, a series of initial layers were deposited for each material on planar InAs substrates and cleaned glass under different deposition conditions (RF power, argon flow rate, and deposition temperature). The sheet resistivity was measured for each layer using a transmission line measurement technique, and the conditions resulting in the highest resistance were determined to be optimum.

The selected optimum conditions were then utilized to deposit the dielectric passivation layers onto the etched mesa diodes, and the sheet resistance was measured via the transmission line method. The details of the deposited conditions are shown in Table 6. 2. After dielectric deposition, the samples were patterned utilizing standard lithography, and an appropriate wet etch was used to remove the dielectric from the electrical contacts and optical window of the device. A reference sample was also realized by passivating one of the samples with SU8, using standard literature-based procedures [12].

Current-voltage (IV) measurements were performed by an Agilent Technology B1500A Semiconductor Device Analyzer with a current compliance limit of 5 mA. At room temperature, the devices were directly probed via a probe station, whereas, for temperature-dependent measurements, the samples were mounted onto proper headers and gold wire bonded, before being placed into a liquid nitrogen-cooled cryostat.

6.3   Sheet resistance

To understand the passivation properties of different high-k dielectric materials, a group of metal oxide were deposited first on both glass and planar InAs wafer with a thickness of 25nm and 50nm via RF sputtering under the same condition. The sheet resistance was measured by the transmission line method and listed in Table 6. 1. It can be seen from the table that 50 nm MgO and ZrO_2 has the most and secondary resistive characteristics when deposited on InAs with $8.77 \pm 0.4 \times 10^{12}$ $\Omega/\square$ and $1.77 \pm 0.2 \times 10^{12}$ $\Omega/\square$, respectively, whereas, the 50nm Al_2O_3 deposited on InAs have the lowest sheet resistance of $7.47 \pm 0.5 \times 10^{10}\Omega/\square$, similar resistance trending can also be found in the sheet resistance value on the glass. Indicating from the table that MgO has the most resistive characteristics while Al_2O_3 has the lowest when depositing on the glass substrate. It is noticed that the sheet resistance value for the high-k material deposited on the glass is generally greater than those resistance values on the InAs substrate. The sheet resistance value vary on the different substrate could indicate that part of the current passes through the high-k dielectric layer and conducting on the surface of the InAs since these high-k dielectric materials were conductive under the particular circumstance. The contact spreads have not been observed as most sheet resistance value for each material are in the same magnitude. It seems like the sheet resistance is not depend on the thickness of thin film since most sheet resistance value is close; however, the resistivity of the film will play an important role in supressing leakage current, therefore 50 nm thin film will be applied and discussed in the following content. In this chapter, the research is focusing on the resistive properties of different high-k dielectric materials on InAs photodiodes under the same condition.

Table 6. 1. The overall sheet resistance of different high-k dielectric materials on glass and planar InAs substrate

	Deposited on glass		Deposited on InAs	
	25nm ($\Omega/\square$)	50nm ($\Omega/\square$)	25nm ($\Omega/\square$)	50nm ($\Omega/\square$)
Al_2O_3	$8.14 \pm 1.8 \times 10^{15}$	$4.73 \pm 0.4 \times 10^{15}$	$6.18 \pm 0.6 \times 10^{10}$	$7.47 \pm 0.5 \times 10^{10}$

MgO	$2.94 \pm 0.6 \times 10^{16}$	$3.69 \pm 0.3 \times 10^{16}$	$4.04 \pm 0.8 \times 10^{12}$	$8.77 \pm 1.4 \times 10^{12}$
ZnO	$6.14 \pm 0.5 \times 10^{15}$	$9.89 \pm 1.6 \times 10^{15}$	$2.69 \pm 0.5 \times 10^{11}$	$2.8 \pm 0.4 \times 10^{11}$
ZrO$_2$	$1.5 \pm 0.4 \times 10^{16}$	$1.91 \pm 0.2 \times 10^{16}$	$2.26 \pm 0.7 \times 10^{12}$	$1.77 \pm 0.2 \times 10^{12}$

Most studies have done by many different groups indicated various resistance values, Nowicki et al. [30] had studied the 190 nm Al$_2$O$_3$ on Si substrate with the film resistivity value around $1 \times 10^7 \Omega \cdot cm$. Carcia et al. [31] and Asadov et al. [32] have deposited ZnO thin film via RF sputtering and DC sputtering with the resistivity values between $6.5 \times 10^4 \Omega \cdot cm$ and $9.7 \times 10^5 \Omega \cdot cm$. Singh et al. [33] have deposited ultrathin films of MgO on Si substrate using dual ion beam sputtering in different partial pressures of oxygen. The result indicates a $1.5 \times 10^7 \Omega$ resistance value with a thickness of 6 nm MgO. These values make it very difficult to compare how effective different passivation methods are since different fabrication recipes are used. In this chapter, the result of the RF sputtering passivation techniques which processed under the same conditions and the same fabrication process have been compared. The optimised conditions used to deposit the high-k materials on etched mesa diodes are listed in Table 6. 2. Similar trending of the sheet resistance has also been observed compare to the result on planar InAs substrate (as shown in Table 6. 1). It can be seen from the Table 6. 2 that MgO has the most sheet resistance value at around $6.3 \pm 0.6 \times 10^{12} \, \Omega/\square$ among the group of materials, while Al$_2$O$_3$ at bottom of the list has $3.5 \pm 0.7 \times 10^{10} \, \Omega/\square$.

Table 6. 2. Deposited high-k dielectric layers and their associated deposition conditions on etched InAs mesa diode

Dielectric Material	Layer Thickness (nm)	Deposition Temperature (°C)	RF Power (W)	Argon Flow (sccm)	Sheet Resistance ($\Omega/\square$)
ZnO	50	25	45	3	$3.2 \pm 0.6 \times 10^{11}$
Al$_2$O$_3$	50	25	45	0.5	$3.5 \pm 0.7 \times 10^{10}$

MgO	50	25	45	0.5	$6.3 \pm 0.6 \times 10^{12}$
ZrO₂	50	25	60	3	$1.6 \pm 0.4 \times 10^{12}$

6.4 Scanning electron microscope

To further investigate the uniformity of the passivation layer, the extra SEM and EDX map measurements were performed on the group of the passivated samples by using a JEOL JSM-6610 scanning electron microscope.

Figure 6. 2 shows the 60º top angle image of InAs APDs with different dielectric layers. It can be seen from

Figure 6. 2 (a) that the uniformity layers are founded for Al_2O_3 and ZrO_2 deposited on InAs APDs, the layers are cover all the tiny undulation on the mesa sidewall. However, some apparent bubble dilation can be observed from MgO deposited InAs APDs, as shown in

Figure 6. 2 (b), which indicate that an inhomogeneous MgO layer is formed during the sputtering. A similar result has also been found for ZnO layer, that some apparent cracks can be observed at the edge of the mesa diode. This thin film cracking could be due to the partial thermal mismatch between the ZnO film and substrate [34].

To look into these high-k layers, energy dispersive x-ray (EDX) maps analysis of the InAs APDs passivated by high-k dielectric material has presented in Figure 6. 3. It revealed distinct patterns in element distributing across the surface of the sample. Figure 6. 3. (a) show the elements map of the sample passivated by ZnO. The localization of Zn and O on the surface of the sample is evenly distributed, leaving a window for the top electrical contact without passivation. A similar result has also been found for the other sample in Figure 6. 3.(b), Figure 6. 3.(c) and Figure 6. 3.(d), that O element is evenly distributed on the surface. However, some distinct element, Mg and Zr has been identified on top of the gold electrical contact in Figure 6. 3.(c) and Figure 6. 3.(d). This element disturbing could imply that the etching process used in this experiment has not sufficiently removed the passivation layer. However, the O element in Figure 6. 3.(c) and Figure 6. 3.(d) has suggested a distinct window for top electrical contact.

Meanwhile, the high-k materials target used for the sputtering process also has more than 98% purity. It is less likely that the etching process can largely break the chemical bond between

metal and oxygen. The possible explanations for the distribution of Mg and Zr are the EDX measurement error because of the similar element weight [35]. EDX is undoubtedly not a sufficiently surface chemical analysis technique. However, the result in this experiment is enough to support that etching process has removed the high-k material on top of the electrode and the electrical characteristics will not be affected by the high-k material on top of electrical contact.

(a)

(b)

SEI   20kV   WD40mm   SS53   x300   50μm
                          ICaL   0023   17 Dec 2019
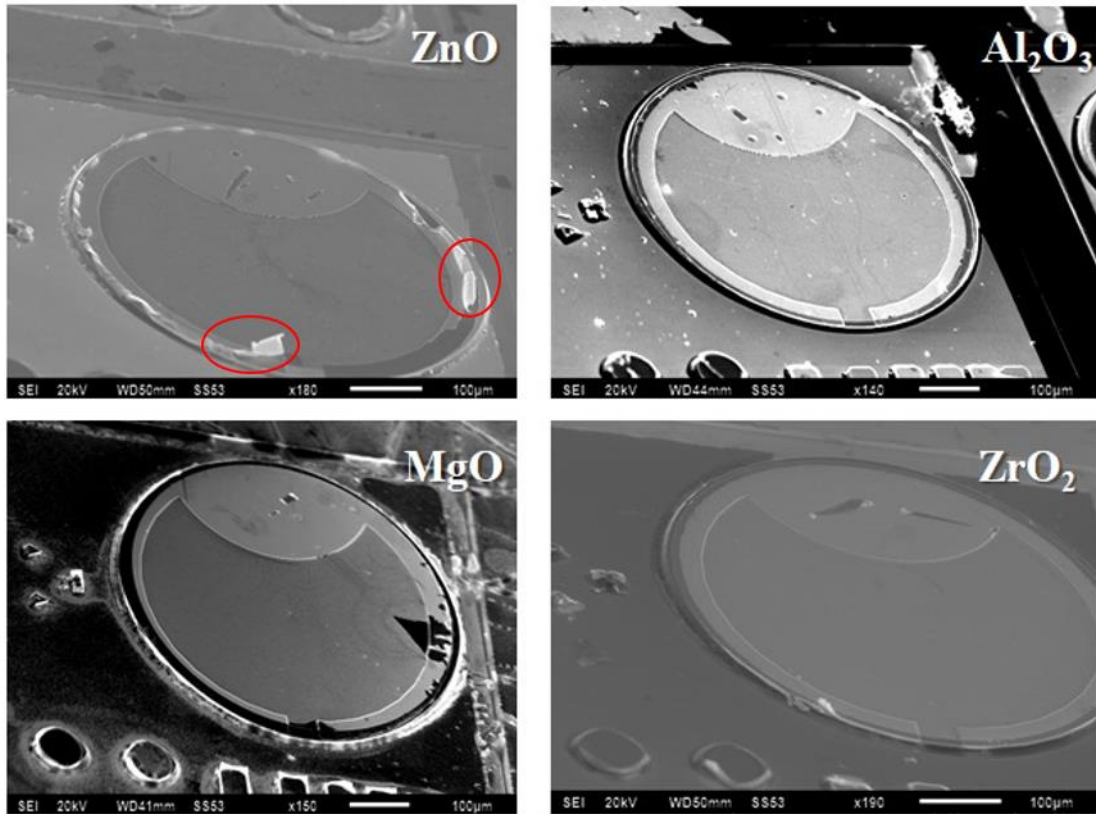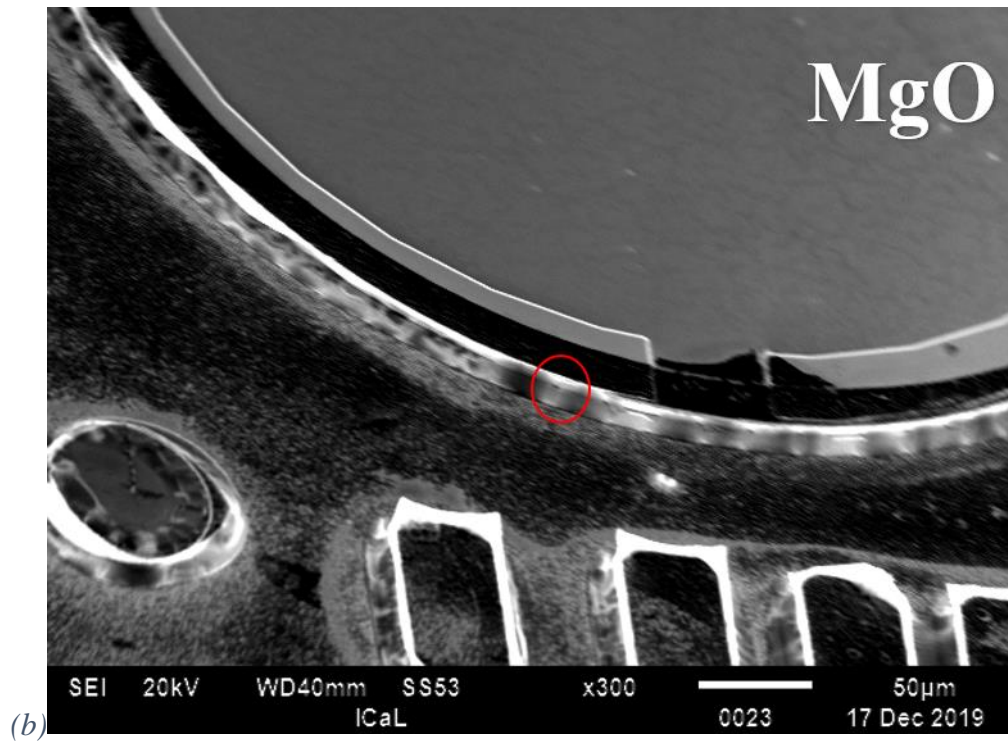
Figure 6. 2. SEM top images for InAs APDs with radius of 600 μm, (a) passivated with different dielectric layers and (b) passivated with MgO in a high resolution.

Electron Image 1   O Ka1   Zn Ka1

As Ka1   Au La1   In La1

(a)

(b)

Electron Image 1 | O Ka1 | Al Ka1
As Ka1 | Au La1 | In La1

(c)

Electron Image 1 | O Ka1 | Mg Ka1_2
In La1 | As Ka1 | Au La1

(d)

Electron Image 1 | O Ka1 | Zr La1
As Ka1 | Au La1 | In La1
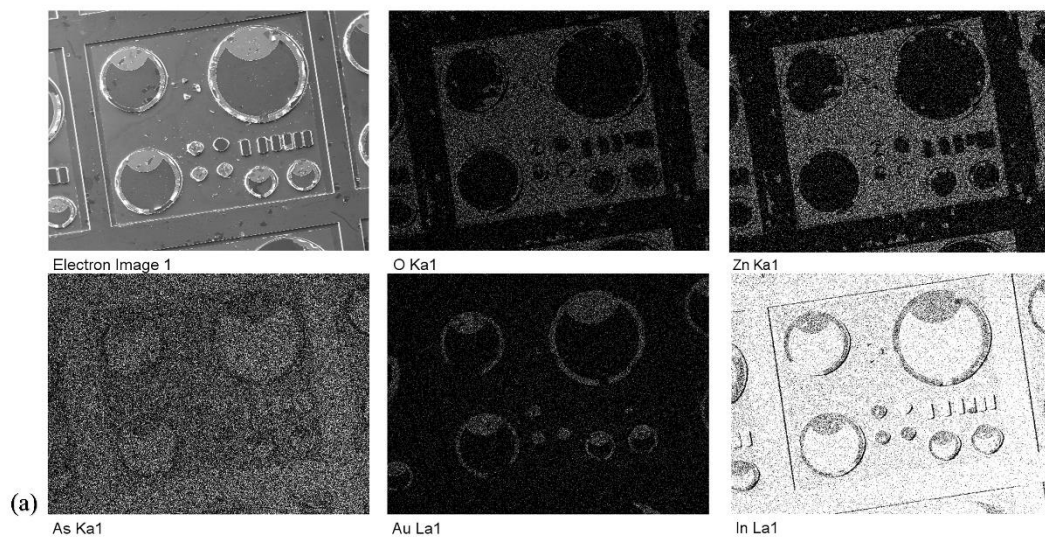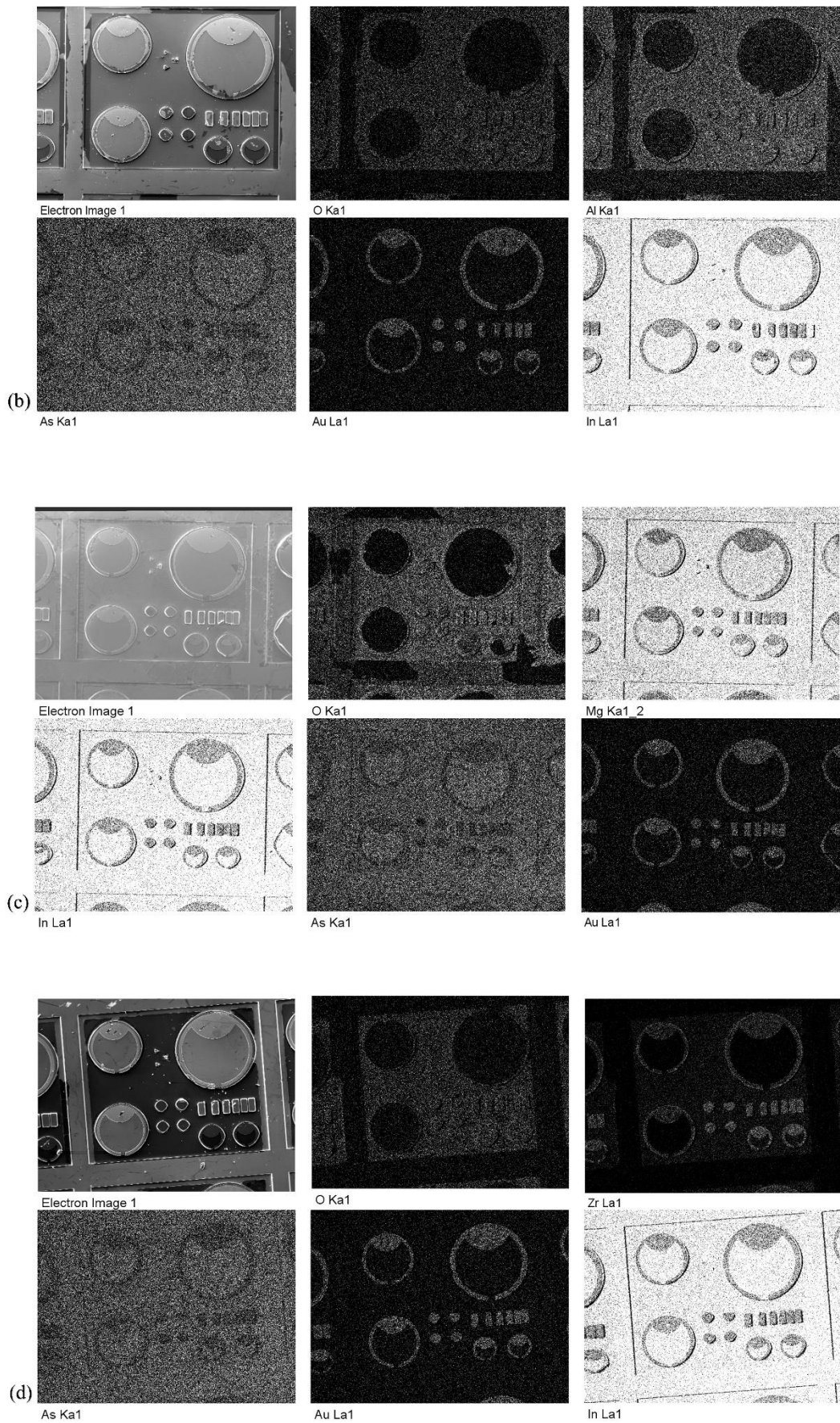
Figure 6. 3. SEM & EDX elements map of InAs APDs passivated with (a) ZnO, (b) Al2O3, (c) MgO and (d) ZrO2.

125

6.5   Room temperature current-voltage measurement

The room temperature current density versus voltage (JV) curves for differently sized mesa diodes is shown for all passivation materials in Figure 6. 4. The reference device (passivated with SU8) shows good agreement between the larger sized diodes; however, as the radius of the mesas is reduced, the current density increases, indicating the presence of significant surface leakage currents in these devices.

The samples passivated with ZnO, Al_2O_3, and MgO exhibit excellent agreement between different sized mesas, even down to the smallest radius used in the chapter (50 μm). This agreement indicates that each of these dielectric layers provides sufficient passivation to suppress any measurable surface leakage currents at room temperature. The ZrO_2 has much poorer performance than the other three high-k dielectrics used, as shown in Figure 6. 4. The resultant devices exhibit a rapid rise in current as the reverse bias is applied, indicating near short-circuit behaviour. The reasons for this are not immediately clear; however, the deposition of this layer does require significantly higher RF power, as shown in Table 6. 2, than the other dielectrics. One possible cause of the degradation in performance is due to this higher power causing significant surface damage to the InAs as the ZrO_2 is initially deposited.
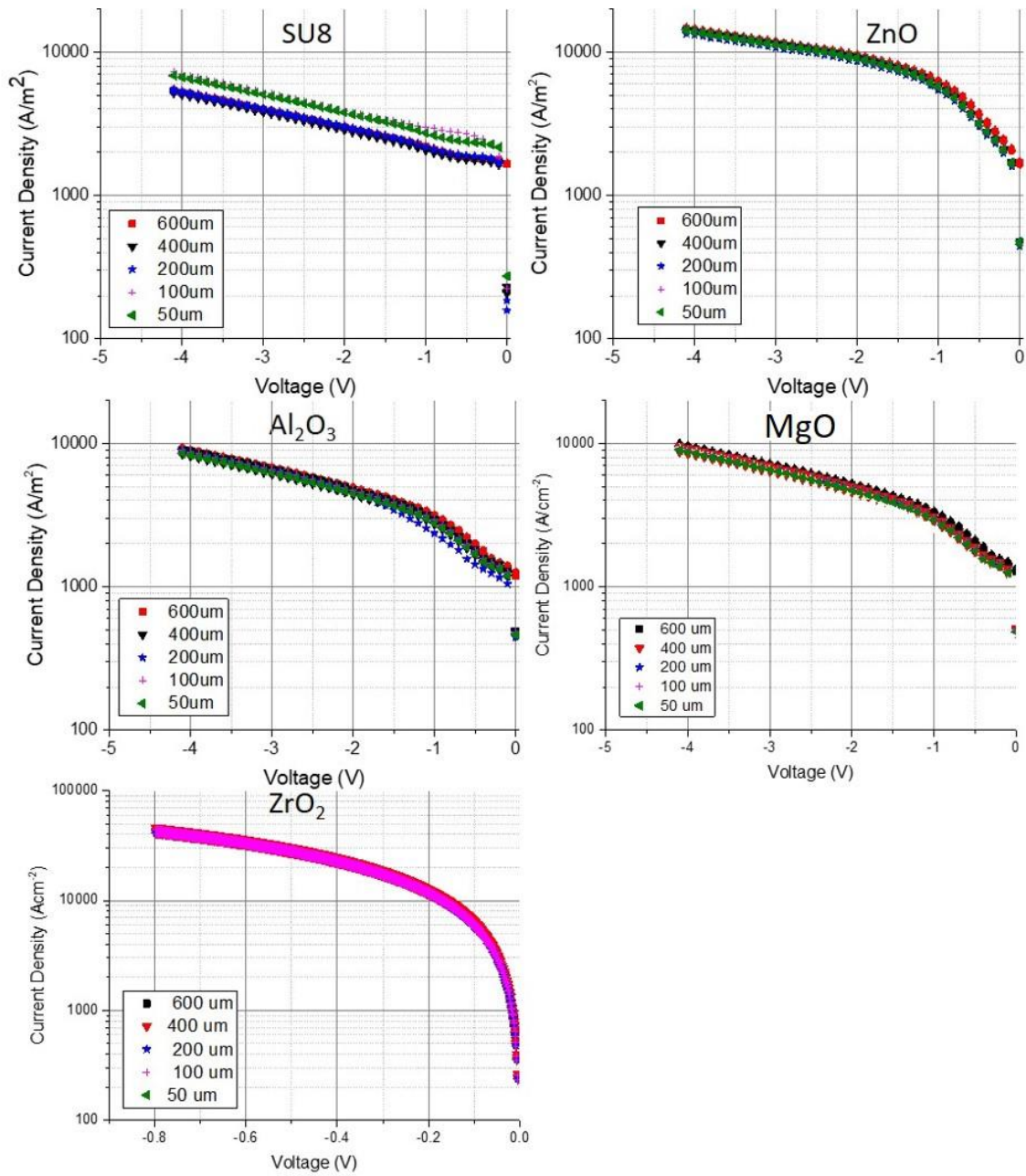
Figure 6. 4. Room temperature current voltage (JV) curves for InAs APDs of varying sized radius, passivated with different dielectric layers.

6.6 Temperature dependence current voltage measurement

To further evaluate the passivation properties of these different layers, temperature-dependent I–V measurements were undertaken for the ZnO, Al_2O_3, and MgO samples. Due to poor room temperature performance, the ZrO_2 sample has been discounted for any further investigation in this work. For each passivation layer, diodes with radii of 600, 200, and 100 μm have been measured as a function of temperature to enable the current density to be compared for each.

The resultant curves for all samples at various temperatures are shown in Figure 6. 5. For the SU8 passivated sample, as the temperature is decreased, there is an increasing divergence in the performance of differently sized devices, indicating the increase of non-bulk leakage current mechanisms as the temperature is decreased. This result indicates that as the temperature is decreased, surface leakage currents become more dominant.

On the contrary, for the three high-k passivated samples, a much better agreement can be seen for all samples and at all temperatures. This agreement indicates that these layers can provide much better suppression of surface leakage currents, even at low temperatures, with only a slight deviation in current densities occurring at high voltages and the lowest temperatures.
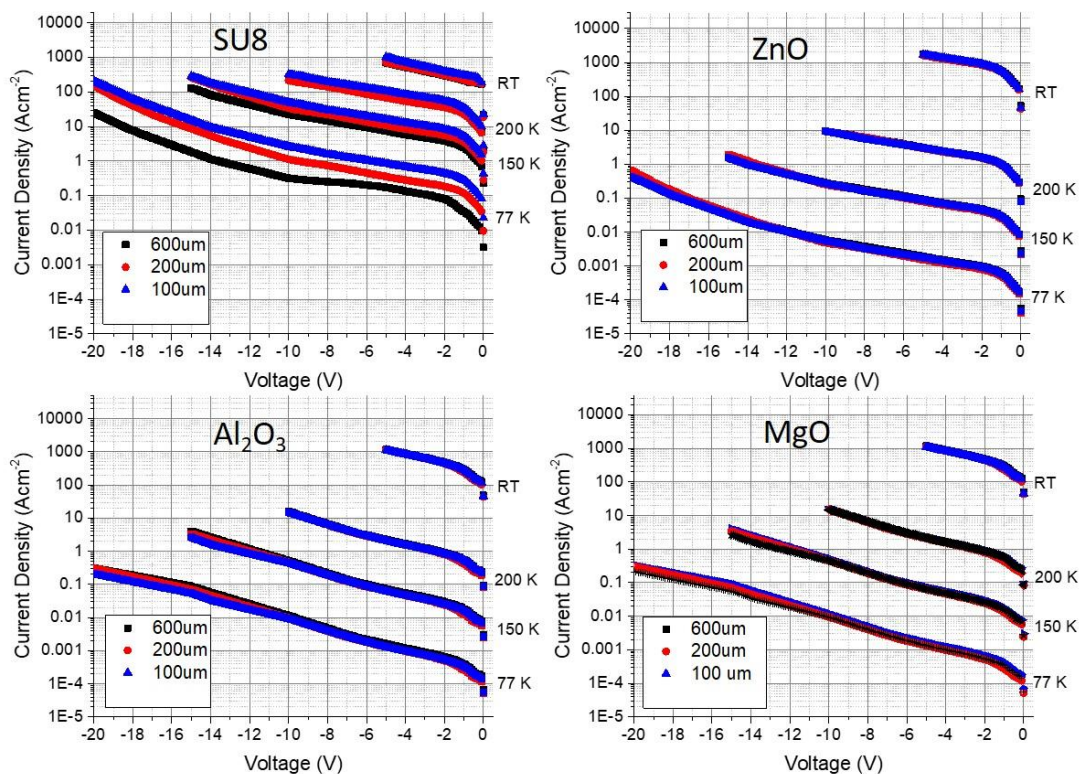
Figure 6. 5. Temperature dependent JV curves for InAs APDs, passivated with different dielectric layers

To further investigate the temperature dependence of these leakage currents, an Arrhenius analysis has been applied. Figure 6. 6 shows the dark current density for devices with a radius of 200 μm at an applied reverse bias of 0.2 V, plotted against 1000/T, where T is the temperature.

In Figure 6. 6, a clear difference between the SU8 passivated sample and the high-k passivated samples can be seen across all temperatures. There is an initial decrease in the current for the

reference SU8 sample as the temperature is initially decreased, however by ~ 250K this decrease becomes much more gradual an exhibits almost the same dark current at all other temperatures. All four high-k passivated samples show almost identical behaviour. There appear to be two distinct temperature regimes, the first occurs at high temperatures between ~300 and 175 K, over which a sharp decrease in the current is observed as the temperature is decreased. As the temperature is further decreased below 175 K, the dark current continues to decrease, however this is now at a slower rate. Note even in this 2nd regime the decrease in current is much more appreciable than that which was observed for the reference SU8 sample.

Despite the reduced dark currents for the samples passivated with high-k layers, there are still two distinct slopes and regimes in the Arrhenius plots. A sharp reduction in the dark current as a function of decreasing temperature occurs between room temperature and at approximately 175 K, after which a much slower reduction of the dark current takes place for further reductions in the temperature. This seems to imply that the dark current is still not dominated by bulk effects over the entire temperature range and that surface currents are still present.

If the dark current was (bulk) dominated by the diffusion of carriers from the cladding layers [36], then the observed current would be expected to follow a simple relationship given by:

$$J = Cexp(\frac{-E_A}{kT})$$

(6- 1)

where C is a fitting constant, and E_A is the activation energy, which has set to 0.36 eV (the bandgap of InAs) [37]. The resultant fit is shown in the dashed line of Figure 6. 6, and it shows an excellent agreement with the experimental data, for the samples passivated with high-k layers, over the higher temperature region between 300 and 175 K, proving that over this region the devices are bulk current dominated. As expected, the fit then gives poorer agreement in the lower temperature region, signifying the onset of surface leakage currents, where generation and recombination of carriers at the surface of the mesa begin to dominate.

This analysis confirms that the presence of surface leakage current is suppressed by high-k passivation at high temperature; however, even for the high-k passivated samples, there are still appreciable (although less compared to the reference SU8 sample) surface leakage currents at lower temperatures. While somewhat masked by the large range of currents plotted, these surface leakage currents are also detectable in Figure 6. 5, for the high-k passivated sampled. In Figure 6. 5 there are deviations in the current densities for the differently sized devices which can be observed at higher voltages, indicating the presence of surface currents. While the

currents at lower voltages appear to show a better agreement, this is due to the scale of the plots, masking these slight discrepencies.

These results show that a variety of high-k dielectric layers can be deposited via sputtering and act as passivation layers with superior performance compared to more standard polymer-based passivation layers.
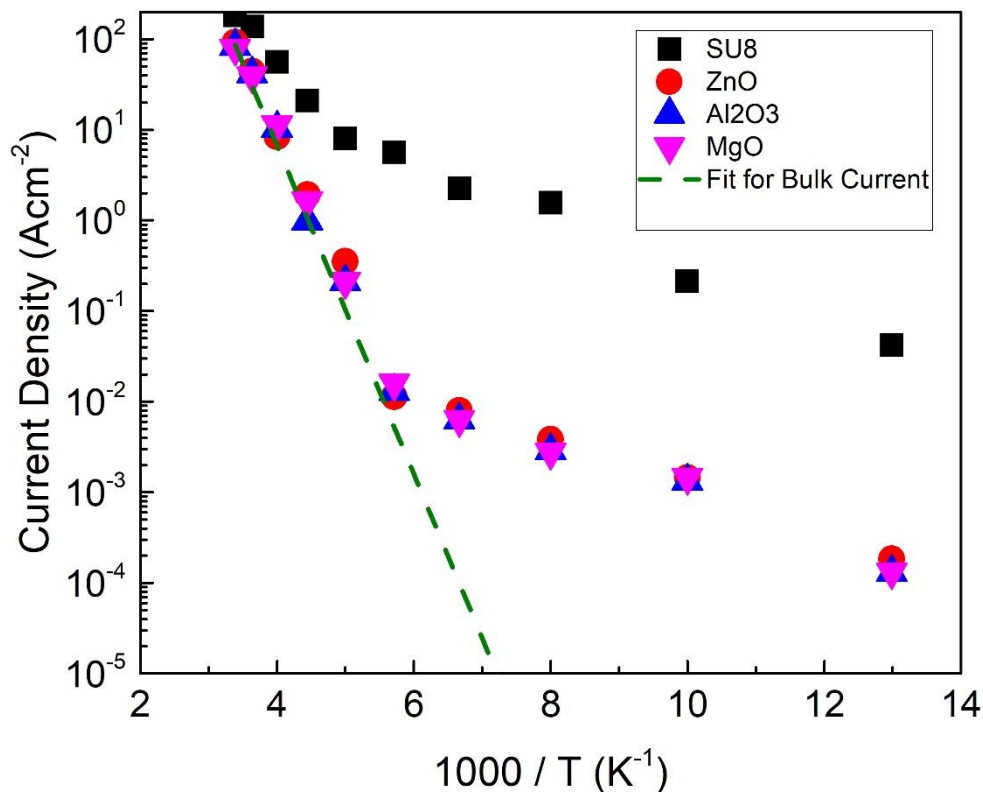
Figure 6. 6. Comparison of temperature dependent dark current density for devices with a radius of 200 μm at a reverse bias of 0.2 V, for different passivation layers.

Another potential drawback from utilizing polymer-based passivation layers is that due to the mismatch in the thermal properties of the polymer layers and the underlying semiconductor layers after repeated temperature cycling, the performance of the device begins to degrade. The most likely cause of such degradation is the difference in thermal expansion and contraction of the InAs and SU8 (4.5×10^{-6} and 1.0×10^{-4} K^{-1}, respectively) causing the SU8 to deform and crack and, hence, degrading the passivation properties of the layer. A secondary potential advantage of utilizing high-k-based passivation layers is improved temperature robustness, due to a lower mismatch in the thermal properties of these layers. ZnO. Al_2O_3 and MgO exhibit the coefficients of expansion of 4.8×10^{-5} [38], 1.4×10^{-5} [39], and 1.1×10^{-5} K^{-1} [40], respectively.

To investigate the thermal robustness of these passivation layers, the thermal cycling tests have performed on each sample. For this, the room temperature I–V characteristics was measured and then cooled the sample to a temperature of 77 K at a rate of approximately 5 K/min; the devices are then held at this temperature for 15 min before being heated back to room temperature at the same rate. The room temperature I–V characteristics are then measured again before another temperature cycle takes place; up to ten temperature cycles were undertaken for each sample. The resultant I–V plots for devices with a radius of 200 μm, taken between temperature cycling runs, are shown in Figure 6. 7.

In Figure 6. 7, it can be seen that for the reference SU8 passivated sample, after one temperature cycle, there is a significant degradation in the electrical performance of the device. After a second temperature cycle, the device has undergone significant further degradation and is exhibiting near short circuit behaviour. For all of the high-k passivated samples, a significant reduction in the degradation after each temperature cycle is observed, with good performance still be maintained even after ten temperature cycles. For the ZnO passivated sample, no observable difference in the I–V characteristics occurs after a single temperature cycle; however, after ten such cycles, an increased current is observed at the highest voltages suggesting some degradation in the layer and onset of some surface leakage current, particularly at higher bias. For the Al_2O_3 passivated sample, no degradation in performance is observed even after ten temperature cycles. The MgO sample shows a very slight degradation in performance after each temperature cycling, resulting in almost a 10% higher current at a constant voltage after ten temperature cycles.

These results indicate that all of the high-k layers exhibit improved temperature robustness compared to the more standard SU8 passivation technique, with the best performance being obtained for the sample passivated with Al_2O_3. As previously noted, Al_2O_3 has the closest coefficient of thermal expansion to InAs, which could be the reason for its excellent behaviour under repeated thermal stress.
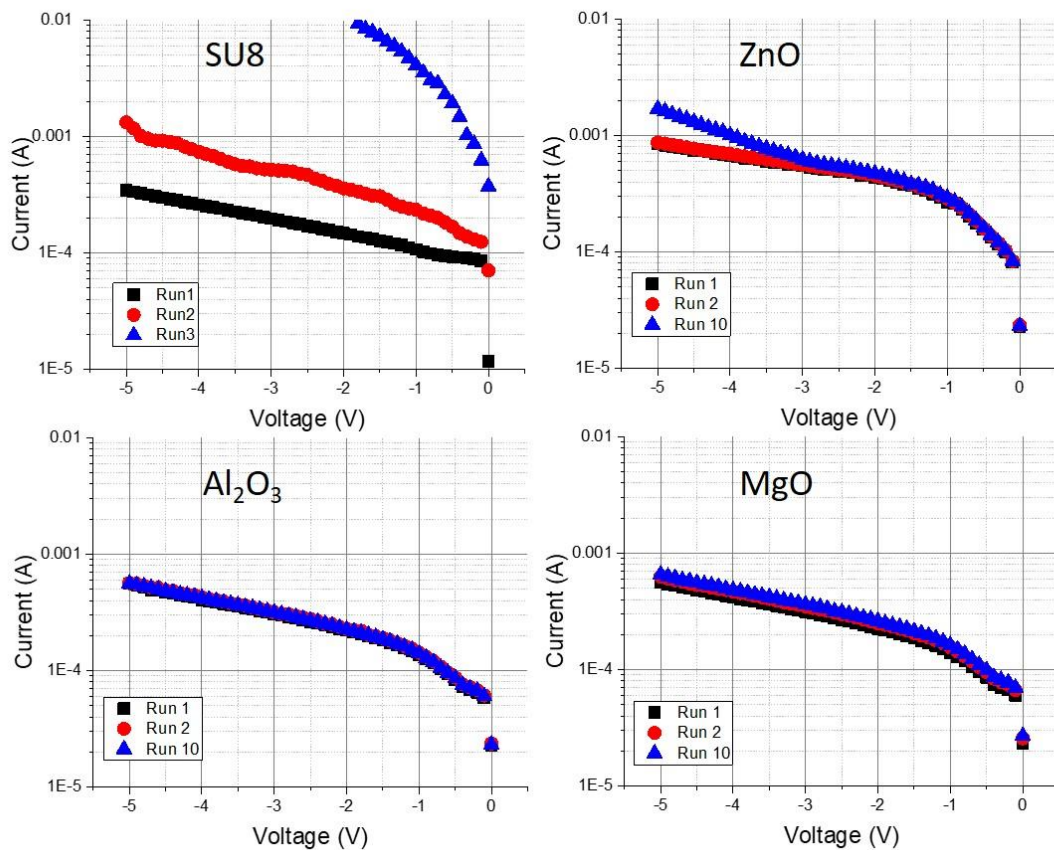
Figure 6. 7. Room temperature I-V characteristics of InAs APDs passivated with different layers, taken between different temperature cycles.

6.7 Conclusion

In this chapter, the effect of four alternative high-k dielectric layers as potential passivation layers for InAs avalanche photodiodes has been investigated. Three potential passivation layers, including ZnO, Al_2O_3 and MgO have been identified, all of which enables the suppression of surface leakage in smaller sized InAs APDs with a radius of 50 μm and at lower temperatures of 175 K compared to a reference SU8 device. The influence of repeated temperature cycling on these layers has also been investigated with Al_2O_3 passivated device, exhibiting no change in performance after temperature cycles.

6.8 Reference

[1]   M. Achour, "Free-space optics wavelength selection: 10 µm versus shorter wavelengths," *Journal of Optical Networking,* vol. 2, no. 6, pp. 127-143, 2003.

[2]   H. Gao, A. Krier, V. Sherstnev, and Y. Yakovlev, "InAsSb/InAsSbP light emitting diodes for the detection of CO and CO2 at room temperature," *Journal of Physics D: Applied Physics,* vol. 32, no. 15, p. 1768, 1999.

[3]   A. Krier, H. Gao, and Y. Mao, "A room temperature photovoltaic detector for the mid-infrared (1.8-3.4 m) wavelength region," *Semiconductor science and technology,* vol. 13, no. 8, p. 950, 1998.

[4]   I. M. Baker, S. S. Duncan, and J. W. Copley, "A low-noise laser-gated imaging system for long-range target identification," in *Infrared Technology and Applications XXX*, 2004, vol. 5406: International Society for Optics and Photonics, pp. 133-144.

[5]   S. Ghosh *et al.*, "Low-noise mid-wavelength infrared avalanche photodiodes," *Journal of electronic materials,* vol. 37, no. 12, pp. 1764-1769, 2008.

[6]   J. Beck *et al.*, "The HgCdTe electron avalanche photodiode," *Journal of electronic materials,* vol. 35, no. 6, pp. 1166-1173, 2006.

[7]   C. H. Tan, A. Velichko, L. W. Lim, and J. S. Ng, "Few-photon detection using InAs avalanche photodiodes," *Optics express,* vol. 27, no. 4, pp. 5835-5842, 2019.

[8]   D. S. Ong, J. S. Ng, Y. L. Goh, C. H. Tan, S. Zhang, and J. P. David, "InAlAs Avalanche Photodiode With Type-II Superlattice Absorber for Detection Beyond 2$\mu\hbox {m} $," *IEEE Transactions on Electron Devices,* vol. 58, no. 2, pp. 486-489, 2010.

[9]   G. R. Savich *et al.*, "III-V semiconductor extended short-wave infrared detectors," *Journal of Vacuum Science & Technology B, Nanotechnology and*

Microelectronics: Materials, Processing, Measurement, and Phenomena, vol. 35, no. 2, p. 02B105, 2017.

[10]　T. Nguyen, J. Kim, Y. Kim, E. Kim, Q. Nguyen, and S. Lee, "Dual-color short-wavelength infrared photodetector based on InGaAsSb/GaSb heterostructure," *AIP Advances,* vol. 8, no. 2, p. 025015, 2018.

[11]　A. Marshall, C. Tan, M. Steer, and J. David, "Electron dominated impact ionization and avalanche gain characteristics in InAs photodiodes," *Applied Physics Letters,* vol. 93, no. 11, p. 111107, 2008.

[12]　A. R. J. Marshall, P. Vines, P. J. Ker, J. P. David, and C. H. Tan, "Avalanche multiplication and excess noise in InAs electron avalanche photodiodes at 77 K," *IEEE Journal of Quantum Electronics,* vol. 47, no. 6, pp. 858-864, 2011.

[13]　I. C. Sandall, S. Zhang, and C. H. Tan, "Linear array of InAs APDs operating at 2 μm," *Optics express,* vol. 21, no. 22, pp. 25780-25787, 2013.

[14]　W. Sun, S. J. Maddox, S. R. Bank, and J. C. Campbell, "Record high gain from InAs avalanche photodiodes at room temperature," in *72nd Device Research Conference*, 2014: IEEE, pp. 47-48.

[15]　D. á. Tsui, "Observation of surface bound state and two-dimensional energy band by electron tunneling," *Physical Review Letters,* vol. 24, no. 7, p. 303, 1970.

[16]　L. Piper, T. Veal, M. Lowe, and C. McConville, "Electron depletion at InAs free surfaces: Doping-induced acceptorlike gap states," *Physical Review B,* vol. 73, no. 19, p. 195321, 2006.

[17] A. Jaouad and V. Aimez, "Passivation of air-exposed AlGaAs using low frequency plasma-enhanced chemical vapor deposition of silicon nitride," *Applied physics letters,* vol. 89, no. 9, p. 092125, 2006.

[18] A. Jaouad, V. Aimez, and C. Aktik, "GaAs passivation by low-frequency plasma-enhanced chemical vapour deposition of silicon nitride," *Electronics Letters,* vol. 40, no. 16, pp. 1024-1026, 2004.

[19] P. J. Ker, A. R. Marshall, A. B. Krysa, J. P. David, and C. H. Tan, "Temperature dependence of leakage current in InAs avalanche photodiodes," *IEEE Journal of quantum electronics,* vol. 47, no. 8, pp. 1123-1128, 2011.

[20] W. Banerjee *et al.*, "Design of CMOS compatible, high-speed, highly-stable complementary switching with multilevel operation in 3D vertically stacked novel HfO2/Al2O3/TiOx (HAT) RRAM," *Advanced Electronic Materials,* vol. 4, no. 2, p. 1700561, 2018.

[21] K. S. Agrawal, V. S. Patil, and A. M. Mahajan, "Atomic layer deposited HfO2 ultra-thin films on different crystallographic orientation Ge for CMOS applications," *Thin Solid Films,* vol. 654, pp. 30-37, 2018.

[22] A. Troian *et al.*, "InAs-oxide interface composition and stability upon thermal oxidation and high-k atomic layer deposition," *AIP Advances,* vol. 8, no. 12, p. 125227, 2018.

[23] G. He, X. Chen, and Z. Sun, "Interface engineering and chemistry of Hf-based high-k dielectrics on III–V substrates," *Surface science reports,* vol. 68, no. 1, pp. 68-107, 2013.

[24] G. He *et al.*, "Effect of dimethylaluminumhydride-derived aluminum oxynitride passivation layer on the interface chemistry and band alignment of HfTiO-InGaAs gate stacks," *APL Materials,* vol. 1, no. 1, p. 012104, 2013.

[25] G. He *et al.*, "Interface control and modification of band alignment and electrical properties of HfTiO/GaAs gate stacks by nitrogen incorporation," *Journal of Materials Chemistry C,* vol. 2, no. 27, pp. 5299-5308, 2014.

[26] J. Zhang *et al.*, "Microstructure optimization and optical and interfacial properties modulation of sputtering-derived HfO2 thin films by TiO2 incorporation," *Journal of alloys and compounds,* vol. 611, pp. 253-259, 2014.

[27] G. He, J. Gao, H. Chen, J. Cui, Z. Sun, and X. Chen, "Modulating the interface quality and electrical properties of HfTiO/InGaAs gate stack by atomic-layer-deposition-derived Al2O3 passivation layer," *ACS applied materials & interfaces,* vol. 6, no. 24, pp. 22013-22025, 2014.

[28] R. Suzuki, K. Ozaki, K. Tsunoda, and H. Nishino, "ALD-Al2O3 passivation effects on surface characteristics of InAs/GaSb type-II superlattice infrared photodetectors," in *Infrared Technology and Applications XLV*, 2019, vol. 11002: International Society for Optics and Photonics, p. 110020B.

[29] O. Salihoglu, "Atomic layer deposited passivation layers for superlattice photodetectors," *Journal of Vacuum Science & Technology B, Nanotechnology and Microelectronics: Materials, Processing, Measurement, and Phenomena,* vol. 32, no. 5, p. 051201, 2014.

[30]   R. Nowicki, "Properties of rf-sputtered Al2O3 films deposited by planar magnetron," *Journal of Vacuum Science and Technology,* vol. 14, no. 1, pp. 127-133, 1977.

[31]   P. Carcia, R. McLean, M. Reilly, and G. Nunes Jr, "Transparent ZnO thin-film transistor fabricated by rf magnetron sputtering," *Applied Physics Letters,* vol. 82, no. 7, pp. 1117-1119, 2003.

[32]   A. Asadov, W. Gao, Z. Li, J. Lee, and M. Hodgson, "Correlation between structural and electrical properties of ZnO thin films," *Thin Solid Films,* vol. 476, no. 1, pp. 201-205, 2005.

[33]   B. B. Singh, V. Agrawal, A. G. Joshi, and S. Chaudhary, "X-ray photoelectron spectroscopy and conducting atomic force microscopy investigations on dual ion beam sputtered MgO ultrathin films," *Thin Solid Films,* vol. 520, no. 22, pp. 6734-6739, 2012.

[34]   M.-Y. Han and J.-H. Jou, "Determination of the mechanical properties of rf-magnetron-sputtered zinc oxide thin films on substrates," *Thin Solid Films,* vol. 260, no. 1, pp. 58-64, 1995.

[35]   D. E. Newbury* and N. W. Ritchie, "Is scanning electron microscopy/energy dispersive X-ray spectrometry (SEM/EDS) quantitative?," *Scanning,* vol. 35, no. 3, pp. 141-168, 2013.

[36]   M. Kabir, "Dark current mechanisms in amorphous selenium-based photoconductive detectors: an overview and re-examination," *Journal of Materials Science: Materials in Electronics,* vol. 26, no. 7, pp. 4659-4667, 2015.

[37]	P. Yu, K. Zhu, A. G. Norman, S. Ferrere, A. J. Frank, and A. J. Nozik, "Nanocrystalline TiO2 solar cells sensitized with InAs quantum dots," *The Journal of Physical Chemistry B,* vol. 110, no. 50, pp. 25451-25454, 2006.

[38]	H. Ibach, "Thermal expansion of silicon and zinc oxide (I)," *physica status solidi (b),* vol. 31, no. 2, pp. 625-634, 1969.

[39]	M. Halvarsson, V. Langer, and S. Vuorinen, "Determination of the thermal expansion of κ-Al2O3 by high temperature XRD," *Surface and coatings technology,* vol. 76, pp. 358-362, 1995.

[40]	D. K. Smith and H. Leider, "Low-temperature thermal expansion of LiH, MgO and CaO," *Journal of Applied Crystallography,* vol. 1, no. 4, pp. 246-249, 1968.

Chapter 7

7.   Conclusions and future work

7.1   Conclusions

The development of novel semiconductor materials, GaSbBi and InAs, for use in mid-infrared optotlectonic devices has been investigated. This thesis focused on studying the Schottky diode, MSM-PDs and fabricated from thin-film GaSbBi and InAs APDs. Despite significant articles has focused on the bandgap structure and growth properties of GaSbBi, comparatively only a few researches reported on the electrical and optical properties of GaSbBi based optoelectronic devices. One potential solution for improving the electrical characteristics of GaSbBi Schottky diode has been proposed. The viability of using Bi for mid-infrared sensing has been demonstrated as well. Besides, the development of the fabrication process of InAs-based APDs has also been studied.

The influence of postgrowth thermal annealing on GaSbBi Schottky diodes has been demonstrated. The effects of the annealing temperature and time on the material quality and electrical characteristics of the diodes have been investigated. The I-V characteristics indicated a better ideality factor and less leakage current at the reverse bias, as the annealing temperature increased up to 500 °C for 30 min. XRD and TEM measurements were performed to verify that the bismuth composition was unaffected during the annealing process. EDX analysis indicated that Sb clustering occurs at high annealing temperatures, resulting in a concomitant degradation in the electrical performance. The optimum electrical characteristics of the diode were obtained with an annealing temperature of 500 °C for 30 min, resulting in an ideality factor of 1.3 being achieved.

The optimised GaSbBi wafer was then used to fabricate MSM-PDs to investigate the viability of using Bi into mid-infrared sensing. The effect of Bi incorporation and different geometry of the electrode on photo spectral response has been investigated. The spectral response measurement of GaSbBi MSM-PDs suggested a bandgap reduction in a range of 26 ~ 29 meV/%Bi, at room temperature. The spectral response comparison between different geometry seems to indicate that Bi incorporation has reduced the carrier mobility on the surface of the semiconductor material.

Another potential mid-infrared compatible material, InAs-based APDs has also been demonstrated in this thesis. The effectiveness of a range of alternative high-k dielectric layers as potential passivation layers for InAs APDs has been investigated. The suppression of surface

leakage current is investigated by analysing the I-V performance of differently sized mesa diodes passivated with each oxide layer. Three potential passivation layers, include ZnO, Al_2O_3 and MgO, have been identified, all of which enables the suppression of the surface leakage in smaller sized devices of a radius of 50 μm and at lower temperatures of 175 K compared to a reference SU8 device. The influence of repeated temperature cycling on these layers has also been investigated with Al_2O_3 passivated devices, exhibiting no change in performance after multiple cooling and heating cycles.

In summary, it has been demonstrated that postgrowth annealing process at 500 °C for 30 mins can significantly improve the electrical characteristics of GaSbBi Schottky diode. Furthermore, the viability of incorporating Bi into GaSb and using for mid-infrared sensing have been investigated. The work presented in this thesis outlines a potential novel semiconductor material using for mid-infrared optoelectronic devices.

7.2   Future work

The solution of achieving good electrical characteristics of GaSbBi Schottky diode has been demonstrated as applying a postgrowth annealing process. However, several other aspects require addressing before achieving mature optoelectronic application.

Before potential optoelectronic applications are identified, a better understanding of the surface characteristics is preferred since the nature of GaSb based material, which is easily formed corresponding oxide layer. The question remains, as efficiently remove the native oxide layer to reduce the serial resistance and keep a smooth surface. A potential solution such as wet chemical etching, plasma etching can be applied to reduce the negative effect on device performance and studies the roughness of the surface. Meanwhile, metal-semiconductor contact formed via different material can also be investigated to find the suitable candidate for the different doping semiconductor material. Furthermore, apart from photodetectors, other essential more complicated device structures such as QW Lasers and p-i-n diodes are required for them to be sucsesfully utilised for infrared sensing and imaging. The extensive study will be needed to find out the most appropriate fabrication process for different optoelectronic devices.

Appendix

8.   Appendix A

Table. A. 1 Detail of each parameters used for forward JV characteristics of a diode with different conduction mechanism simulation in chapter 2

Symbol	Name	Value	Units
A^*	Effective Richardson constant	9.1[1]	$\text{A/cm}^2 - \text{K}^2$
ϕ_B	Barrier height	0.75[2]	eV
kT/q	Thermal voltage at 300 K	0.0259	V
S	Diode cross area	2.1×10^{-7}	m^2
N_C	Effective density of states in the conduction band at 300 K	4.37×10^{17}	cm^{-3}
q	Electron charge	1.6×10^{-19}	C
μ	Electron mobility at 300 K	9000	$\text{cm}^2/(\text{V·s})$
ε_m	Maximum electric field	3000[2]	V/cm
τ_0	Life time	1×10^{-7} [3]	S
n_i	Intrinsic carrier density at 300 K	2.03×10^{6} [4]	cm^{-3}
W	Depletion region	14 [5]	µm
$\hbar$	Reduced plank constant	1.054×10^{-34}	J-s
N	Doping concentration	4×10^{18}	cm^{-3}
m^*	Effective mass	0.067	kg
ε_S	Permittivity of GaAs	12.95 [6]	C/V-cm
ϕ_n	Fermi potential from conduction band edge in n-type semiconductor	0.65	eV

Equations

1. **The thermionic emission (TE) conduction theory**

$$J_n = J_{TE}[exp\left(\frac{qV}{kT}\right) - 1]$$

and

$$J_{TE} = A^*T^2 exp(-\frac{q\phi_B}{kT}) = 2.168 \times 10^{-7} \quad \text{(value taken from the table)}$$

2. **Diffusion**

$$J_n = J_D[exp\left(\frac{qV}{kT}\right) - 1]$$

and

$$J_D = qSN_C\mu\mathcal{E}_m exp(-\frac{q\phi_B}{kT}) = 1.05 \times 10^{-13} \text{ (value taken from the table)}$$

3. **Carrier generation and recombination in the depletion region**

$$I = I_{R0}[exp(qV/2kT) - 1]$$

and

$$I_{R0} = \frac{qSn_iW}{2\tau_0} = 4.77 \times 10^{-12} \quad \text{(value taken from the table)}$$

4. **Tunnelling through the barrier**

field emission (FE)

$$J_{FE} = \frac{A^{**}T\pi exp[-\frac{q(\phi_B-V)}{E_{00}}]}{c_1 ksin(\pi c_1 kT)}$$

where

$$c_1 \equiv \frac{1}{2E_{00}} log\left[\frac{4(\phi_B-V)}{-\phi_n}\right]$$

$$E_{00} = \frac{q\hbar}{2}\sqrt{\frac{N}{m^*\varepsilon_S}} = 1.81 \times 10^{-44}$$

And ϕ_n is the Fermi potential from conduction band edge in n-type semiconductor express as

$$\phi_n = \frac{E_F-E_V}{q}$$

thermionics field emission (TFE)

$$J_{TFE} = \frac{A^{**}T\sqrt{\pi E_{00} q(\phi_B - \phi_n - V)}}{k cosh(E_{00}/kT)} exp\left[\frac{-q\phi_n}{kT} - \frac{q(\phi_B - \phi_n)}{E_0}\right] exp\left(\frac{qV}{E_0}\right)$$

$$E_0 \equiv E_{00} coth\left(\frac{E_{00}}{kT}\right)$$

Reference

[1]   J. Borrego, R. Gutmann, and S. Ashok, "Richardson constant of Al-and Au-GaAs Schottky barrier diodes," Applied Physics Letters, vol. 30, no. 3, pp. 169-172, 1977.

[2]   T. Kubicki et al., "Calculation of the electric field in GaAs particle detectors," Nuclear Instruments and Methods in Physics Research Section A: Accelerators, Spectrometers, Detectors and Associated Equipment, vol. 345, no. 3, pp. 468-473, 1994.

[3]   F. D. Lenahan, "Photoconductivity and minority carrier lifetime in tin sulfide and gallium arsenide semiconductors for photovoltaics," Massachusetts Institute of Technology, 2016.

[4]   B. Van Zeghbroeck, "Principles of semiconductor devices," Colarado University, vol. 34, 2004.

[5]   G. Lioliou, C. Poyser, S. Butera, R. Campion, A. Kent, and A. Barnett, "30μm thick GaAs X-ray p+-i-n+ photodiode grown by MBE," Nuclear Instruments and Methods in Physics Research Section A: Accelerators, Spectrometers, Detectors and Associated Equipment, vol. 946, p. 162670, 2019.

[6]   W. E. Courtney, "Complex permittivity of GaAs and CdTe at microwave frequencies," IEEE Transactions on Microwave Theory and Techniques, vol. 25, no. 8, pp. 697-701, 1977.